Modelling coarse and giant desert dust particles

Eleni Drakaki[1,2], Vassilis Amiridis[1], Alexandra Tsekeri[1], Antonis Gkikas[1], Emmanouil Proestakis[1], Sotirios Mallios[1], Stavros Solomos[3], Christos Spyrou[1], Eleni Marinou[1,4], Claire L. Ryder[5], Demetri Bouris[6], and Petros Katsafados[2]

[1]IAASARS, National Observatory of Athens, Athens GR-15236, Greece
[2]Harokopion University of Athens (HUA), Department of Geography, Athens GR-17671, Greece
[3]Academy of Athens, Research Centre for Atmospheric Physics and Climatology, Athens GR-10679, Greece
[4]Institut für Physik der Atmosphäre, Deutsches Zentrum für Luft- und Raumfahrt, Oberpfaffenhofen, Germany
[5]University of Reading, Department of Meteorology, Reading, RG6 6BB, UK
[6]National Technical University of Athens, School of Mechanical Engineering, Athens, GR-15780, Greece

Correspondence to: Eleni Drakaki (eldrakaki@noa.gr)

Abstract. Dust particles larger than 20 μm in diameter have been regularly observed to remain airborne during long-range transport. In this work, we modify the parameterization of the mineral dust cycle in the GOCART-AFWA dust scheme of WRFV4.2.1, to include also such coarse and giant particles, and we further discuss the underlying misrepresented physical mechanisms which hamper the model in reproducing adequately the transport of the coarse and giant mineral particles. The initial particle size distribution is constrained by observations over desert dust sources. Furthermore, the Stokes' drag coefficient has been updated to account realistic dust particles sizes ($Re < 10^5$). The new code was applied to simulate dust transport over Cape Verde in August 2015 (AER-D campaign). Model results are evaluated against airborne dust measurements and the CALIPSO-LIVAS pure dust product. The results show that the modelled lifetimes of the coarser particles are shorter than those observed. Several sensitivity runs are performed by reducing artificially the particles' settling velocities in order to compensate underrepresented mechanisms, such as the non-spherical aerodynamics, in the relevant parameterization schemes. Our simulations reveal that particles with diameters of 5.5-17 μm and 40-100 μm are better represented under the assumption of a 80% reduction in the settling velocity (UR80) while particles with sizes ranging between 17 μm and 40 μm are better represented in a 60% reduction in settling velocity (UR60) scenario. The overall statistical analysis indicates that the best agreement with airborne in-situ measurements downwind (Cape Verde) is achieved with a 40% reduction in settling velocity (UR40). Moreover, the UR80 experiment improves the representation of the vertical structure of the dust layers as those are captured by the CALIPSO-LIVAS vertically-resolved pure dust observations. The current study highlights

Μορφοποίησε: Επικεφαλίδα 2 Char

Μορφοποίησε: Εκθέτης

the necessity of upgrading the existing model parameterization schemes of the dust life-cycle components towards improving the assessment of the dust-related impacts within the Earth-Atmosphere system.

~~Dust particles larger than 20 μm in diameter (0.2 μm < D < 100 μm) have been regularly observed to remain airborne during long-range transport. In this work we extend the parameterization of mineral dust cycle in the GOCART-AFWA dust scheme of WRFV4.2.1, to include also such coarse and giant particles. The initial particle size distribution in our parameterization is based on observations over desert dust sources and the Stokes' drag coefficient has also been updated to account for dust particles of all sizes ($Re < 10^5$). The new code is applied to simulate dust transport over Cape Verde during the August 2015 AER-D campaign. Model results are evaluated using both airborne dust measurements and the CALIPSO-LIVAS pure dust product. The results show that the modeled lifetimes of the coarser particles are shorter than those observed. Various processes are proposed to explain such inaccuracies, such as the electric field inside dust plumes and non-spherical aerodynamics. Additional sensitivity runs are performed by artificially reducing the settling velocities of the particles to compensate for such underrepresented processes in the model. Our simulations show that particles with diameters of 5-17 μm and 40-100 μm are better represented assuming 80% reduction in settling velocity (UR80) while particles at the range 17-40 μm are better represented in the UR60 scenario. The overall statistical analysis shows that the UR80 experiment presents the closest agreement with the airborne in situ measurements both in Cape Verde and over the sources. The UR80 experiment improves also the vertical distribution of dust in the model, as compared to the CALIPSO-LIVAS pure dust product. Further research is requested in order to understand the physical processes behind the reduction of settling velocity.~~

1 Introduction

Μορφοποιήθηκε: Επικεφαλίδα 2

Μορφοποιήθηκε: Εσοχή: Πρώτη γραμμή: 1,27 εκ.

Dust is the most prominent contributor to the global aerosol burden, in terms of dry mass, and it ranks second in aerosol emissions (Gliß et al., 2021; Huneeus et al., 2019; Textor et al., 2006). ~~Dust is the prominent contributor to the aerosol burden worldwide and ranks second in aerosol emissions (Textor et al., 2006)~~. The major sources of dust are situated across the "dust belt" ~~span the "dust belt"~~ (Prospero et al., 2002) stretching in the Northern Hemisphere hosting deserts and erodible soils ~~in the Northern Hemisphere, which hosts deserts, bare, and erodible soils~~ (e.g.,Goudie and Middleton, 2006), that are prone to windblown dust ~~emissions~~. Most of the global dust budget comes from the Sahara Desert, followed by deserts in the Middle East and Asia. (Ginoux et al., 2012; Huneeus et al., 2011; Kok et al., 2021; Li and Osada, 2007). Spatially more limited desert regions in the Southern Hemisphere emit lower amounts of mineral particulate matter (Ginoux et al., 2012; Huneeus et al., 2011; Kok et al., 2021; Li and Osada, 2007) , and less than 5% comes from high-latitude sources (Bullard et al., 2016).

Dust particles act as ice nuclei (IN) on cold cloud processes (Marinou et al., 2019; Solomos et al., 2011) and when mixed or coated with hygroscopic material, they can affect warm cloud processes (Twohy et al., 2009) and serve as cloud condensation nuclei (CCN). Dust particles rich in key micronutrients such as iron (Fe) and phosphorus (P) affect biogeochemical processes in marine and terrestrial ecosystems (Jickells et al., 2005; Okin et al., 2004; Stockdale et al., 2016; Tagliabue et al., 2017) and disrupt the carbon cycle (Jickells et al., 2014) ~~during~~ after their wet and dry deposition. Severe dust

episodes can affect aviation and telecommunications (Harb et al., 2013; Weinzierl et al., 2012; Nickovic et al., 2021), human health (e.g., Du et al., 2016; Giannadaki et al., 2014) and solar energy productionpower generation (Kosmopoulos et al., 2018).

Apart fromIn addition to the dust load intensity of dust load, the size of the suspended mineral particles plays a determinant role on the related impacts ona key factor in the effects of dust particles on weather and climate, is the size of the suspended mineral particlesamong others. Larger dust particles act more effectively efficiently as CCN (Petters and Kreidenweis, 2013) and IN (Diehl et al., 2014) altering cloud microphysical processes, their evolution and dissolution, and subsequently the hydrological cycle in the atmosphere. Recent research studies suggests that coarser dust aerosols are more effective at absorbingabsorbers of the incoming solar radiation, thus enhancing enhancing atmospheric warming (Mahowald et al., 2014; Ryder et al., 2019). Therefore, it is imperative to represent realistically A complete representation of the dust particle size distribution (PSD) facilitating a thorough investigation on the dust transport processes and the dust-induced impacts.is required for the comprehensive study of dust-related processes in the atmosphere and the assessment of associated impacts.

Airborne dust particles has been observed to sizes up to 300 μm, whereas even larger particles with diameters up to 450 μm have been recorded from in situ deposition measurements acquired at buoys mounted across the Tropical Atlantic Ocean (van der Does et al., 2018).The diameter (D) range of airborne dust particles is mainly between 0.2 μm and 300 μm, while even larger particles with diameters up to 450 μm have been reported from in situ deposition measurements from buoys in the Atlantic Ocean (van der Does et al., 2018). The size range ofDust particles is are usually divided into three different modes, (fine, coarse, and giant), without strictly defined limits bounds of their sizes (Goudie, 2014; Knippertz and Stuut, 2014). According to Ryder et al. (2019), the fine mode includes represents dust particles with $D \leq 2$ μm, for the coarse mode those with diameters between 2 μm < D < and 20 μm, and for the giant mode particles with $D \geq 20$ μm. A recent study (Ryder et al., in preparation) suggests that the above modes can be further divided descritized into four categories, namely fine ($D < 2.5$ μm), coarse (2.5-10 μm), super-coarse (10-62.5 μm), and giant ($D > 62.5$ μm).

The existence of dust particles larger than 20 μm in diameter was already demonstrated in the 1970s based on measurements in the Caribbean (Prospero et al., 1970). Nevertheless, these sizes were neglected in atmospheric dust models since giantbecause such particles were assumed to be rare. This assumption has been disproved in recent decades by a large number of airborne campaigns equipped with state-of-the-art in situ and remote sensing instruments. Specifically, in the framework of the SAMUM1 (Weinzierl et al., 2009) and SAMUM2 (Liu et al., 2018) experimental campaigns it has been justified that above sources dust aerosols up to 40 μm in diameter were recorded in 20% of the identified dust layerstook place over dust sources and downwind areas (i.e., off the western coasts of N. Africa), in 2006 and 2011 respectively, and presented that over the sources dust aerosols up to 40 μm in diameter were recorded in 20% of the identified dust layers, while over Cape Verde mineral particles up to 30 μm in diameter were measured (Weinzierl et al., 2011)., This reduction of dust particle sizes, along the transport pathway, is attributedwhich indicate a reduction in dust particle size along the transport path due to gravity the gravitational settling. Similar results findings were reported in the FENNEC campaign (Ryder et al., 2013a) with mean effective particle diameters ranges of 22 to 28 μm and 15 to 18 μm for fresh and aged dust, respectively. During the AER-D

Μορφοποιήθηκε: Εσοχή: Πρώτη γραμμή: 1,27 εκ.

campaign, in the Saharan outflow ~~areas~~ zone near Cape Verde and the Canary Islands, mineral particles with diameters ~~greater~~ larger than 20 μm were systematically recorded, while ~~their diameters exceeded 40 μm~~ in 36% of the ~~total~~ studied cases, particles with diameters larger than 40 μm recorded (Ryder et al., 2018).~~;~~ Dust particles with diameters of 10 to 30 μm were detected during the SALTRACE campaign in Barbados ~~(Weinzierl et al., 2017) (Weinzierl et al., 2017a)~~, revealing that they were suspended at about 2000 km more than what would be expected from the Stokes' theory (Weinzierl et al., 2017).~~showing that they occur at larger distances than would be expected according to Stokes' theory of gravity.~~

Atmospheric dust models are the optimal tool to ~~represent~~ simulate the components of the dust cycle and therefore to study the dust-related effects. However, the state-of-the-art atmospheric dust models are characterized by inherent limitations in accounting for realistic emission and transport dust size distributions ~~in emission and transport~~ (Huang et al., 2020; Kok, 2010; Mahowald et al., 2014). To overcome these model drawbacks, it is needed to extend the PSD towards ~~we need to include~~ the giant particles size spectrum ~~in the models~~ in order to shed light on~~study~~ the processes that ~~keep~~ sustain ~~the~~ larger dust aerosols in the atmosphere for longer periods than expected.

Ginoux, (2003) modeled dust aerosols up to 70 μm in diameter using the Global Ozone Chemistry Aerosol Radiation and Transport (GOCART) model and examined the effects of non-sphericity assuming randomly oriented ellipsoidal particles. His results showed that ~~reducing~~ the reduction of the settling velocity ~~efficiently reproduces~~results in a better agreement with ~~the~~ observations when the aspect ratio is equal or greater than 5. The new modeled particle size distributions (PSDs) were in generally better agreement with the AERONET observations, although the PSDs were significantly underestimated for diameters near 10 μm. The aspect ratio of 5 results in a reduction in settling velocity of about 45% for particles with sphere volume-equivalent diameters near 10 μm and 60% for particles with sphere-volume-equivalent diameters near 30 μm. Maring et al. (2003) applied a simple empirical model and suggested that an upward velocity of 0.0033 ms^{-1} (0.33 cm s^{-1}) is required to accurately predict PSD changes during transport. Although their comparisons were limited to sizes up to 25 μm, they pointed out that unknown or not well-known processes counteract gravity settling ~~by gravity~~. Possible ~~Proposed~~ mechanisms which can interpret the aforementioned findings are~~include:~~ (i) vertical mixing within the Saharan air layer during the day (Gasteiger et al., 2017), (ii) the lower settling velocities of non-spherical dust particles (Huang et al., 2020; Mallios et al., ~~2020~~2022), (iii) the underrepresented meteorological conditions (O'Sullivan et al., 2020), (iv) the unresolved turbulence (Gu et al., 2021), (v) the electrification of dust (Daskalopoulou et al., 2021; Mallios et al., 2021a; Mallios et al., 2022; Joseph R. Toth III et al., 2020; Renard et al., 2018; Nicoll et al., 2011) and (vi) the numerical errors that perturb the mass balance (Ginoux, 2003a).

In this work, we demonstrate for the first time a method for incorporating coarse and giant desert dust particles (D > 20 μm, following ~~according to~~ the definition of dust modes proposed in Ryder et. al, (2019) into the Advanced Research Weather version of the Weather Research and Forecasting (WRF-ARW) model in conjunction with the GOCART (Ginoux et al., 2001) aerosol model and the Air Force Weather Agency (AFWA) dust emission scheme (LeGrand et al., 2019) (WRF-GOCART-AFWA model). After pinpointing that the model quickly deposits coarse and giant dust particles, we investigate the reasons behind those findings. We use sophisticated in situ PSD measurements to initialize the model over the sources and to evaluate the simulated PSD over the receptor areas. We also use pure-dust spaceborne retrievals to assess the model

Μορφοποίησε: Αγγλικά (Ηνωμένων Πολιτειών), Μοτίβο: Διαφανές

Μορφοποιήθηκε: Εσοχή: Πρώτη γραμμή: 1,27 εκ.

performance in terms of reproducing the vertical structure of the dust layers. In addition, we perform a series of sensitivity tests by reducing the settling velocity of mineral particles in the model and we investigate the concomitant effects on dust fields. ~~We use advanced in situ measurements from PSD to initialize the model. To evaluate our results, we use both in situ measurements of PSD and satellite retrievals of the extinction coefficient and compare the modelled PSDs after transport and the vertical distribution of dust layers. In addition, we reduce the settling velocity of the particles in the model and study the effects on the dust field properties.~~

The article is organized as follows: In Sect. 2, we describe the methodology in terms of the changes we made to the code of WRF-GOCART-AFWA, the setup of the model and the experiments performed, and the observational data we used for model validation. The results of our work are presented in Sect. 3 and Sect. 4 contains the discussion and conclusions of this work.

2 Model and Data

2.1. WRF-GOCART-AFWA model

In our numerical experiments to study the transport of coarse and giant dust aerosols, we use the WRF-ARWv4.2.1 model coupled with the GOCART aerosol model and the AFWA dust emission scheme (LeGrand et al., 2019). The current version of the WRF-GOCART-AFWA model accounts for giant dust particles in the calculated dust emission fluxes (up to 125 μm) and assumes that the transported dust particles are up to 20 μm in diameter. To extend the transport PSD to coarser and giant mineral particles, we implemented several developments in the standard WRF-GOCART-AFWA model, which are ~~described and~~ discussed in Sect. 2.1.1 and 2.1.2. Figure 1 shows a sketch of the workflow: the first three steps refer to the implemented ~~extensions~~ modifications in the standard WRF-GOCART-AFWA code: In **step 1**, we establish the definition of a prescribed PSD for the emitted dust particles at the source based on in situ reference measurements, and we distribute the total emitted dust accordingly; in **step 2**, we define five size ranges (five model size bins) for the transported PSD covering dust particle sizes (in diameter) spanning from 0.2 μm to 100 μm (Sect. 2.1.1);~~in **step 2**, we define five size ranges (five model size bins) for the transported PSD to cover the entire size range of dust particles in the atmosphere (Sect. 2.1.1);~~ in **step 3**, we implement an updated drag coefficient that applies to the sizes of the entire range of Aeolian dust PSD (Sect. 2.1.2). These code ~~changes~~ upgrades are integrated into the new WRF-L model. Table 1 shows the properties of the size bins in the standard WRF-GOCART-AFWA code and the size classes defined in the new WRF-L code. ~~The final~~At **step 4** ~~is to~~we perform model experiments and validate the model results using different model configurations against observations (Sect. 2.2), as described in detail in Sect. 3.

Μορφοποιήθηκε: Εσοχή: Πρώτη γραμμή: 1,27 εκ.

2.1.1 Dust size distribution

In observational studies of non-spherical particles, it is customary to describe their size in terms of spherical volume equivalent diameter. ~~In the followingHere, particle size data refer to sphere volume-equivalent diameter, unless otherwise noted. T,~~to describe particles' ~~the~~ sizes ~~of the particles in~~distributed within the five size bins of the WRF-L model, we use the

Μορφοποιήθηκε: Εσοχή: Πρώτη γραμμή: 1,27 εκ.

sphere-volume-equivalent effective diameter (D_{eff}), which is more relevant to the optical properties of the particles (Hansen and Travis, 1974). In this way, we simplify the comparison between the model calculations and the observations of the optical properties of the particles (e.g., dust optical depth). The D_{eff} in (m) of each size bin is calculated as shown in Eq. 1, and is provided in Table 1.

$$D_{eff} = \frac{\int_{D_{lo,k}}^{D_{u,k}} D^3 \cdot \frac{dN}{dD} \cdot dD}{\int_{D_{lo,k}}^{D_{u,k}} D^2 \cdot \frac{dN}{dD} \cdot dD}, \quad (1)$$

Where D is the particle diameter in (~~μ~~m) and $\frac{dN}{dD}$ is the particle number size distribution in number of particles per ~~c~~m^{-3}. The parameters ~~of~~ at each size bin ~~*ik*~~ are ~~shown~~ listed in Table 1~~Table 3~~. Henceforward, references about the size of the particle correspond to particle volume equivalent effective diameter, unless mentioned otherwise.

In the default GOCART-AFWA dust emission scheme of WRF, the total emitted vertical dust flux is estimated at each grid point prone to dust emission, when favorable conditions are met. The dust flux is then distributed over five transport size bins, based on the fragmentation theory of Kok, (2011), bounded~~although limited~~ to diameters up to 20 μm. Since our goal is to ~~to include~~consider larger dust particles than those commonly used in the current atmospheric dust models, we redefine the five transport model bins ~~to include~~including particles with diameters up to 100 μm (Table 1). ~~We use a prescribed PSD for emitted dust particles at the source based on in situ measurements from the FENNEC campaign (Ryder et al., 2013a). Ryder et al., (2013a) made airborne in situ measurements of dust PSDs at various altitudes near dust sources in the Sahara Desert. The emitted dust PSD used in our work is derived from measurements of fresh upwelling cases at the lowest available altitudes from aircraft profiles representative of 1 km and is hereafter referred to as the "observed FENNEC-PSD". The observed FENNEC-PSD is shown in Fig. 2(a) with red squares, and the shaded areas show the size range of the individual bins. In Sect. 2.2.1 more information are provided about the FENNEC campaign and the instruments used for the measurements.~~

~~The distribution of emitted mass over the redefined size range is obtained by calculating the mass fraction resulting from the weighting factors ($k_{factors}$) for each transport bin, as shown in Eq. 2.~~ We rely on prescribed PSD for the emitted dust particles at the source based on the airborne in situ measurements acquired during the FENNEC campaign of 2011 (Ryder et al., 2013a). More specifically, for the freshly uplifted dust we use the mean PSD at the lowest available height (i.e., 1km), obtained by averaging profile measurements above the Sahara (Mauritania and Mali), hereafter called the "observed FENNEC-PSD", which is shown in Fig. 2(a) with red squares. Figure 2a shows also the “fitted FENNEC-PSD” (solid red line), which is the fit of the “observed FENNEC-PSD”, using five lognormal modes (Table 4). In Sect. 2.2.1 more information is provided on the derivation of the mean "observed FENNEC-PSD", including also the description of the FENNEC 2011 campaign, the in-situ instrumentation used and the processing of the acquired data. Based on the FENNEC-PSD we calculate the mass fraction

Μορφοποιήθηκε: Εσοχή: Πρώτη γραμμή: 1,27 εκ.

($k_{factors}$) distributed among the redefined transport model size bins in Eq. 2. The weighting factors $k_{factors}$ are ~~also~~ shown in Fig.2(b).

$$k_{factors} = \frac{\int_{Dlo,k}^{Du,k} \frac{1}{D} \frac{dV}{dlnD} dD}{\int_{Dlo,k_{min}}^{Du,k_{max}} \frac{1}{D} \frac{dV}{dlnD} dD} \int_{Dlo,k}^{Du,k} \frac{1}{D} \cdot \frac{dV}{dlnD} \cdot dD, \quad (2)$$

Where D is the particle diameter, $\frac{dV}{dlnD}$ is the volume size distribution in $\mu m^3 cm^{-3}$, $D_{lo,k}$ and $D_{u,k}$ are the margins of each size bin k in µm.

Μορφοποίησε: Αγγλικά (Ηνωμένων Πολιτειών)

2.1.2 Updated gravitational scheme

In the GOCART-AFWA dust scheme of WRF, the forces acting on a dust particle moving along the vertical direction are the gravitational force F_g and the aerodynamic drag force F_{drag}, which are mathematically expressed in Eq.3 and Eq.4, respectively.

$$F_g = \rho_p \cdot V_p \cdot g, \quad (3)$$

$$F_{drag} = \frac{1}{2} \cdot \frac{C_D}{C_{cun}} \cdot A_p \cdot \rho_{air} \cdot u_{term}^2, \quad (4)$$

Where ρ_p stands for particle density in kgm^{-3}, g corresponds to the gravitational acceleration in ms^{-2}, $V_p = \frac{1}{6} \cdot \pi \cdot D_{eff}^3$ is the particle volume in m^3 and $A_p = \frac{\pi}{4} \cdot D_{eff}^2$, is the particle's projected area normal to the flow in m^2, ρ_{air} is the air density in kgm^{-3}. and D_{eff} represents the particles' diameter in m for each model size bin (assuming spherical particles, as defined in Sect. 2.1.1). C_D is the aerodynamic drag coefficient (unit less) and C_{cun} is the slip correction to account for slip boundary conditions (Davies, 1945) and it is expressed as a function of the air mean free path (λ, in meters) (Eq. 5):

$$C_{cun} = C_{cun}(\lambda) = 1.0 + \frac{2 \cdot \lambda}{D_{eff}} [1.257 + 0.4 \cdot e^{\frac{-1.1 \cdot D_{eff}}{2 \cdot \lambda}}], \quad (5)$$

The constant velocity that a particle builds up falling vertically within the Earth's atmosphere, is defined as the terminal settling velocity u_{term}, and it can be estimated by solving the 1-D equation of motion at the steady state limit, where net force is assumed to be equal to zero:

$$\rho_p \cdot V_p \cdot g = \frac{1}{2} \cdot \frac{C_D}{C_{cun}} \cdot A_p \cdot \rho_{air} \cdot u_{term}^2, \quad (6)$$

In the default GOCART-AFWA dust scheme the drag coefficient is given by Stokes' Law and is defined as:

$$C_D = \frac{12}{Re}, \quad (7)$$

Where Re is the Reynold's number (unit less) given by the following equation as a function of the particle volume equivalent effective diameter D_{eff}:

$$Re = \frac{\rho_{air} \cdot u_{term} \cdot D_{eff}}{2 \cdot \mu}, \quad (8)$$

Where μ is the air dynamic viscosity in $\frac{kg}{m \cdot s}$ defined as a function of air temperature T in K by the following equation (Hilsenrath, 1955; United States Committee on Extension to the Standard Atmosphere., 1976):

$$\mu = \frac{\beta \cdot T^{\frac{3}{2}}}{T+S}, \quad (9)$$

where S is the Sutherland constant which equal to 110.4 K and β is a constant which equals to $1.458 \cdot 10^{-6}\ kg \cdot m^{-1} \cdot s^{-1} \cdot K^{-1/2}$.

and the air mean free path is expressed as:

$$\lambda = \frac{1.1 \cdot 10^{-3} \cdot \sqrt{T}}{P} \quad (10)$$

Where T is the air temperature in K and P the air pressure in hPa.

The slip-corrected drag coefficient of the Stokes' Law ($\frac{12}{Re \cdot C_{cun}}$) is valid only for Re <<1, thus it is not representative for particles with D_{eff} larger than ~10 μm. Therefore, an adaptation of the drag coefficient is needed in order to be valid for higher Re values (i.e., 0<Re<16), since in our work dust particles with diameters larger than 20 μm are considered. To realize, we use the drag coefficient C'_D (Eq. 11), proposed by Clift and Gauvin, (1971):

$$C'_D = \frac{12}{Re} \cdot (1 + 0.2415 \cdot Re^{0.687}) + \frac{0.42}{1+\frac{19019}{Re^{1.16}}}, \ for \ \ Re < 10^5 \quad (11)$$

Mallios et al., (2020) used the same C'_D as a reference for the development of a drag coefficient for prolate ellipsoids, as more suitable for $Re < 10^5$. The departures between the drag coefficients given by Stokes and Clift and Gauvin (1971) become

more evident for increasing particles' sizes. More specifically, the drag coefficient given by Clift and Gauvin (1971) can be up to 2 times higher than those of the Stokes' Law for coarse and giant particles (Fig. S1).

In the default WRF code the slip correction is applied unconditionally for all the Re values, probably without affecting the solution significantly due to the small particle sizes ($D_{eff} < 20\ \mu m$). However, in our work a condition is required for applying the slip correction only in the Stokes' regime (e.g. Re < 0.1, Mallios et. al, 2020). Hence, we apply the bisection method to calculate the terminal velocity for each model size bin using the revised drag coefficient and, at first, ignoring the slip correction. When the solution lies in the Stokes' regime (e.g. Re < 0.1), we recalculate the settling velocity using the corrected drag coefficient $C'_{D,slip} = \frac{C'_D}{C'_{cun}}$, where $C'_{cun} = C_{cun}(\lambda')$ with λ' the mean free path obtained by (Jennings, 1988):

$$\lambda' = \sqrt{\frac{\pi}{8}} \cdot \frac{\frac{\mu}{0.4987445}}{\sqrt{p\rho_{air}}}, \quad (12)$$

~~In WRF-GOCART-AFWA, the forces acting on a dust particle moving along the vertical direction, are the gravitational force F_g and the aerodynamic drag force F_{drag}, which are mathematically expressed in Eq.3 and Eq.4, respectively.~~

~~$$F_g = \rho_p \cdot V_p \cdot g, \quad (3)$$~~

~~$$F_{drag} = \frac{1}{2} \cdot \frac{C_D}{C_{cun}} \cdot A_p \cdot \rho_{air} \cdot u_{term}^2, \quad (4)$$~~

~~The constant velocity that a particle builds up, as it falls vertically in the Earth's atmosphere, is defined as the terminal settling velocity u_{term}, and it can be estimated by solving the 1-D equation of motion in the steady state limit, where ΣF is assumed to be equal to zero:~~

~~$$\rho_p \cdot V_p \cdot g = \frac{1}{2} \cdot C_D \cdot A_p \cdot \rho_{air} \cdot u_{term}^2, \quad (5)$~~

~~Where ρ_p is the particle density in $\frac{kg}{m^3}$, g is the gravitational acceleration in $\frac{m}{s^2}$, V_p is the particle volume in m^3 and A_p is the particle projected area normal to the flow in m^2, ρ_{air} is the atmospheric air density in $\frac{kg}{m^3}$ and C_D is the aerodynamic drag coefficient (unit less). For each size bin it is assumed that the particles are spherical with diameter D_{eff} in m (as defined in Sect. 2.1.1), thus their volume and projected area are defined by the following equations for spheres:~~

~~$$A_p = \frac{\pi}{4} \cdot D_{eff}^2, \quad (6)$~~

~~$$V_p = \frac{1}{6} \cdot \pi \cdot D_{eff}^3, \quad (7)$~~

The drag coefficient is that of Stokes' Law and is defined as:

$$C_D = \frac{12}{Re}, \quad (8)$$

Where Re is the Reynold's number (unit less) given by the following equation:

$$Re = \frac{\rho_{air} \cdot u_{term} \cdot D_{eff}}{2 \cdot \mu}, \quad (9)$$

Where μ is the air dynamic viscosity in $\frac{kg \cdot s}{m}$ defined as a function of air temperature T in ^oK by the following equation:

$$\mu = \frac{1.458 \cdot 10^{-6} \cdot T^{\frac{3}{2}}}{T + 110.4}, \quad (10)$$

Equation 7 has been derived with the simplification of no-slip boundary conditions, thus a correction factor C_{cun}, proposed by Davies, C. N. (1945), is applied to the Stokes' relationship to account for velocity slip at the particle's surface. The corrected drag coefficient become is:

$$C_{D,slip} = \frac{C_D}{C_{cun}}, \quad (11)$$

Where C_{cun} is given by:

$$C_{cun} = C_{cun}(\lambda) = 1.0 + \frac{2 \cdot \lambda}{D_{eff}} [1.257 + 0.4 \cdot e^{\frac{-1.1 \cdot D_{eff}}{2 \cdot \lambda}}], \quad (12)$$

Where $\lambda = \frac{1.1 \cdot 10^{-7} \cdot \sqrt{T}}{p}$ is the air mean free path in m and μ is the air dynamic viscosity in $\frac{kg \cdot s}{m}$, as defined by Eq.10. T is the air temperature in ^oK and P the air pressure in hPa.

Substituting Eq. 6-9 in Eq. 4 we end up with the relationship for the terminal velocity of the dust particles, as shown in Eq. 12.

$$u_{term} = \frac{\rho_p \cdot g \cdot D_{eff}^2 \cdot C_{cun}}{18 \cdot \mu}, \quad (13)$$

The slip-corrected drag coefficient of the Stokes' Law (Eq.10) is valid only when Re <<1, thus it is not representative for particles with D_{eff} larger than ~10 μm. Since our work includes dust particles with diameters larger than 20 μm, the drag coefficient must be representative for higher values of Re (i.e., $0 < Re < 16$). For this reason, we adapt the drag coefficient

~~C'_D of Eq.13, proposed by (Clift and Gauvin, 1971), instead. C'_D has been recently used in (Mallios et al., 2020) as a reference for the development of a drag coefficient for prolate ellipsoids, as more valid for $Re < 10^5$ (Clift et al., 2005).~~

~~$$C'_D = \frac{12}{Re} \cdot (1 + 0.2415 \cdot Re^{0.687}) + \frac{0.42}{1+\frac{19819}{Re^{1.115}}}, \quad for \quad Re < 10^5 \qquad (14)$$~~

~~Using Eq.5, 6, 7, 9 and 14 we calculate the terminal velocity for each model size bin. Since the resulting equation is not linearly dependent by D_{eff} we apply the bisection method to solve the equation.~~

~~In the default code the slip correction is applied unconditionally, as mentioned above, for all the values of Re. However, slip correction is defined in Stokes' regime (Mallios et al., 2020). Thus, in the updated drag coefficient, only when $Re < 0.1$ (Stokes' regime), we recalculated the settling velocity using the corrected drag coefficient $C_{d,slip} = C'_D / C'_{cun}$, where $C'_{cun} = C_{cun}(\lambda')$ with λ' the mean free path adopted by (Jennings, 1988):~~

~~$$\lambda' = \sqrt{\frac{\pi}{8}} \cdot \frac{\frac{\mu}{0.499271}}{\sqrt{P}\rho_{air}}, \qquad (15)$$~~

~~here μ is air dynamic viscosity in $\frac{kg \cdot s}{m}$, as defined by Eq.10, and the atmospheric pressure P is in Pa.~~

2.1.3 Model experiments

Using the WRF-L code, we first run the CONTROL experiment. Our simulation period coincides with the AER-D experimental campaign (29/7 - 25/8/2015) for a domain bounded between the 1.42ºN and 39.99ºN parallels and stretching between the 30.87ºW and 46.87ºE meridians (Fig. 3). The simulation area encompasses the major Saharan also including the downwind areas in the eastern Tropical Atlantic. We use an equal-distance grid with a spatial grid spacing of 15 km x 15 km consisting of 550 × 300 points whereas in vertical, 70 vertical sigma pressure levels up to 50 hPa are utilized (defined by the model). The simulation period consists of nine 84-hour forecast runs, which are initialized at 12 UTC, using the 6-hour Global Forecast System Final Analysis (GFS - FNL) reanalysis product, available at a 0.25ºx0.25º spatial grid spacing. The sea surface temperatures, acquired by the NCEP daily global SST analysis (RTG_SST_HR), are updated every six hours along with the lateral boundary conditions. Topography is interpolated from the 30-sec Global Multi-resolution Terrain Elevation Data 2010 (GMTED2010, Danielson and Gesch, (2011)). Land use is defined based on the Moderate-resolution Imaging

Μορφοποίησε: Αγγλικά (Ηνωμένων Πολιτειών)
Μορφοποιήθηκε: Κανονικό (Web), Πλήρης, Εσοχή: Πρώτη γραμμή: 1,27 εκ., Διάστιχο: 1,5 γραμμές
Μορφοποίησε: Αγγλικά (Ηνωμένων Πολιτειών), Εκθέτης
Μορφοποίησε: Αγγλικά (Ηνωμένων Πολιτειών)
Μορφοποίησε: Αγγλικά (Ηνωμένων Πολιτειών), Εκθέτης
Μορφοποίησε: Αγγλικά (Ηνωμένων Πολιτειών)
Μορφοποίησε: Αγγλικά (Ηνωμένων Πολιτειών), Εκθέτης
Μορφοποίησε: Αγγλικά (Ηνωμένων Πολιτειών)
Μορφοποίησε: Αγγλικά (Ηνωμένων Πολιτειών), Εκθέτης
Μορφοποίησε: Αγγλικά (Ηνωμένων Πολιτειών)
Μορφοποίησε: Αγγλικά (Ηνωμένων Πολιτειών), Εκθέτης
Μορφοποίησε: Αγγλικά (Ηνωμένων Πολιτειών)
Μορφοποίησε: Αγγλικά (Ηνωμένων Πολιτειών), Εκθέτης
Μορφοποίησε: Αγγλικά (Ηνωμένων Πολιτειών)
Μορφοποίησε: Αγγλικά (Ηνωμένων Πολιτειών)
Μορφοποίησε: Αγγλικά (Ηνωμένων Πολιτειών)

Spectroradiometer (MODIS) observational data, modified by the University of Boston (Gilliam and Pleim, 2010). From each 84-hours cycle, the first 12 hours are discarded due to model spin up. Likewise, the first week of the simulation served as a spin-up run for the accumulation of the background dust loading and it is excluded from the analysis.~~Using the WRF-L code, we run a simulation that serves as a CONTROL experiment. Our simulation period coincides with the AER-D experimental campaign and covers the days from July 29, 2015 to August 25, 2015 for a region extending in latitude and longitude along [1.42°N;39.99°N] and [46.87°E;30.87°W] (Fig. 3). The simulation area is located over the major Saharan sources and also includes the downwind areas in the eastern sector of the tropical Atlantic. We use an equal-distance grid with a spatial grid spacing of 15 km x 15 km that includes 550 × 300 points and 70 vertical sigma pressure levels up to 50 hPa. For each run, 84-hour forecast cycles are performed and reinitialized every 3 days using the 6-hour Global Forecast System Final Analysis (GFS - FNL) reanalysis product, available at a 0.25°x0.25° model grid, to initialize the model and set boundary conditions. The first week of the simulation served as a spin-up run for the accumulation of the background dust loading and is excluded from the analysis.~~ The simulation runs are performed in a dust-only mode, ~~without including~~neglecting the radiative feedback from aerosols~~, to avoid (in this first case) a more complicated analysis that would include the radiative effect on dust transport.~~ We scale the dust source strength, by tuning the empirical proportionality constant in the horizontal saltation flux equation (in eq. 10 in LeGrand et al., (2019)) in order to obtain the best match between the modeled DOD and the AERONET AOD (RMSE=0.34, bias=-0.07) acquired at 8 desert stations: Banizoumbou, Dakar, El_Farafra, Medenine- IRA, Oujda, Tizi_Ouzou, Tunis_Carthage, Ben_Salem). Note that we take into account only AERONET records when AODs are higher than 0.2 (Version 3.0, Level 1.5, Giles et al., 2019; Sinyuk et al., 2020) and the Angstrom exponent is lower than 0.75. The tuning constant is equal to 3 and is applied throughout the model domain.~~The scaling of the dust source strength is chosen to best match the modeled DOD with the AERONET measurements (RMSE=0.34, bias= 0.07) from the desert stations: Banizoumbou, Dakar, El_Farafra, Medenine- IRA, Oujda , Tizi_Ouzou, Tunis_Carthage ,Ben_Salem). We only use the measurements where DOD is higher than 0.75 and the Angstrom exponent is lower than 0.2 to ensure that contamination by aerosols other than dust is negligible.~~ The complete configuration options for the run are listed in Table 2. The resolution applied in this study (15km grid spacing) is adequate for the scale of phenomena we want to study, improves the representation of topography and increases the accuracy of the reproduced weather and dust fields compare to coarser resolution such as used in global datasets (e.g. 0.5 deg GFS) (Cowie et al., 2015; Basart et al., 2016; Roberts et al., 2017; Solomos et al., 2018). WRF-Chem solver uses a 5th-order horizontal advection scheme and a 3-rd order vertical advection scheme to solve the scalar

Μορφοποίησε: Αγγλικά (Ηνωμένων Πολιτειών)

Μορφοποίησε: Αγγλικά (Ηνωμένων Πολιτειών)

Μορφοποίησε: Αγγλικά (Ηνωμένων Πολιτειών)

conservation equation, along with the 3-rd order Runge-Kutta time integration scheme (Grell et al., 2005). The use of such high-order advective schemes eliminate the numerical errors of diffusion in the code. We should note though that in the deposition parameterization of GOCART-AFWA dust scheme the vertical advection of the losses due to the gravitational settling is solved by a first order explicit scheme, which is notoriously too diffusive (Versteeg and Malalasekera, 2007) and thus it can possibly induce numerical errors in the mass conservation (Ginoux, 2003). A series of additional sensitivity runs has been performed aiming to resemble possible mechanisms (misrepresented or even absent in the model) counteracting gravitational settling towards reducing the differences between the CONTROL run calculations and the in-situ observations (shown in Sect. 3.4). To be more specific, we gradually reduced (with an incremental step of 20%) the settling velocity by up to 80%, with the corresponding runs named as URx (x corresponds to the reduction in percentage terms). Under such theoretical conditions, it is expected that the giant dust particles will be suspended for longer periods and that they will be transported at larger distances than the current state-of-the-art models simulate, failing to reproduce what is observed in the real world. Based on these sensitivity experiments, we defined a constant (by percentage) relevant reduction of the particles' settling, which in its absolute value varies with size. Therefore, it is more similar to the effects that are related to aerodynamic forces due to the non-spherical shape and the orientation of the suspended dust particles (Ginoux, 2003b; Loth, 2008; Zastawny et al., 2012; Shao et al., 2017; Sanjeevi et al., 2018; Mallios et al., 2020).

~~In addition, we investigate the implications of a possible mechanism to counteract gravitational settling in order to reduce the differences between the CONTROL run calculations and the in situ observations (shown in Sect. 3.4). To this end, we perform additional sensitivity tests by reducing the settling velocity by 20 to 80%, with a step size of 20%. The experiments are referred to as the "Urx experiment", using the percentage (x%) by which the settling velocity is reduced. With this artificial tuning, we aim to reproduce the net force acting on dust particles falling into the atmosphere and overcome the current shortcomings of the model (i.e., the absence of all real forces that determine the lifetime of dust particles in nature).~~

~~It should be noted that several studies have pointed out the importance of fine-resolution dust simulations (Solomos et al., 2012; Basart et al., 2016; Gu et al., 2021;), which, among other things, help the model resolve small-scale dynamics and account for possible interactions between different scales. Given the complicated meteorological conditions during the study period (i.e., August 2015), the fine resolution increases the accuracy of the dust simulations and provides a good estimate of the magnitude of the missing mechanism. The reduced deposition of particles can be attributed to either an updraft counteracting gravity or a reduction in particle settling velocity, both of which slow dust deposition rates. In the first case, this~~

Μορφοποιήθηκε: Εσοχή: Πρώτη γραμμή: 1,27 εκ.

~~can be attributed to either as yet unresolved meteorological conditions (e.g., small-scale haboobs, dunes) or atmospheric feedbacks due to dust-radiation interactions (i.e., atmospheric heating due to absorption of solar radiation by mineral particles). Lower settling velocities may be related to higher aerodynamic forces due to the non-spherical shape and orientation of dust particles (Ginoux, 2003b; Loth, 2008; Zastawny et al., 2012; Shao et al., 2017; Sanjeevi et al., 2018; Mallios et al., 2020;), or upward electric forces acting on dust particles (Ulanowski et al., 2007; Daskalopoulou et al., 2021; Mallios et al., 2021;).~~ Finally, ~~The~~ the full list of the performed experiments ~~performed can be found~~is given in Table 3.

2.1.4 Dust extinction coefficient ~~and dust optical depth~~

For the evaluation of the model mid-visible (550 nm) dust extinction profiles the corresponding products from the Lidar climatology of Vertical Aerosol Structure for space-based lidar simulation studies (LIVAS) dataset is used as reference. For the spatiotemporal matching between the modelled and the observed dust extinction, we first project the two datasets onto a common horizontal grid, by converting the model outputs from their native horizontal grid spacing (15 km x 15 km) to the structured 1°x1° equal lat-lon grid of LIVAS. The model extinction coefficient for each size bin k ($EC_{550,k,n,l}$) is then calculated at each grid cell n and within each model level l, as shown in Eq.13.

$$EC_{550,k,l,n} = \sum_1^k \frac{3}{2\rho_k D_{eff,k}} M_{n,k,l} Q_{ext550,k}, \quad (13)$$

where $M_{n,k,l}$, ρ_k, $D_{eff,k}$ and $Q_{ext550,k}$ are the grid cell dust mass concentration in g/m^3, the particle density in g/m^3, the effective diameter in m, and the extinction efficiency factor at 550 nm, of size bin k.

$Q_{ext550,k}$ is calculated using the Mie scattering code (Mie, 1908), considering spherical dust particles, and a refractive index of 1.55 + i0.005, which is representative of dust (e.g. Dubovik et al., 2002). Although the extinction coefficient values for spherical particles may be different from the extinction coefficient values of the dust particles, which have irregular shapes, to our knowledge there is no data available for the extinction coefficient of the latter. The extinction coefficient values of spheroidal shapes, commonly used as a proxy of the dust shapes, are not substantially different compared to the spherical particles (Tsekeri et al., 2022), at least when considering the aspect ratios measured for dust particles in Sahara (Kandler et al., 2009). For simplifying the computations, we assume that the particles in each size bin have the same size (i.e. $D_{eff,k}$), and thus the same $Q_{ext550,k}$. In vertical, the fine resolution LIVAS dust extinction coefficient is rescaled (averaging) to match the model layers vertical margins. In the time dimension, the model outputs at the closest lead times to the satellite overpass are selected. ~~In Sect. 3.5, we compare the model calculations of dust extinction at 550 nm with the product of the pure dust extinction coefficient from the Lidar climatology of Vertical Aerosol Structure for space-based lidar simulation studies (LIVAS). To this end, we first project the two data sets (model and LIVAS) onto a common horizontal grid. We thus convert the 15-km horizontal grid of the model output to a 1°x1°-degree grid to match the ~111km horizontal grid of LIVAS. The~~

Μορφοποιήθηκε: Εσοχή: Πρώτη γραμμή: 1,27 εκ.

~~model extinction coefficient for each size bin k ($EC_{550,k,n,l}$) is then calculated for each horizontal grid box n and for each model level l, as shown in Eq.16.~~

$$EC_{550,k,l,n} = \sum_{1}^{k} \frac{3}{2\rho_k D_{eff,k}} M_{n,k,l} Q_{ext550,k}, \quad (16)$$

~~where $M_{n,k,l}$, ρ_n and $D_{eff,k}$ are the dust mass concentration in g/m^3, the particle density in g/cm^3, and the effective diameter in μm of size bin k. $Q_{ext550,k}$ is the extinction efficiency at 550 nm, calculated using the Mie scattering code (Mie, 1908), considering a spherical shape for the dust particles, and a refractive index of 1.55 + i0.005, which is representative of dust (e.g. Dubovik et al., 2002). For simplification of the computations, we assume that the particles in each size bin have the same size (i.e. $D_{eff,k}$), and thus the same $Q_{ext550,k}$. Along the vertical direction, the LIVAS dataset is collocated to the coarser model grid, by averaging across the margins of each model vertical grid box.~~

~~The DOD at 550 nm is computed for every horizontal grid box n of the model, as shown in Eq. 17. For the evaluation of the calculated DOD, we use the ModIs Dust AeroSol (MIDAS) DOD product (see Sect. 2.2.3), after applying the following spatiotemporal collocation: First, the calculated DODs are re-projected on an equal-lat-lon grid, with 0.4° x 0.4° grid. The DOD is provided by WRF on an hourly basis without spatial gaps, in contrast to MIDAS DOD, which is available at swath level with a viewing width of 2330 km, along the MODIS-Aqua polar orbit, at 5-minute segments (see Gkikas et al., 2021) for further details). The MIDAS swaths are re-projected on the horizontal grid of the WRF, with 0.4° x 0.4° grid spacing. Then, the WRF outputs that are closer to the Aqua satellite overpass time, are used to calculate a weighted-average WRF DOD, only for WRF grid cells with coincident MIDAS DODs, by taking into account the absolute difference between WRF forecast time and Aqua overpass time.~~

$$DOD_{550,n} = \sum_{1}^{k} \frac{3}{2\rho_k D_{eff,k}} M_{n,k} Q_{ext550,k}, \quad (17)$$

Μορφοποιήθηκε: Εσοχή: Πρώτη γραμμή: 1,27 εκ.

2.2 Observational datasets

2.2.1 Airborne in situ observations

During the FENNEC field campaign in 2011 (Ryder et al., 2013b, 2013a) and the AER-D field campaign in 2015 (Ryder et al., 2018, 2019), airborne in situ observations were collected with the FAAM BAE research aircraft. In this study we use size distributions from the FENNEC field campaign, aquired during aircraft profiles over the Sahara (Mauritania and Mali), as described in Ryder et al. (2013a). We select size distributions from "freshly uplifted dust" cases, when dust particles are in the atmosphere for less than 12 h. Additionally, from these profiles we use data from the lowest available altitude, centered at 1km, covering altitudes between 0.75 to 1.25km. The derived PSD is depicted in Fig.2(a), hereafter referred to as the "observed FENNEC-PSD". Error bars in Fig.2(a) indicate the standard deviation of the observed values across the profiles

and altitudes we used. The instrumentation for those measurements was the Passive Cavity Aerosol Spectrometer Probe (PCASP, 0.13-3.5 μm), the Cloud Droplet Probe (CDP, 2.9-44.6 μm), using light scattering measurements and assuming a refractive index (RI) of 1.53-0.001i (which is constant with particle size), spherical shape for the particles, and using Mie calculations to convert from optical to geometric diameter, as well as the Cloud Imaging Probe (CIP15, 37.5-300 μm)). The instruments and data processing are described in Ryder et al. (2013a). The midpoint size bin diameters do not overlap, though there is some overlap in bin edges between the instruments. A fit on the observations is provided in Figure 2a (the "fitted FENNEC-PSD" with solid red line), which is used in the parameterization of the emitted dust, as described in Section 2.1.1, to modify the GOCART-AFWA dust scheme in WRF.

We also use PSD observations during horizontal flight legs at a constant height (referred either as RUNs or flight segments) over the Atlantic Ocean during AER-D. We use measurements taken with PCASP (D =0.12-3.02 μm) for fine dust particles. For the coarse and giant mode of dust we used measurements from CDP (D=3.4-20 μm - although CDP measurements availability extends up to 95.5 μm as it is explained below) and the two-dimension Stereo probe (2DS, D = 10–100 μm - although the instrument measures up to 1280 μm few particles larger than 100μm were detected). For the light scattering techniques of PCASP and CDP, a RI = 1.53-0.001i is assumed for the conversion of the optical to geometric diameter (as in FENNEC 2011 campaign). CDP observations extend up to the size of 95.5 μm, thus data from CDP and 2DS partly overlap in their size range. Since 2DS observations are more reliable in the overlapping size range, we used the CDP observations for particles with sizes up to 20 μm. Also, 2DS-XY observations are preferred over the 2DS-CC, since they better represent the non-spherical particles. A more detailed description of the in-situ instruments and the corresponding processing of the data acquired during the AER-D campaign is included in Ryder et al., (2018). The error bars represent the total (random and systematic) measurement error due to the counting error, the discretization error, the uncertainties in the sample area and the uncertainties in the bin size due to Mie singularites (Ryder et al., 2018). All PSD measurements are at ambient atmospheric conditions. The locations of the flights of AER-D used in this study are depicted in Fig.3.

~~The airborne in situ measurements used in this study, were collected during the FENNEC and the AER-D campaigns. Both campaigns employed the FAAM BAE 146 research aircraft, equipped with similar instrumentation for measurements of the dust PSD. During the FENNEC campaign the flights were performed above the Sahara dust sources, above Mauritania and West Mali, while during the AER-D campaign the flights were performed away from the dust sources, in the vicinity of Cape Verde and Canary Islands. The trajectories of AER-D flights and the approximate locations of each run (i.e. near-horizontal flight segment) are depicted in Fig.3. The suite of airborne in situ instruments included the Passive Cavity Aerosol Spectrometer Probe (PCASP) and the Cloud Droplet Probe (CDP), alongside with either the Cloud Imaging Probe 15 (CIP15), or the 2-D Stereo probe (2DS). During the FENNEC campaign, the measurements provided PSD data for diameters up to 300μm, while during the AER-D campaign, the PSD was provided for particles with diameters up to 200μm. Full details of instrumental measurements and processing are given by Ryder et al., (2013b) and Ryder et al., (2018), for FENNEC and AER-D, respectively. In Sect. 2.1.1 we describe the way that FENNEC campaign measurement used in this study.~~

2.2.2 LIVAS product

For the validation of the vertical distribution of dust from the model (see Sect. 3.5), we utilize the pure-dust profiles provided by the LIVAS dataset, originally presented in Amiridis et al. (2013; 2015) and updated in Marinou et al. (2017). The LIVAS pure-dust product is a global dataset, covering the period between 06/2006 and 05/2020, and is provided a) on per-granule level with similar resolution to the original Cloud-Aerosol Lidar and Infrared Pathfinder Satellite Observations (CALIPSO) L2 profile products (i.e., 5 km horizontal and 60 m vertical), and b) as a global three-dimensional database of monthly-mean averaged profiles of aerosol properties, on a uniform horizontal grid spacing of 1° × 1°. LIVAS was developed applying the dust-separation technique described in Tesche et al., (2009) on the CALIPSO level 2 version 4 products (Winker et al., 2009). The LIVAS pure-dust product has been used to a variety of dust-oriented studies including the investigation of the dust sources and the seasonal transition of the dust transport pathways (Marinou et al., 2017; Proestakis et al., 2018); the evaluation of the performance of atmospheric and dust transport models (e.g. Tsikerdekis et al., 2017; Solomos et al. 2017; Georgoulias et al., 2018; Konsta et al., 2018), the evaluation of new satellite-based products (e.g. Georgoulias et al., 2016; Chimot at al. 2017; Georgoulias et al., 2020; Gkikas et al., 2021), and on dust assimilation experiments (Escribano et al., 2021). Herein, the LIVAS pure-dust extinction product is used for the assessment of the simulated dust vertical patterns. In the geographical region of our study, the uncertainty of the product is estimated to be less than 20% in altitudes up to 6km (Marinou et al. 2017).

~~### 2.2.3 MIDAS product~~

~~For the assessment of the simulated horizontal dust patterns (see Sect. 3.2), the recently-developed MIDAS dataset (Gkikas et al., 2021) has been utilized. MIDAS has been produced via the synergy of the quality-filtered MODIS aerosol optical depth (AOD, Collection 6.1, Level 2) and the fraction of AOD attributed to dust (MDF), provided by the Modern-Era Retrospective Analysis for Research and Applications (MERRA-2 version 2; Gelaro et al., 2017). According to the applied methodology, the columnar DOD at 550 nm is derived at fine spatial grid spacing (0.1° x 0.1°), along with its associated uncertainty (see Sect. 3 in Gkikas et al., (2021)). MIDAS DOD has been evaluated versus AERONET AOD retrievals (Giles et al., 2019), in which the contribution of non-dust aerosol species has been minimized. In the region of interest of the current study (i.e., West Sahara and eastern Tropical Atlantic Ocean), MIDAS DODs covariate (R ~0.90) very well with AERONET-derived DODs, although they are slightly overestimated by <0.04 (see Fig. 4 in Gkikas et al., (2021)). Moreover, the intercomparison of MIDAS, LIVAS and MERRA-2 DODs show a remarkable consistency in reproducing the seasonal cycle of dust loads over the W. Sahara and the eastern segment of the Tropical Atlantic Ocean. Overall, the MIDAS dataset is quite useful for the current study, due to the high reliability of the derived DOD product and the product availability at fine spatial resolution, on a daily basis.~~

Μορφοποιήθηκε: Εσοχή: Πρώτη γραμμή: 1,27 εκ.

~~2.2.4 MSG-SEVIRI-DUST RGB product~~

~~We use the Meteosat Second Generation - Spinning Enhanced Infrared and Visible Imager (MSG-SEVIRI) DUST RGB product, which is produced by the RGB colors (Red-Green-Blue), corresponding to the three infrared channels of the MSG-SEVIRI instrument. The functionality of the geostationary SEVIRI sensor in the infrared area of the electromagnetic spectrum, and the combination of the different sensitivities of the three channels, enables both daytime and nighttime continuous observations, along with the discrimination between land, clouds and aerosols, making the Dust RGB product very useful for monitoring intense dust and volcanic ash plumes. Dust particles are depicted on images as bright magenta (during day) or purple color (during night) over land, and as a magenta color over the sea.~~

3 Results

3.1 Settling Velocities

Figure 4 shows the altitude profiles of the settling velocities for each size bin from the CONTROL run, averaged over the simulation domain, and the ~~simulation~~ period of interest. ~~As the size gets bigger the~~S ~~s~~ettling velocity is increase~~s~~ for larger mineral particles.~~d~~. The ~~Terminal~~ terminal velocities ~~of~~ for particles ~~of~~ within bin 5 are two orders of magnitude ~~greater~~ higher than ~~the particles of~~those in bin 2 and bin 3, and one order of magnitude ~~greater than the particles of~~with respect to bin 4. An altitude dependency, regulated by the thermodynamic state of the atmosphere, of the terminal velocities is also apparent in Figure 4, showing that they increase with height due to the reduction either of temperature or air density (Eqs. 10 and 13)~~The terminal velocities increase with height following the temperature lapse rate, and are sensitive to the thermodynamic condition of the atmospheric air, increasing as temperature or air density drops, based on Eq.10, 13 and the relationships of air viscosity.~~ For the CONTROL run ~~T~~the average settling velocities ~~for the CONTROL run~~ near the surface are lower by approximately 10% than ~~differ from~~ those at 6 km height, ~~by approximately 10 %,~~ and this non-negligible reduction can be critical, particularly ~~which is a significant reduction, especially~~ for coarser and giant particles where velocities are ~~greater~~higher.

3.2 Dust above the sources

In Fig. 5 we present how the PSD varies with height above an emission point (latitude=24.9° and longitude=9.2°) in Mali, on 11/08/2015 at 14UTC. The model PSDs are only from that grid model box interpolated at 1, 2, and 3 km height and for the particular timestep (11/08/2015 at 14UTC). The red squares correspond to the "observed FENNEC-PSD" sorted into the five bins. The error bars provide the maximum and minimum limits of the "observed FENNEC-PSD", sorted into the five model size bins, after including the standard deviation of "observed FENNEC-PSD". The "observed FENNEC-PSD" (see Section 2.2.1) has been derived from several flights above dust sources, thus it is representative of the PSDs above Sahara sources and it used here as reference. The black squares depict the "fitted FENNEC-PSD" sorted into five bins, used in the model parameterization to calculate the emitted dust mass of the corresponding five model transport bins. The difference

Μορφοποιήθηκε: Εσοχή: Πρώτη γραμμή: 1,27 εκ.

Μορφοποίησε: Γραμματοσειρά: Όχι Πλάγια, Αγγλικά (Ηνωμένων Πολιτειών)

between the “fitted FENNEC-PSD” and the “fitted FENNEC-PSD” occurs due to the fitting process. The modelled volume concentration is reduced with height by an order of magnitude between 2 and 3 km for particles with diameters 17-40 μm (bin 4). At 3km the simulated concentrations of particles in bin 4 and bin 5 are very low compared to the measurements in Fig. S2a of Ryder et al., (2013a) which indicate the removal of giant particles above 4 km (Ryder et al., 2013a, Figure S2a). Although a direct comparison between the modelled and the observed PSD for this particular emission point is not feasible, since the FENNEC campaign took place on different dates than the AER-D and there are no available measurements above dust sources for the period we performed our simulations, we note a modification of the PSD shape, both for model and observations at 1km. It is evident that the model overestimates the PSD for bins 1-3 while the opposite is found in the size spectrum of the super-coarse (bin4) and giant (bin5) dust particles. Therefore, a model weakness is revealed at the very early phase of the dust transport. Those differences can be attributed to an overestimation of their loss during uplift from the surface to 1 km, or to higher updrafts that remain unresolved in our numerical experiment. Another possible source of this underestimation could be the utilization of a not well-defined PSD shape constraining the distribution of emitted dust mass to the model transport size bins. The use of a PSD with a higher contribution of coarse and giant dust particles could possibly improve the representation of the coarse and giant particles aloft (Fig. S2 and S3) and can be assessed in future studies. Additionally, comparing the “observed FENNEC-PSD” with the modelled PSD of the scenario with the maximum relative reduction of the settling velocities (UR80) in Fig. 5, we find a significant increase of the modelled volume concentrations, reducing the differences seen in volume concentrations in bin4 and bin5 without the reduction of the settling velocity, although the underestimation in bin 5 is still evident.

~~Figure 5 shows the change of the dust volume PSD with height above an emission point in Mali, on 12/08/2015, with the dust concentration reducing considerably for heights greater than 2 km. This point is in the area of intense emissions, observed both from satellites and the model. The area of Mali is also suggested by Ryder et al. (2013) as one of the dust sources of the dust plume that measurements of flight b928 were taken. Fig. 5 shows how the concentration of every size bin of the model is reduced with increase in altitude. The reduction is more evident for the particles of bin 4 and bin 5, where the volume concentration is reduced over an order of magnitude between 2 and 3 km. Particles of bin 4 and bin 5 are removed very quickly with height and are found in low concentrations at heights up to 4 km in the model simulations (not shown).~~

~~A direct comparison between the modelled and the observed PSD for the dust concentration above the sources, cannot be conducted for the AER-D campaign, since the measurements were only performed over the ocean. Figure 5 shows a more qualitative comparison, using the observed FENNEC PSD at 1km (red squares). The modelled and observed PSD differ. The modelled volume concentrations have larger values for bins 1-3, and lower for bins 4 and 5. The maximum concentration of the modelled PSD is at bin 3, whereas for the observed PSD is at bin 4, suggesting that the model underestimates the concentrations at bins 4 and 5, already from the initial transport stage, near the dust sources. Those differences can be attributed either to an underestimation of the contribution of the coarser particles on the emission, to an overestimation of their loss during transport from the surface to 1 km, or to higher updrafts that remain unresolved in the simulation of this study.~~

Μορφοποίησε: Γραμματοσειρά: Όχι Πλάγια

Μορφοποίησε: Γραμματοσειρά: Όχι Πλάγια, Αγγλικά (Ηνωμένων Πολιτειών)

3.3 Mean dust load ~~and spatiotemporal distribution of dust~~

In Fig. 6, the spatial patterns of the columnar dust concentrations are depicted, averaged over the period of 5/8/15-25/8/15, for the total mass as well as for each one of the five size bins simulated with the CONTROL run. Among the first three bins, there are evident many similarities of the dust load spatial features, with maximum values in the Western Sahara whereas the dust advection pathways towards the Atlantic Ocean are clearly seen. In terms of intensity. The mass increases from bin1 to bin 3 (5.5 – 17 μm), yielding the maximum values throughout the size ranges. Dust particles with diameters between 17 μm and 40 μm (bin 4) are found mainly over land, and are subjected to short-range transport westwards (i.e., off the Moroccan coast). Giant particles (bin 5) are found at very low concentrations (< 0.5 gr m^{-2}), at isolated areas over/near dust sources, since the strong impact of gravitational settling prohibits their accumulation and transport.

~~In order to further demonstrate the distribution of the total dust mass at the different sizes, Fig. 6 shows the simulated fields of the total columnar dust load, along with the corresponding concentrations at each size bin. The simulations in Fig. 6 are performed using the parameters of the CONTROL experiment, and the calculated concentrations are averaged over the period of interest (5-25/8/15). For the first three bins, the spatial patterns of dust load are very similar, showing the dust sources in the Western Sahara, and the advection of the particles towards the Atlantic Ocean. The mass increases from bin1 to bin 3 (5.5 – 17 μm), which has maximum values for the whole size range. Dust particles with diameters between 17 μm and 40 μm (bin 4) are found mainly over land, and are subjected to short-range transport westwards (i.e., off the Moroccan coast). Giant particles (bin 5) are found at very low concentrations (< 0.5 gr m^{-2}), at isolated areas over/near dust sources, probably due to their quick gravitational settling.~~

~~The comparison of the model simulations with satellite retrievals shows that, in general, there is a good agreement on the spatiotemporal distribution of dust during the days and times of the AER-D flights. Deviations between the simulations and the observations are found for flight b920, due to a shift of the center of the simulated dust mass towards the south (Fig. 7(a)). Moreover, the observations show that the dust plume traveled towards Morocco and Canary Islands, whereas the model shows that it traveled mainly towards Cape Verde (see Dust RGB image of MSG-SEVIRI, during the time of flight b920 in Fig.7(b), and the MODIS DOD and corrected reflectance in Fig. 7(c) and 7(d), respectively). This difference results in an overestimation of the simulated dust mass in the area of South West Africa and West Mauritania, affecting the transport towards the area of flight b920. The main cause for this discrepancy is the difference in the intensity by which the various dust sources in Northern Algeria were activated during the previous days. As it is depicted in Fig. 7(e, f) there are sources in the model that have been strongly activated in circles A and B, although in RGB-Dust MSG-SEVIRI images they are depicted with much less intensity (fewer pink colors). That deficiency of the model could be attributed to various reasons, such as underrepresentation of the meteorological conditions mostly in cases of haboobs (Ryder, 2018a, 2021) which are responsible for the dust erosion, possibly due to a not so sophisticated microphysics scheme or missing smaller scale processes. For those reasons, b920 is excluded from the statistical analysis in Sect. 3.4.~~

Μορφοποιήθηκε: Εσοχή: Πρώτη γραμμή: 1,27 εκ.

3.4 Dust size distribution

Figure 7 illustrates the simulated PSDs, from each experiment (i.e., CONTROL and URx), along with those acquired by the airborne in situ measurements at different segments and altitudes of the flight b928 in the surrounding area of Cape Verde (downwind region). For the other AER-D flights (i.e., b920, b924, b932 and b934) similar findings are drawn and for brevity reasons are omitted here and are included in the supplementary material (Fig.S4). All AER-D measurements demonstrate the impacts of the processes that are associated with dust transport. The red squares represent the observations and the error bars represent the total (random and systematic) measurement error (see Sect 2.2.1). The modelled PSDs are collocated in space and time with the measurements of each flight segment. For each flight segment, we extract the modeled PSD by interpolating the dust field to the specific altitude of the flight RUN. Additionally, we average the dust field of the nearest grid cell to each coordinate pair along the flight segment track, and the eight neighbouring grid cells of the same altitude. The coordinates of the flight leg track are depicted with orange dots and the collocated grid points used for deriving the modelled PSD (at the specific height of each flight leg) with blue dots. In the time dimension, we average the two hourly model outputs that contain the times of the measurement. In case that the time of measurement coincides with the exact hourly output, the model output on that hour along with the outputs prior and after that are averaged. The error bars in the model PSDs indicate the standard deviation of the collocated grid points averaging in space and time.

Based on our findings, for the CONTROL run, the model performs considerably well particularly near the surface and above 4 km, reproducing the volume concentration of the particles residing within bins 1 and 2. Underestimations are found for the third bin with the simulated volume concentration falling however within the measurement uncertainties envelope. As expected, for bins 4 and 5, the model is not capable of reproducing the observed PSD at distant areas since quite significant underestimations have been already notified above sources (see Fig. 5a). The reduction of the settling velocity (i.e., URx runs, see Table 3) has negligible impact on the level of agreement between model and observations for bins 1 and 2, moderate for bin3 while is determinant for the super-coarse (bin 4) and giant (bin 5) dust particles. Nevertheless, for achieving the best model-observations matching, the necessary reduction (expressed in percentage) on the settling velocity is not constant among the defined transport bins. Focusing on bins 4, the UR60 run (i.e., reduction of the settling velocity by 60%) outperforms the other numerical experiments and focusing on bin 5 the UR80 run.

The overall comparison of the observed and modelled average PSDs is presented in Fig 8. We are considering all the in situ airborne measurements and the WRF-L numerical outputs satisfying the defined spatiotemporal collocation criteria. Error bars indicate the corresponding standard deviation. Figure 8a shows that the best model performance is found for the UR80 experiments resembling satisfactory the bin 4 and bin 3/5 concentrations, respectively. These “artificial” reductions translate to settling velocities equal ~0.066 for bin 3 (D=5.5-17 μm), ~0.32 m/s for bin 4 (D=17-40 μm) and ~1.88 m/s for bin 5 (D=40-100 μm). it is also reminded that for the same experiment it has been achieved the best agreement against the FENNEC-PSD above dust sources (see Fig. 5 and the relevant discussion).

An alternative comparison between observations and model volume concentrations, for the selected AER-D samples (each flight segment is denoted with different marker), has been performed and the obtained results, at each flight altitude, are depicted in Figure 8b. More specifically, we calculate for each model experiment (denoted with different colour), the relative differences (expressed in percentage) of the total dust volume concentration with respect to the in-situ measurements. In addition, the corresponding differences (in percentage terms) that are representative for the altitudes spanning from near-surface up to ~4.2 km are denoted with the vertical coloured dashed thick lines (WRF-L experiments). Those differences are derived by averaging the relative differences of each flight segment. Overall, the model tends to underestimate the total dust volume concentration (relative differences up to 100% in absolute terms) even though occasionally positive departures are found, as indicated by the spread of the individual biases around zero. Nevertheless, the main finding from this analysis is that the model-observation declinations reduce when the settling velocity reduces too (i.e., URx runs). Among the WRF-L experiments, the minimum biases (~5%) are obtained for the UR40 scenario (i.e. the vertical orange dashed line resides close to zero). Through the inspection of the vertically resolved "behavior" of the individual runs, it is revealed that in some cases the model-observation biases can be minimized for the UR60 and UR80 runs and this "variability" highlights the complexity of the underlying mechanisms governing the suspension of airborne dust.

~~The model PSDs are collocated in space and time with the measurements of each flight segment. To extract the model PSDs, after interpolating the model dust concentrations fields to the specific height of the flight run, we average the dust concentrations of the eight neighboring grid points to the grid point with the nearest latitude and longitude of each flight segment. The performance of the model is similar for the flights b924, b932 and b934. Figure 8 shows the comparison of the CONTROL run with the airborne in situ measurements of flight b928. The model adequately reproduces the volume concentration of the particles for bins 1 and 2, although the agreement is better near the surface and above 4 km. The model underestimates the volume concentration of bin 3, with the simulated values to be within the measurement uncertainties. It also underestimates the volume concentrations of bins 4 and 5, as expected, since the underestimation happens also near the sources, as shown in Fig. 5(a). Considering the different experiments for reduced settling velocities (Table 3), we see that the reduction mainly affects the simulations for the coarser particles (bins 3, 4 and 5), with the effect increasing with the size of the particles. The simulated concentrations of giant particles (bin 5) become significant when the reduction in settling velocity is greater than 60%. The comparison of the observed and modelled mean average PSDs in Fig. 9(a) shows that UR60 and UR80 experiments are closer to the observations, with UR80 to better reproduce the observed values of bins 3 and 5, whereas UR60 better reproduces the values of bin 4. This reduction results in settling velocities of ~0.066 m/s for bin 3 (D=5.5-17 μm), ~0.32 m/s for bin 4 (D=17-40 μm) and ~1,88 m/s for bin5 (40-80μm). In general, UR80 simulations of the mean PSD provide the best agreement with the observations. In terms of total volume, the UR80 simulations have the smallest relative difference with the observations for most flights, providing a ~50% improvement in relative difference, as it is depicted in Fig. 9(b). UR80 also provides better agreement with the observed FENNEC PSD above the dust sources, by shifting the maximum of the PSD to bin 4 (Fig. 5).~~

Μορφοποιήθηκε: Εσοχή: Πρώτη γραμμή: 1,27 εκ.

3.5 Dust vertical distribution

Figure ~~10~~9(a) shows the profile of the mean extinction coefficient at 532 nm, provided by the LIVAS pure-dust product (black line), and the profile of the mean extinction coefficients at 550 nm, provided by the CONTROL, UR20, UR40, UR60, and UR80 experiments. The orange area indicates the standard deviation of the LIVAS profiles. Figure9(b) depicts the mean absolute model bias with respect to LIVAS profiles for the different simulations and the vertical dashed lines show the corresponding bias averaged over different altitudes. The mean LIVAS profile is provided by averaging the night-time profiles over the region between 25.5oW to 12.5oE and 11.5oN to 35.5oN, during 5 to 25 August 2015. This area includes the main dust sources that affected the vicinity of Cape Verde (Ryder et al., 2018) and the region of the dust outflow over the Ocean, as well. The nighttime profiles excel in accuracy over the daytime ones, due to the lower signal-to-noise ratio (SNR) during the night. The model profiles are collocated in space and time with the LIVAS profiles, as described in Sect. 2.1.4 and the model extinction coefficient is provided with the Eq.13.

The intercompared profiles are in good agreement, with the simulations falling well-within the variability of the dust observations, although discrepancies are also present, especially close to the dust sources, in the nighttime boundary layer (Fig.9(b) – region I), and within the upper free Troposphere (Fig. 9(b) – region III). The assessment of the different model experiments against the ESA-LIVAS pure-dust product is performed in the region between 1.5 km and 6.4 km a.m.s.l. (Fig. 9 – region II), to avoid possible biases propagating into the analysis (i.e., complex topography and surface returns-region I, SNR and tenuous aerosol layers – region II). ~~This comparison is an initial demonstration of the good initialization and performance of the different model experiments, with respect to capturing the vertical distribution of dust. The intercompared profiles are in good agreement, with the simulations falling well-within the variability of the dust observations, although discrepancies are also present, especially close to the dust sources, in the nighttime boundary layer (Fig.10(b) – region I), and within the upper free Troposphere (Fig. 10(b) – region III). The discrepancies close to the dust sources are attributed to the complex topography, in terms of geographical characteristics (Proestakis et al., 2018), weighting effects, surface returns, and representativeness issues related to the aggregation of CALIPSO L2 profiles to LIVAS 1°x1° grid resolution (Amiridis et al, 2013, Marinou et al., 2017). The discrepancies in the upper free Troposphere (above 6 km) are attributed to the presence of tenuous aerosol layers which fall below the CALIOP layer detection threshold. Thus, the assessment of the different model experiments with the LIVAS pure-dust product, is performed in the region between 1.5 km and 6.4 km a.m.s.l. (Fig. 10 – region II).~~

According to the comparison of observations and simulations of the mean extinction coefficient (Fig. ~~9~~10(a)), the statistical overall analysis reveals that the UR40 experiment demonstrates a better performance compared to LIVAS, reducing the mean bias close to zero. For the same experiment the minimum mean bias with respect to the total volume concentration is achieved (see discussion of Fig.9b in Sect. 3.4). However, the UR80 experiment provides a more constant (positive) bias with height, which suggests a better distribution of the dust mass in the vertical.

Μορφοποιήθηκε: Εσοχή: Πρώτη γραμμή: 1,27 εκ.

4 Discussion ~~and Conclusions~~

The frequent presence of large desert dust particles (D>20 μm) far from their sources, is well established by numerous observational studies over the last decade (van der Does et al., 2018; Liu et al., 2018; Ryder et al., 2013, 2018, 2019a; Weinzierl et al., 2009, 2011, 2017b). However, the processes that result in the particle retainment in the atmosphere, and subsequently their travel at greater distances than predicted, remains unrevealed. In this study we extend the particle size range applied in the transport parameterization of the GOCART-AFWA dust scheme of WRF, to include particles with diameters up to 100 μm. The evaluation against airborne in situ observations of the size distribution shows that the concentrations of the larger particles are underestimated, both above dust sources and distant areas. This suggests that there are atmospheric processes that are not taken into account in the model simulations. We investigate the effect of reducing the settling velocity of the dust particles due to these unknown processes, and we see that for a reduction of 60% and (especially for) 80%, the simulations of the PSD in Cape Verde are improved with respect to the observations. The reduction of 80% corresponds to a reduction in settling velocity of 0.0066 m/s for particles with D between 5.5 and 17 μm, which is double than the value reported by Maring et al. (2003) for similar sizes. It should be noted though that Maring et al. (2003) derived this settling velocity using observations that were taken with a five-year difference. Ginoux (2003), has also reported an improvement in model simulations for a reduction in settling velocity of approximately 45% and 60%, for particles with diameters 10 to 30 μm. Though, the differences in the model resolution, the dust scheme and the drag coefficient in Ginoux (2003) compared to this study, could cause the different values of the required corrections in the settling velocities. The difference with the values suggested herein, can mainly be attributed to the different drag coefficient used in Ginoux (2003), which results in lower settling velocities for the spherical particles. Meng et al. (2022) performed a study, similar to this, where after reducing the settling velocity by 13% for accounting for particles' asphericity based on Huang et al., (2020), performed sensitivity tests reducing the dust particles' density from 2500 kg m^{-3} to 1000, 500, 250 and 125 kg m^{-3}. They found that a decrease in the modelled dust aerosol density by 10-20 times its physical value (2500 kg m^{-3}) is needed to improve the comparison between the model and the long-range dust observations of coarse particles. A 10 times reduction in particles' density is almost equal to a 90% reduction in the settling velocity (starting from the Clift and Gauvin (1971) drag coefficients and assuming conditions of U.S. Standard Atmosphere, Fig Sx). It is clear that a huge reduction in the settling velocity in both the Meng et al., (2022) methodology and this work is required, although the physical processes occurring to explain this reduction are not clear.

One of the processes proposed in the literature to explain the longer atmospheric lifetimes of large mineral dust particles is the particle asphericity. Ginoux (2003) compared randomly-oriented prolate spheroids and spheres of the same cross section. They showed that spheroids fall slightly slower than their spherical counterparts, with their difference being negligible for spheroids with aspect ratio values less than 5. Huang et al. (2020) compared randomly-oriented ellipsoids and spheres of the same volume. They showed that ellipsoids fall around 20% slower than spheres. Mallios et al. (2020) compared prolate spheroids and spheres of the same maximum dimension, and of the same volume. Moreover, they did not assume randomly-oriented particles, but particles of specific orientation (horizontal and vertical). They showed that the results of the

Μορφοποίησε: Εκθέτης
Μορφοποίησε: Εκθέτης
Μορφοποίησε: Εκθέτης
Μορφοποίησε: Γραμματοσειρά: Όχι Πλάγια
Μορφοποιήθηκε: Βασικό, Αριστερά, Εσοχή: Πρώτη γραμμή: 1,27 εκ., Διάστημα Μετά: 0 στ., Διάστιχο: μονό, Περίγραμμα: Επάνω: (Χωρίς περίγραμμα), Κάτω: (Χωρίς περίγραμμα), Αριστερά: (Χωρίς περίγραμμα), Δεξιά: (Χωρίς περίγραμμα), Μεταξύ : (Χωρίς περίγραμμα)
Μορφοποίησε: Γραμματοσειρά: Όχι Πλάγια
Μορφοποίησε: Γραμματοσειρά: Όχι Πλάγια

comparison change when the maximum dimension or the volume-equivalent size is used in the comparison. Prolate spheroids, with aspect ratio values in the range of 1.4-2.4, fall slower than spheres of the same maximum dimension, regardless of orientation, with the relative difference between the settling velocities reaching the value of 52%. On the other hand, prolate spheroids, in the same aspect ratio value range, fall faster than spheres of the same volume, regardless of orientation. The comparison with in situ observations of the maximum dimension of particles is not so common, since most of the in-situ measurements do not provide the sizing of the particles in terms of their maximum dimension, with some exceptions, as e.g. the observations shown in van der Does et al. (2016) of individual giant mineral particles (larger than 100 μm in maximum dimension).

All the above show that more work is needed for the definite and accurate quantification of the particle asphericity effect on their settling. Nevertheless, there are indications pointing that aspherical particles remain in the atmosphere longer, and that asphericity can be one of the reasons for the differences between the modelling results and the observations. Another process that can influence mineral dust settling has to do with the electrical properties of dust particles. The dust particles are charged in the atmosphere either due to the attachment of atmospheric ions on them (Mallios et al. 2021b) or/and due to collisions, a process known as triboelectric effect (Ette, 1971, Eden and Vonnegut, 1973, Mills, 1977, Jayaratne, 1991, Mallios et al., 2022). Moreover, there is a large-scale atmospheric electric field, due to the potential difference between the lower part of the Ionosphere and the Earth's surface (Rycroft et al., 2008). The electric field is modified by ion attachment process (Mallios et al. 2021b) or by the charge separation caused by updrafts (Krauss et al., 2003). Therefore, electrical forces are generated that might influence the particle settling process by balancing the gravity or changing the particle orientation. The quantification of the particles' electrical properties is still an open question

Another possible source of error in the gravitational losses simulated by the model as proposed by (Ginoux, 2003b) is the numerical diffusion in the advection equation of gravitational settling. Since in the GOCART-AFWA dust scheme of WRF (and WRF-L) a first-order upwind scheme is adapted for the gravitational losses, which is rather diffusive, an investigation of the possible improvement on the results by the replacement of the scheme with a less diffusive would be of interest. A possible limitation of this study is the accuracy of the PSD which is used for the distribution on the model transport bins of the emitted fluxes. The simplification in the assumption that the shape of the PSD at 1km above the sources remains unchanged in lower heights near the ground, could possibly introduce errors in the representation of the presence of dust particles aloft.

In any case, the proposed scheme presented here, provides a useful tool for the investigation of the physical processes in the transport of coarse and giant particles, along with their impacts on other physical processes in the atmosphere, such as ice nucleation and radiation interactions. The artificial reduction in the settling velocity is not attributed to a known physical mechanism (although results from the past literature reveal some candidates that can give results on the same order of magnitude). Thus, despite the encouraging results, more research is needed towards understanding the physical or numerical processes driving this finding, including the estimation of the impact of non-spherical particles, electricity, the radiation impact on thermodynamics and the disturbance of the mass balance due to the numerical diffusion.

Μορφοποίησε: Γραμματοσειρά: Όχι Πλάγια, Χρώμα γραμματοσειράς: Μαύρο

Μορφοποίησε: Γραμματοσειρά: Όχι Πλάγια

The frequent presence of large desert dust particles (D>20 μm) far from their sources, is well established by numerous observational studies over the last decade (van der Does et al., 2018; Liu et al., 2018; Ryder et al., 2013, 2018, 2019a; Weinzierl et al., 2009, 2011, 2017b). However, the processes that result in the particle retainment in the atmosphere, and subsequently their travel at greater distances than predicted, remains unrevealed. In this study we extend the particle size range acknowledged in WRF-GOCART-AFWA transport code, to include particles with diameters up to 100 μm. The evaluation against airborne in situ observations of the size distribution shows that larger particles, are underestimated, both above their sources and far from them. This suggests that there are atmospheric processes that are not taken into account in the model simulations. We investigate the effect of reducing the settling velocity of the dust particles due to these unknown processes, and we see that for a reduction of 60% and (especially for) 80%, the simulations of the PSD in Cape Verde are improved with respect to the observations. The reduction of 80% results in settling velocity of 0.066 m/s for particles with D<25 μm, which is double than the value reported by Maring et al. (2003) for similar sizes. It should be noted though that Maring et al. (2003) derived this settling velocity using observations that were taken with a five-year difference. Ginoux (2003), has also reported an improvement in model simulations for a reduction in settling velocity of approximately 45% and 60%, for particles with diameters 10 to 30 μm. Though, the differences in the model resolution, the dust scheme and the drag coefficient in Ginoux (2003) compare to this study, could cause the different values of the required corrections in the settling velocities. The difference with the values suggested herein, can mainly be attributed to the different drag coefficient used in Ginoux (2003), which results in lower settling velocities for the spherical particles.

One of the processes proposed in the literature to explain the longer atmospheric lifetimes of large mineral dust particles is the particle asphericity. Huang et al. (2020) used globally averaged shape distributions of particle aspect ratio and height to width ratio and provided a correction to the spherical particle settling velocity, which is valid for ellipsoidal particles. According to their empirical expression, there is a 20% reduction of particle settling velocity in the case of ellipsoidal particles compared with their spherical counterparts of the same volume. Among the limitations of their methodology (see Huang et al. 2020), is that it is valid only in the Stokes' regime (Re<<1), which limits the applicability of the study for particles with sizes less than 20 μm, and that the ellipsoidal particles are randomly oriented.

Mallios et al. (2021a) derived semi-analytical expressions for the mean orientation angle of prolate spheroids moving vertically in the Earth's atmosphere in the presence of electrical and gravitational forces. They found that the random orientation assumption is, in principle, valid only for particles with size (two times the particle major semi-axis) less than 2 μm, reducing even more the applicability of the methodology by Huang et al. (2020). As the size increases, the gravity or the electrical force tend to create sufficient torque to rotate the particle horizontally or vertically with respect to the ground, respectively (depending on the particle net electrical charge and the large-scale atmospheric electric field).

Moreover, Mallios et al. (2020) provided new expressions for the drag coefficient of prolate spheroids that are valid beyond the Stokes' regime (specifically for Re≤100) and that take into account the orientation and the aspect ratio of the particle. They showed that in the case the aspect ratio ranges between 1.4 and 2.4, prolate spheroids fall faster than their spherical counterparts of the same volume. This is attributed to the projected area of the prolate spheroids, which depends strongly on the particle

orientation (although on average it is larger for ellipsoids than spheres (Vickers, 1996), the projected area of ellipsoids becomes smaller than the projected area of spheres of the same volume as the particle becomes vertically oriented), and the aerodynamic properties due to the impact of the prolate spheroid shape factors on their drag coefficients. They also showed that when comparing prolate spheroids with spherical particles of the same maximum dimension the conclusions are different. In the case of particles with aspect ratio equal to 1.4, the settling velocity of prolate spheroids is on average 6% (in the case of horizontal orientation) up to 23% (in the case of vertical orientation) less than their spherical counterparts (of the same maximum dimension). As the aspect ratio increases to 2.4, the difference becomes 20% (for horizontal orientation) and 52% (for vertical orientation).

Another process that can influence mineral dust settling has to do with the electrical properties of dust particles. The dust particles are charged in the atmosphere either due to the attachment of atmospheric ions on them (Mallios et al. 2021b) or/and due to collisions, a process known as triboelectric effect (Ette, 1971, Eden and Vonnegut, 1973, Mills, 1977, Jayaratne, 1991). Moreover, there is a large-scale atmospheric electric field, due to the potential difference between the lower part of the Ionosphere and the Earth's surface (Rycroft et al., 2008). The electric field is modified by ion attachment process (Mallios et al. 2021b) or by the charge separation caused by updrafts (Krauss et al., 2003). Therefore, electrical forces are generated that might influence the particle settling process by balancing the gravity or changing the particle orientation. The quantification of the particles electrical properties is still an open question.

Triboelectric effect is able to modify the particles saltation process at the emission sources right above the ground due to the generation of very high values of electric charge caused by the large collision frequency which is a consequence of the wind and the large particle number density (Kok and Renno, 2006, 2008). As the particles are aloft, the collision frequency decreases (Rahman et al., 2008) and the ion attachment process can modify the acquired particle charge, because the electric field of the charged particles tend to attract ions of opposite polarities (Mallios et al., 2021b). It is still unknown if the acquired charge of the particles remains or is neutralized. Toth III et al., (2020) estimated that if the particle net charge persists, then the ambient electric field is sufficient to generate electrical forces that can keep particles suspended at higher elevations and enrich the concentration of larger particles at higher elevations. Mallios et al. (2021) calculated the ion-attachment rates of settling spherical particles in the radius range of 1-100 μm, and found that the maximum electric force that acts upon the particles is two orders of magnitude smaller than the gravity force, and doesn’t significantly influence the particle dynamics. They concluded that a generalized model that includes all the particle charging mechanisms is necessary for the proper study of the dust particle electric properties influence on the settling process.

According to aforementioned studies, the particle ashericity seems to be a strong candidate for the suggested corrections in this work. Vertically oriented prolate spheroids with aspect ratio 2.4 can "experience" a 52% velocity reduction compared to their spherical counterparts of the same maximum size. This difference can increase in the case of tri-axial ellipsoidal particles (Huang et al., 2020), or in the case of more aspherical particles. As the electric field and the particle electrical charge are responsible for the particle vertical orientation, the proper quantification of the particle electrical properties and their incorporation into the WRF-L model constitute the future steps of this work.

~~Finally, it is worth mentioning that a possible source of error in the gravitational loses simulated by the model, are the numerical errors, such as the numerical diffusion in the advection equation of gravitational settling, since WRF-GOCART-AFWA (and the WRF-L) uses a first-order upwind scheme. In any case, the proposed scheme presented here, provides a tool for the investigation of the physical processes in the transport of coarse and giant particles, along with their impacts on other physical processes in the atmosphere, such as ice nucleation and radiation interactions. The artificial reduction in the settling velocity is not attributed to a known physical mechanism (although results from the past literature reveal some candidates that can give results on the same order of magnitude). Thus, despite the encouraging results, more research is needed towards understanding the physical or numerical processes driving this finding, including the estimation of the impact of non-spherical particles, electricity, the radiation impact on thermodynamics and the disturbance of the mass balance due to the numerical diffusion.~~

5 Summary and conclusions

In the current state-of-the-art atmospheric dust models, several physical processes governing dust life cycle components are not well represented or they are not included in the relevant parameterization schemes. This drawback, along with the lack of knowledge on the underlying mechanisms, results in the failure of the numerical simulations to reproduce adequately the long-range transport of super-coarse and giant mineral particles, as it has been justified via their evaluation versus sophisticated dust observations. Among the model limitations, well documented in literature, one of the critical is the neglect of mineral particles with diameters larger than 20 μm, under the erroneous assumption that they deposit quickly after their emission.

In the current study, we modify the transport particle size distribution in WRF, expanding at size ranges up to 100 μm in diameter, by constraining the shape of the modelled PSD with the observed one above dust sources, acquired in the framework of the FENNEC 2011 campaign. A novelty of our work constitutes the upgrade of the drag coefficient, determining the settling velocity of dust particles, for accounting realistic dust particles sizes ($Re < 10^5$), opposite to what is assumed in the traditional Stokes' theory. After optimally tuning the CONTROL run, we performed a series of sensitivity experiments in which the settling velocity has been reduced, aiming to artificially resemble the real forces acting on particles moving vertically and counteract gravitational settling. Our period of interest spans from 5th to 25th August 2015, when the AER-D campaign took place in the surrounding area of Cape Verde, residing in the core of the "corridor" of the Saharan dust transport along the Tropical Atlantic Ocean. In our experiments, the simulation domain covers most of the Sahara Desert (encompassing the most active dust sources worldwide) and the eastern sector of the Tropical Atlantic Ocean (receiving large amounts of mineral particles from the nearby Saharan dust sources). The dust-related numerical outputs produced by the CONTROL and URx (referring to the reduction of the settling velocity by 20%, 40%, 60% and 80% and it is expressed by the term x) experiments are evaluated against the LIVAS satellite datasets providing pure dust extinction vertical profiles. Nevertheless, special attention is given on the evaluation of the WRF-L PSD against airborne in-situ measurements acquired in the framework of the AER-D campaign.

Μορφοποιησε: Εκθέτης

Μορφοποιησε: Εκθέτης

Μορφοποιησε: Εκθέτης

Based on our results, in the CONTROL experiment, the model tends to underestimate the dust volume concentration of coarse and giant dust particles (FENNEC) since the very early stage of dust transport, when the emitted mineral particles are uplifted at 1 km above the sources. Subsequently, the initially obtained model underestimation becomes more pronounced, against those measured in AER-D, particularly for the super-coarse (bin 4, diameters from 17 to 40 μm) and giant (bin 5, diameters from 40 to 100 μm) dust particles, in the vicinity of Cape Verde (i.e., downwind region). Our findings are in line with the already stated underestimation of the presence of coarse and giant dust particles' presence during their long range dust transport. Nevertheless, when we gradually reduce the settling velocity (URx runs) the model performance steadily improves. Overall, among the numerical experiments, the best match of the simulated and the observed PSDs is achieved for the UR80 scenario (i.e., reduction of the settling velocity by 80%), thus highlighting the misrepresentation or the absence of forces, within the model parameterization schemes, acting on dust particles and counteract gravitational settling. Through the case-by-case inspection, it is revealed that the UR60 and UR40 scenarios can also occasionally provide the optimum model-observations agreement thus highlighting the complexity of the real physical processes that regulate dust particles' settling velocity and suspension. From the evaluation of the vertically resolved simulated dust extinction against the corresponding measurements from the LIVAS dataset, it is revealed that for the UR40 run the model-observations are minimized (oscillating around zero) whereas the UR80 run outperforms in reproducing the vertical structure of the dust layers within the Saharan Air Layer. Summarizing, our work demonstrated an innovative approach in order to overcome existing drawbacks of the atmospheric-dust models towards improving the simulations of dust transport along the Tropical Atlantic Ocean. There are several candidate mechanisms, along with inappropriate definition and treatment of mineral particles in the parameterization schemes, hampering models in reproducing adequately the observed dust patterns. Despite our encouraging results, there are many mandatory steps towards upgrading the current state-of-the-art atmospheric dust models in anticipation of an optimum assessment of the multifaceted role of dust aerosols within the Earth-Atmosphere system.

Author Contributions: ED, VA, and AT design the study; SM guided ED on the methodology for the replacement of the drag coefficient. AT provided useful assistance on the treatment of airborne observations. CR provided the data from the airborne in situ measurements and provided useful information about the instrumentation methods. ED developed the code, performed the simulations and analyzed the results. AG and CR consulted ED on the methodology of in situ and WRF datasets. VA, EM and EP provided the LIVAS dataset, lead the collocation methodology and helped on the interpretation of the results. ED plotted the model and observation data (apart from LIVAS). EP treated and plotted LIVAS data; ED wrote the manuscript draft; VA, AT, AG, EP, SM, CS, SS, EM, CR, DB and PK provided critical feedback and reviewed and edited the manuscript."

~~Author Contributions: ED, VA, and AT design the study; ED developed the code and performed the simulations. ED, EP and AG analyzed and plot the data; ED wrote the manuscript draft; VA, AT, AG, EP, SM, CS, SS, EM, CR, DB and PK provided critical feedback and helped shape the research, analysis, and reviewed and edited the manuscript.~~

Μορφοποίησε: Αγγλικά (Ηνωμένου Βασιλείου)

Μορφοποιήθηκε: Εσοχή: Πρώτη γραμμή: 1,27 εκ.

Μορφοποίησε: Γραμματοσειρά: 10 στ., Όχι Πλάγια

Μορφοποίησε: Γραμματοσειρά: 10 στ., Όχι Πλάγια

Μορφοποίησε: Προεπιλεγμένη γραμματοσειρά

Funding: This research was supported by the project "PANhellenic infrastructure for Atmospheric Composition and climatE change" (no. MIS 5021516), which is implemented under the action "Reinforcement of the Research and Innovation Infrastructure", funded by the "Competitiveness, Entrepreneurship and Innovation" Operational Programme (NSRF 2014–2020) and co-financed by Greece and the European Union (European Regional Development Fund). Support was also provided ~~This research was supported~~ by D-TECT (Grant Agreement 725698) funded by the European Research Council (ERC). ED would like to acknowledge funding by Greece and the Stavros Niarhos Foundation (SNF). CLR was funded by NERC grant reference NE/M018288/1. EM was funded by the European Research Council 661 (grant no. 725698, D-TECT) and by a DLR VO-R young investigator group and the Deutscher Akademischer Austauschdienst (grant no. 57370121). AG acknowledges support by the Hellenic Foundation for Research and Innovation (H. F. R. I.) under the "2nd Call for H. F. R. I. Research Projects to support Post-Doctoral Researchers" (project acronym: ATLANTAS, project number: 544). ~~The MIDAS dataset has been developed in the framework of the DUST-GLASS project (grant no. 749461; European Union's Horizon 2020 Research and Innovation program under the Marie Sklodowska-Curie Actions.~~

Acknowledgements: This work was supported by computational time granted from the National Infrastructures for Research and Technology S.A. (GRNET S.A.) in the National HPC facili~~-~~ty - A~~R-~~IS - under project ID pa210502-TRAP-P. We thank the PANhellenic GEophysical observatory of Antikythera (PANGEA) for providing access to the LIVAS ~~and MIDAS~~ data used in this study and their computational center. The National Centers for Environmental Prediction (NCEP) is gratefully acknowledged for the provision of the Global Forecasting System (GFS) operational analyses and the real time global (RTG) sea surface temperature (SST) analyses. We would like to thank the NASA CALIPSO team and NASA/LaRC/ASDC for making the CALIPSO products available, which have been used to build the LIVAS products, and ESA, who funded the LIVAS project (contract no. 4000104106/11/NL/FF/fk).

Data Availability: The model outputs and the data used for the analysis are available upon request from Vassilis Amiridis (vamoir@noa.gr) and/or Eleni Drakaki (eldrakaki@noa.gr). The LIVAS dust ~~-~~products are available upon request from Vassilis Amiridis (vamoir@noa.gr), Emmanouil Proestakis (proestakis@noa.gr), and/or Eleni Marinou (elmarinou@noa.gr). ~~The MIDAS dataset has been developed in the framework of the DUST-GLASS project (grant no.749461; European Union's Horizon 2020 Research and Innovation programme under the Marie Sklodowska-Curie Actions) and it is available at: https://doi.org/10.5281/zenodo.4244106~~

Code Availability: The source code of WRF-L is available upon request from Vassilis Amiridis (vamoir@noa.gr) and/or Eleni Drakaki (eldrakaki@noa.gr).

Μορφοποίησε: Γραμματοσειρά: (Προεπιλεγμένη) Times New Roman, Χρώμα γραμματοσειράς: Αυτόματο, Αγγλικά (Ηνωμένων Πολιτειών), Μοτίβο: Διαφανές

Μορφοποίησε: Γραμματοσειρά: (Προεπιλεγμένη) Times New Roman, Χρώμα γραμματοσειράς: Αυτόματο, Αγγλικά (Ηνωμένων Πολιτειών), Μοτίβο: Διαφανές

Μορφοποίησε: Εκθέτης

References

Amiridis, V., Wandinger, U., Marinou, E., Giannakaki, E., Tsekeri, A., Basart, S., Kazadzis, S., Gkikas, A., Taylor, M., Baldasano, J. and Ansmann, A.: Optimizing CALIPSO Saharan dust retrievals, Atmos. Chem. Phys., 13(23), 12089–12106, doi:10.5194/acp-13-12089-2013, 2013.

Amiridis, V., Marinou, E., Tsekeri, A., Wandinger, U., Schwarz, A., Giannakaki, E., Mamouri, R., Kokkalis, P., Binietoglou, I., Solomos, S., Herekakis, T., Kazadzis, S., Gerasopoulos, E., Proestakis, E., Kottas, M., Balis, D., Papayannis, A., Kontoes, C., Kourtidis, K., Papagiannopoulos, N., Mona, L., Pappalardo, G., Le Rille, O. and Ansmann, A.: LIVAS: a 3-D multi-wavelength aerosol/cloud database based on CALIPSO and EARLINET, Atmos. Chem. Phys., 15(13), 7127–7153, doi:10.5194/acp-15-7127-2015, 2015.

Basart, S., Vendrell, L. and Baldasano, J. M.: High-resolution dust modelling over complex terrains in West Asia, Aeolian Res., 23, 37–50, doi:10.1016/j.aeolia.2016.09.005, 2016.

Bullard, J. E., Baddock, M., Bradwell, T., Crusius, J., Darlington, E., Gaiero, D., Gassó, S., Gisladottir, G., Hodgkins, R., McCulloch, R., McKenna-Neuman, C., Mockford, T., Stewart, H. and Thorsteinsson, T.: High-latitude dust in the Earth system, Rev. Geophys., 54(2), 447–485, doi:10.1002/2016RG000518, 2016.

Chimot, J., Pepijn Veefkind, J., Vlemmix, T., De Haan, J. F., Amiridis, V., Proestakis, E., Marinou, E. and Levelt, P. F.: An exploratory study on the aerosol height retrieval from OMI measurements of the 477 nmO2 O2 spectral band using a neural network approach, Atmos. Meas. Tech., 10(3), 783–809, doi:10.5194/amt-10-783-2017, 2017.

Cowie, S. M., Knippertz, P. and Marsham, J. H.: A climatology of dust emission events from Northern Africa using long-term surface observations, Atmos. Chem. Phys., 14(16), 8579–8597, doi:10.5194/acp-14-8579-2014, 2014.

Clift, R. and Gauvin, W. H.: Motion of entrained particles in gas streams, Can. J. Chem. Eng., 49(4), 439–448, doi:10.1002/cjce.5450490403, 1971.

Clift, R., Grace, J. R. and Weber, M. E.: Bubbles, Drops, and Particles, Dover Publications. [online] Available from: https://books.google.gr/books?id=UUrOmD8niUQC, 2005.

Danielson, J. J. and Gesch, D. B.: Global multi-resolution terrain elevation data 2010 (GMTED2010), Open-File Report, https://doi.org/10.3133/ofr20111073, 2011.

Daskalopoulou, V., Mallios, S. A., Ulanowski, Z., Hloupis, G., Gialitaki, A., Tsikoudi, I., Tassis, K. and Amiridis, V.: The electrical activity of Saharan dust as perceived from surface electric field observations, Atmos. Chem. Phys., 21(2), 927–949, doi:10.5194/acp-21-927-2021, 2021.

Davies, C. N.: Definitive equations for the fluid resistance of spheres, Proc. Phys. Soc., 57(4), 259–270, doi:10.1088/0959-5309/57/4/301, 1945.

Diehl, K., Debertshäuser, M., Eppers, O., Schmithüsen, H., Mitra, S. K. and Borrmann, S.: Particle surface area dependence of mineral dust in immersion freezing mode: Investigations with freely suspended drops in an acoustic levitator and a vertical wind tunnel, Atmos. Chem. Phys., 14(22), 12343–12355, doi:10.5194/acp-14-12343-2014, 2014.

van der Does, M., Knippertz, P., Zschenderlein, P., Giles Harrison, R. and Stuut, J. B. W.: The mysterious long-range transport of giant mineral dust particles, Sci. Adv., 4(12), eaau2768, doi:10.1126/sciadv.aau2768, 2018.

Du, Y., Xu, X., Chu, M., Guo, Y. and Wang, J.: Air particulate matter and cardiovascular disease: The epidemiological, biomedical and clinical evidence, J. Thorac. Dis., 8(1), E8–E19, doi:10.3978/j.issn.2072-1439.2015.11.37, 2016.

Dubovik, O., Holben, B. N., Lapyonok, T., Sinyuk, A., Mishchenko, M. I., Yang, P. and Slutsker, I.: Non-spherical aerosol retrieval method employing light scattering by spheroids, Geophys. Res. Lett., 29(10), 54-1-54–4, doi:10.1029/2001gl014506, 2002.

Eden, H. F. and Vonnegut, B.: Electrical Breakdown Caused by Dust Motion in Low-Pressure Atmospheres: Considerations for Mars, Science (80-.)., 180(4089), 962–963, doi:10.1126/science.180.4089.962, 1973.

Escribano, J., Tomaso, E. Di, Jorba, O., Klose, M., Ageitos, M. G., Macchia, F., Amiridis, V., Baars, H., Marinou, E., Proestakis, E., Urbanneck, C., Althausen, D., Bühl, J., Mamouri, R. and García-pando, C. P.: Assimilating spaceborne lidar dust extinction improves dust forecasts, , (June), 1–36, 2021.

Ette, A. I. I.: The effect of the Harmattan dust on atmospheric electric parameters, J. Atmos. Terr. Phys., 33(2), 295–300, doi:https://doi.org/10.1016/0021-9169(71)90208-X, 1971.

Garcia-Carreras, L., Parker, D. J., Marsham, J. H., Rosenberg, P. D., Brooks, I. M., Lock, A. P., Marenco, F., Mcquaid, J. B. and Hobby, M.: The turbulent structure and diurnal growth of the Saharan atmospheric boundary layer, J. Atmos. Sci., 72(2), 693–713, doi:10.1175/JAS-D-13-0384.1, 2015.

Gasteiger, J., Groß, S., Sauer, D., Haarig, M., Ansmann, A. and Weinzierl, B.: Particle settling and vertical mixing in the Saharan Air Layer as seen from an integrated model, lidar, and in situ perspective, Atmos. Chem. Phys., 17(1), 297–311, doi:10.5194/acp-17-297-2017, 2017.

Gelaro, R., McCarty, W., Suárez, M. J., Todling, R., Molod, A., Takacs, L., Randles, C. A., Darmenov, A., Bosilovich, M. G., Reichle, R., Wargan, K., Coy, L., Cullather, R., Draper, C., Akella, S., Buchard, V., Conaty, A., da Silva, A. M., Gu, W., Kim, G. K., Koster, R., Lucchesi, R., Merkova, D., Nielsen, J. E., Partyka, G., Pawson, S., Putman, W., Rienecker, M., Schubert, S. D., Sienkiewicz, M. and Zhao, B.: The modern-era retrospective analysis for research and applications, version 2 (MERRA-2), J. Clim., 30(14), 5419–5454, doi:10.1175/JCLI-D-16-0758.1, 2017.

Georgoulias, A. K., Alexandri, G., Kourtidis, K. A., Lelieveld, J. and Zanis, P.: Spatiotemporal variability and contribution of different aerosol types to the aerosol optical depth over the Eastern Mediterranean, , 13853–13884, doi:10.5194/acp-16-13853-2016, 2016.

Georgoulias, A. K., Tsikerdekis, A., Amiridis, V., Marinou, E., Benedetti, A., Zanis, P., Alexandri, G., Mona, L., Kourtidis, K. A. and Lelieveld, J.: A 3-D evaluation of the MACC reanalysis dust product over Europe, northern Africa and Middle East using CALIOP/CALIPSO dust satellite observations, Atmos. Chem. Phys., 18(12), 8601–8620, doi:10.5194/acp-18-8601-2018, 2018.

Georgoulias, A. K., Boersma, K. F., Van Vliet, J., Zhang, X., Van Der A, R., Zanis, P. and De Laat, J.: Detection of NO2 pollution plumes from individual ships with the TROPOMI/S5P satellite sensor, Environ. Res. Lett., 15(12), doi:10.1088/1748-9326/abc445, 2020.

Giannadaki, D., Pozzer, A. and Lelieveld, J.: Modeled global effects of airborne desert dust on air quality and premature mortality, Atmos. Chem. Phys., 14(2), 957–968, doi:10.5194/acp-14-957-2014, 2014.

Giles, D. M., Sinyuk, A., Sorokin, M. G., Schafer, J. S., Smirnov, A., Slutsker, I., Eck, T. F., Holben, B. N., Lewis, J. R., Campbell, J. R., Welton, E. J., Korkin, S. V. and Lyapustin, A. I.: Advancements in the Aerosol Robotic Network (AERONET) Version 3 database - Automated near-real-time quality control algorithm with improved cloud screening for Sun photometer aerosol optical depth (AOD) measurements, Atmos. Meas. Tech., 12(1), 169–209, doi:10.5194/amt-12-169-2019, 2019.

Gilliam, R. C. and Pleim, J. E.: Performance Assessment of New Land Surface and Planetary Boundary Layer Physics in the WRF-ARW, J Appl Meteorol Climatol, 49, 760–774, https://doi.org/10.1175/2009JAMC2126.1, 2010.

Ginoux, P.: Effects of nonsphericity on mineral dust modeling, J. Geophys. Res., 108(D2), doi:10.1029/2002jd002516, 2003.

Ginoux, P., Chin, M., Tegen, I., Goddard, T. and In-, G.: Sources and distributions of dust aerosols simulated with the GOCART model, J. Geophys. Res., 106, 20255–20273, 2001.

Ginoux, P., Prospero, J. M., Gill, T. E., Hsu, N. C. and Zhao, M.: Global-scale attribution of anthropogenic and natural dust sources and their emission rates based on MODIS Deep Blue aerosol products, Rev. Geophys., 50(3), 1–36, doi:10.1029/2012RG000388, 2012.

Gkikas, A., Proestakis, E., Amiridis, V., Kazadzis, S., Di Tomaso, E., Tsekeri, A., Marinou, E., Hatzianastassiou, N. and Pérez Garciá-Pando, C.: ModIs Dust AeroSol (MIDAS): A global fine-resolution dust optical depth data set, Atmos. Meas. Tech., 14(1), 309–334, doi:10.5194/amt-14-309-2021, 2021.

Gkikas, A., Proestakis, E., Amiridis, V., Kazadzis, S., Di Tomaso, E., Marinou, E., Hatzianastassiou, N., Kok, J. F. and García-Pando, C. P.: Quantification of the dust optical depth across spatiotemporal scales with the MIDAS global dataset (2003-2017), Atmos. Chem. Phys., 22(5), 3553–3578, doi:10.5194/acp-22-3553-2022, 2022.

Gliß, J., Mortier, A., Schulz, M., Andrews, E., Balkanski, Y., Bauer, S. E., Benedictow, A. M. K., Bian, H., Checa-Garcia, R., Chin, M., Ginoux, P., Griesfeller, J. J., Heckel, A., Kipling, Z., Kirkevåg, A., Kokkola, H., Laj, P., Le Sager, P., Tronstad Lund, M., Lund Myhre, C., Matsui, H., Myhre, G., Neubauer, D., Van Noije, T., North, P., Olivié, D. J. L., Rémy, S., Sogacheva, L., Takemura, T., Tsigaridis, K. and Tsyro, S. G.: AeroCom phase III multi-model evaluation of the aerosol life cycle and optical properties using ground- And space-based remote sensing as well as surface in situ observations, Atmos. Chem. Phys., 21(1), 87–128, doi:10.5194/acp-21-87-2021, 2021.

Goudie, A. S.: Desert dust and human health disorders, Environ. Int., 63, 101–113, doi:10.1016/j.envint.2013.10.011, 2014.

Goudie, A. S. and Middleton, N. J.: Desert Dust in the Global System., 2006.

Grell, G. A. and Dévényi, D.: A generalized approach to parameterizing convection combining ensemble and data assimilation techniques, Geophys Res Lett, 29, 10–13, https://doi.org/10.1029/2002GL015311, 2002.

Grell, G. A., Peckham, S. E., Schmitz, R., McKeen, S. A., Frost, G., Skamarock, W. C. and Eder, B.: Fully coupled "online" chemistry within the WRF model, Atmos. Environ., 39(37), 6957–6975, doi:10.1016/j.atmosenv.2005.04.027, 2005.

Gu, Z., He, Y., Zhang, Y., Su, J., Zhang, R., Yu, C. W. and Zhang, D.: An overview of triggering mechanisms and characteristics of local strong sandstorms in china and haboobs, Atmosphere (Basel)., 12(6), 1–17, doi:10.3390/atmos12060752, 2021.

Hansen, J. E. and Travis, L. D.: Light scattering in planetary atmospheres, Space Sci. Rev., 16(4), 527–610, doi:10.1007/BF00168069, 1974.

Harb, K., Butt, O., Abdul-jauwad, S. and Al-yami, A. M.: Systems Adaptation for Satellite Signal under Dust , Sand and Gaseous Attenuations, J. Wirel. Netw. Commun., 3(3), 39–49, doi:10.5923/j.jwnc.20130303.03, 2013.

Heinold, B., Tegen, I., Esselborn, M., Kandler, K., Knippertz, P., Müller, D., Schladitz, A., Tesche, M., Weinzierl, B., Ansmann, A., Althausen, D., Laurent, B., Massling, A., Müller, T., Petzold, A., Schepanski, K. and Wiedensohler, A.: Regional Saharan dust modelling during the SAMUM 2006 campaign, Tellus, Ser. B Chem. Phys. Meteorol., 61(1), 307–324, doi:10.1111/j.1600-0889.2008.00387.x, 2009.

Hilsenrath, J. and of Standards, U. S. N. B.: Tables of Thermal Properties of Gases: Comprising Tables of Thermodynamic and Transport Properties of Air, Argon, Carbon Dioxide, Carbon Monoxide, Hydrogen, Nitrogen, Oxygen, and Steam , U.S. Department of Commerce, National Bureau of Standards. [online] Available from: https://books.google.gr/books?id=LK8vaddchE4C, 1955.

Huang, Y., Kok, J. F., Kandler, K., Lindqvist, H., Nousiainen, T., Sakai, T., Adebiyi, A. and Jokinen, O.: Climate Models and Remote Sensing Retrievals Neglect Substantial Desert Dust Asphericity, Geophys. Res. Lett., 47(6), 1–11, doi:10.1029/2019GL086592, 2020.

Huneeus, N., Schulz, M., Balkanski, Y., Griesfeller, J., Prospero, J., Kinne, S., Bauer, S., Boucher, O., Chin, M., Dentener, F., Diehl, T., Easter, R., Fillmore, D., Ghan, S., Ginoux, P., Grini, A., Horowitz, L., Koch, D., Krol, M. C., Landing, W., Liu, X., Mahowald, N., Miller, R., Morcrette, J.-J., Myhre, G., Penner, J., Perlwitz, J., Stier, P., Takemura, T. and Zender, C. S.: Global dust model intercomparison in AeroCom phase I, Atmos. Chem. Phys., 11(15), 7781–7816, doi:10.5194/acp-11-7781-2011, 2011.

Jayaratne, E. R.: Charge separation during the impact of sand on ice and its relevance to theories of thunderstrom electrification, Atmos. Res., 26(5), 407–424, doi:https://doi.org/10.1016/0169-8095(91)90061-Z, 1991.

Jennings, S. G.: The mean free path in air, J. Aerosol Sci., 19(2), 159–166, doi:10.1016/0021-8502(88)90219-4, 1988.

Jickells, T. D., An, Z. S., Andersen, K. K., Baker, A. R., Bergametti, C., Brooks, N., Cao, J. J., Boyd, P. W., Duce, R. A., Hunter, K. A., Kawahata, H., Kubilay, N., LaRoche, J., Liss, P. S., Mahowald, N., Prospero, J. M., Ridgwell, A. J., Tegen, I. and Torres, R.: Global iron connections between desert dust, ocean biogeochemistry, and climate, Science (80-.)., 308(5718), 67–71, doi:10.1126/science.1105959, 2005.

Jickells, T., Boyd, P. and Hunter, K. A.: Biogeochemical Impacts of Dust on the Global Carbon Cycle, in Mineral Dust: A Key Player in the Earth System, edited by P. Knippertz and J.-B. W. Stuut, pp. 359–384, Springer Netherlands, Dordrecht., 2014.

Kandler, K., et al.: Size distribution, mass concentration, chemical and mineralogical composition and derived optical parameters of the boundary layer aerosol at Tinfou, Morocco, during SAMUM 2006, Tellus B, 61, 32–50, https://doi.org/10.1111/j.1600-0889.2008.00385.x, 2009.

Knippertz, P. and Stuut, J. B. W.: Mineral dust: A key player in the earth system, Miner. Dust A Key Play. Earth Syst., 1–509, doi:10.1007/978-94-017-8978-3, 2014.

Kok, J. F.: An improved parameterization of wind-blown sand flux on Mars that includes the effect of hysteresis, Geophys. Res. Lett., 37(12), doi:10.1029/2010GL043646, 2010.

Kok, J. F.: A scaling theory for the size distribution of emitted dust aerosols suggests climate models underestimate the size of the global dust cycle, Proc. Natl. Acad. Sci. U. S. A., 108(3), 1016–1021, doi:10.1073/pnas.1014798108, 2011.

Kok, J. F., Adebiyi, A. A., Albani, S., Balkanski, Y., Checa-Garcia, R., Chin, M., Colarco, P. R., Hamilton, D. S., Huang, Y., Ito, A., Klose, M., Leung, D. M., Li, L., Mahowald, N. M., Miller, R. L., Obiso, V., Pérez García-Pando, C., Rocha-Lima, A., Wan, J. S. and Whicker, C. A.: Improved representation of the global dust cycle using observational constraints on dust properties and abundance, Atmos. Chem. Phys., 21(10), 8127–8167, doi:10.5194/acp-21-8127-2021, 2021.

Konsta, D., Binietoglou, I., Gkikas, A., Solomos, S., Marinou, E., Proestakis, E., Basart, S., García-Pando, C. P., El-Askary, H. and Amiridis, V.: Evaluation of the BSC-DREAM8b regional dust model using the 3D LIVAS-CALIPSO product, Atmos. Environ., 195, 46–62, doi:10.1016/j.atmosenv.2018.09.047, 2018.

Kosmopoulos, P. G., Kazadzis, S., El-Askary, H., Taylor, M., Gkikas, A., Proestakis, E., Kontoes, C. and El-Khayat, M. M.: Earth-observation-based estimation and forecasting of particulate matter impact on solar energy in Egypt, Remote Sens., 10(12), 1–23, doi:10.3390/rs10121870, 2018.

Krauss, C. E., Horányi, M. and Robertson, S.: Experimental evidence for electrostatic discharging of dust near the surface of Mars, New J. Phys., 5, doi:10.1088/1367-2630/5/1/370, 2003.

LeGrand, S. L., Polashenski, C., Letcher, T. W., Creighton, G. A., Peckham, S. E. and Cetola, J. D.: The AFWA dust emission scheme for the GOCART aerosol model in WRF-Chem v3.8.1, Geosci. Model Dev., 12(1), 131–166, doi:10.5194/gmd-12-131-2019, 2019.

Li, J. and Osada, K.: Preferential settling of elongated mineral dust particles in the atmosphere, , 34, 17807, doi:10.1029/2007GL030262, 2007.

Liu, D., Taylor, J. W., Crosier, J., Marsden, N., Bower, K. N., Lloyd, G., Ryder, C. L., Brooke, J. K., Cotton, R., Marenco, F., Blyth, A., Cui, Z., Estelles, V., Gallagher, M., Coe, H. and Choularton, T. W.: Aircraft and ground measurements of dust aerosols over the west African coast in summer 2015 during ICE-D and AER-D, Atmos. Chem. Phys., 18(5), 3817–3838, doi:10.5194/acp-18-3817-2018, 2018.

Loth, E.: Drag of non-spherical solid particles of regular and irregular shape, Powder Technol., 182(3), 342–353, doi:10.1016/j.powtec.2007.06.001, 2008.

Mahowald, N., Albani, S., Kok, J. F., Engelstaeder, S., Scanza, R., Ward, D. S. and Flanner, M. G.: The size distribution of desert dust aerosols and its impact on the Earth system, Aeolian Res., 15, 53–71, doi:10.1016/j.aeolia.2013.09.002, 2014.

Mallios, S. A., Drakaki, E. and Amiridis, V.: Effects of dust particle sphericity and orientation on their gravitational settling in the earth's atmosphere, J. Aerosol Sci., 150(April), 105634, doi:10.1016/j.jaerosci.2020.105634, 2020.

Mallios, S. A., Papangelis, G., Hloupis, G., Papaioannou, A., Daskalopoulou, V. and Amiridis, V.: Modeling of Spherical Dust Particle Charging due to Ion Attachment, Front. Earth Sci., 9(August), 1–22, doi:10.3389/feart.2021.709890, 2021a.

Mallios, S. A., Daskalopoulou, V. and Amiridis, V.: Orientation of non spherical prolate dust particles moving vertically in the Earth's atmosphere, J. Aerosol Sci., 151(November 2019), 105657, doi:10.1016/j.jaerosci.2020.105657, 2021b.

Mallios, S. A., Daskalopoulou, V. and Amiridis, V.: Modeling of the electrical interaction between desert dust particles and the Earth's atmosphere, J. Aerosol Sci., 165, 106044, doi:https://doi.org/10.1016/j.jaerosci.2022.106044, 2022.

Maring, H.: Mineral dust aerosol size distribution change during atmospheric transport, J. Geophys. Res., 108(D19), 8592, doi:10.1029/2002JD002536, 2003.

Marinou, E., Amiridis, V., Binietoglou, I., Tsikerdekis, A., Solomos, S., Proestakis, E., Konsta, Di., Papagiannopoulos, N., Tsekeri, A., Vlastou, G., Zanis, P., Balis, Di., Wandinger, U. and Ansmann, A.: Three-dimensional evolution of Saharan dust transport towards Europe based on a 9-year EARLINET-optimized CALIPSO dataset, Atmos. Chem. Phys., 17(9), 5893–5919, doi:10.5194/acp-17-5893-2017, 2017.

Marinou, E., Tesche, M., Nenes, A., Ansmann, A., Schrod, J., Mamali, D., Tsekeri, A., Pikridas, M., Baars, H., Engelmann, R., Voudouri, K. A., Solomos, S., Sciare, J., Groß, S., Ewald, F. and Amiridis, V.: Retrieval of ice-nucleating particle concentrations from lidar observations and comparison with UAV in situ measurements, Atmos. Chem. Phys., 19(17), 11315–11342, doi:10.5194/acp-19-11315-2019, 2019.

Meng, J., Huang, Y., Leung, D. M., Li, L., Adebiyi, A. A., Ryder, C. L., Mahowald, N. M. and Kok, J. F.: Improved Parameterization for the Size Distribution of Emitted Dust Aerosols Reduces Model Underestimation of Super Coarse Dust, Geophys. Res. Lett., 49(8), e2021GL097287, doi:https://doi.org/10.1029/2021GL097287, 2022.

Mie, G.: Beiträge zur Optik trüber Medien, speziell kolloidaler Metallösungen, Ann. Phys., 330(3), 377–445, doi:https://doi.org/10.1002/andp.19083300302, 1908.

Mills, A. A.: Dust clouds and frictional generation of glow discharges on Mars, Nature, 268(5621), 614, doi:10.1038/268614a0, 1977.

Nakanishi, M. and Niino, H.: An improved Mellor-Yamada Level-3 model: Its numerical stability and application to a regional prediction of advection fog, Boundary Layer Meteorol, 119, 397–407, https://doi.org/10.1007/s10546-005-9030-8, 2006.

Nickovic, S., Cvetkovic, B., Petković, S., Amiridis, V., Pejanović, G., Solomos, S., Marinou, E. and Nikolic, J.: Cloud icing by mineral dust and impacts to aviation safety, Sci. Rep., 11(1), 6411, doi:10.1038/s41598-021-85566-y, 2021.

Nicoll, K. A., Harrison, R. G. and Ulanowski, Z.: Observations of Saharan dust layer electrification, Environ. Res. Lett., 6(1), 1–8, doi:10.1088/1748-9326/6/1/014001, 2011.

O'Sullivan, D., Marenco, F., Ryder, C., Pradhan, Y., Kipling, Z., Johnson, B., Benedetti, A., Brooks, M., McGill, M., Yorks, J. and Selmer, P.: Models transport Saharan dust too low in the atmosphere compared to observations, Atmos. Chem. Phys. Discuss., 1–47, doi:10.5194/acp-2020-57, 2020.

Okin, G. S., Mahowald, N., Chadwick, O. A. and Artaxo, P.: Impact of desert dust on the biogeochemistry of phosphorus in terrestrial ecosystems, Global Biogeochem. Cycles, 18(2), doi:10.1029/2003GB002145, 2004.

Pérez, C., Nickovic, S., Pejanovic, G., Baldasano, J. M. and Özsoy, E.: Interactive dust-radiation modeling: A step to improve weather forecasts, J. Geophys. Res., 111(D16), D16206, doi:10.1029/2005JD006717, 2006.

Petters, M. D. and Kreidenweis, S. M.: A single parameter representation of hygroscopic growth and cloud condensation nucleus activity-Part 3: Including surfactant partitioning, Atmos. Chem. Phys., 13(2), 1081–1091, doi:10.5194/acp-13-1081-2013, 2013.

Proestakis, E., Amiridis, V., Marinou, E., Georgoulias, A. K., Solomos, S., Kazadzis, S., Chimot, J., Che, H., Alexandri, G., Binietoglou, I., Daskalopoulou, V., Kourtidis, K. A., De Leeuw, G. and Van Der A, R. J.: Nine-year spatial and temporal evolution of desert dust aerosols over South and East Asia as revealed by CALIOP, Atmos. Chem. Phys., 18(2), 1337–1362, doi:10.5194/acp-18-1337-2018, 2018.

Prospero, J. M., Bonatti, E., Schubert, C. and Carlson, T. N.: Dust in the Caribbean atmosphere traced to an African dust storm, Earth Planet. Sci. Lett., 9(3), 287–293, doi:10.1016/0012-821X(70)90039-7, 1970.

Prospero, J. M., Ginoux, P., Torres, O., Nicholson, S. E. and Gill, T. E.: Environmental characterization of global sources of atmospheric soil dust identified with the Nimbus 7 Total Ozone Mapping Spectrometer (TOMS) absorbing aerosol product, Rev. Geophys., 40(1), 2-1-2–31, doi:10.1029/2000RG000095, 2002.

Renard, J. B., Dulac, F., Durand, P., Bourgeois, Q., Denjean, C., Vignelles, D., Couté, B., Jeannot, M., Verdier, N. and Mallet, M.: In situ measurements of desert dust particles above the western Mediterranean Sea with the balloon-borne Light Optical Aerosol Counter/sizer (LOAC) during the ChArMEx campaign of summer 2013, Atmos. Chem. Phys., 18(5), 3677–3699, doi:10.5194/acp-18-3677-2018, 2018.

Roberts, A. J., Marsham, J. H., Knippertz, P., Parker, D. J., Bart, M., Garcia-Carreras, L., Hobby, M., McQuaid, J. B., Rosenberg, P. D. and Walker, D.: New Saharan wind observations reveal substantial biases in analysed dust-generating winds, Atmos. Sci. Lett., 18(9), 366–372, doi:10.1002/asl.765, 2017.

Rycroft, M. J., Harrison, R. G., Nicoll, K. A. and Mareev, E. A.: An Overview of Earth's Global Electric Circuit and Atmospheric Conductivity, Space Sci. Rev., 137(1), 83–105, doi:10.1007/s11214-008-9368-6, 2008.

Ryder, C. L., Highwood, E. J., Lai, T. M., Sodemann, H. and Marsham, J. H.: Impact of atmospheric transport on the evolution of microphysical and optical properties of Saharan dust, Geophys. Res. Lett., 40(10), 2433–2438, doi:10.1002/grl.50482, 2013a.

Ryder, C. L., Highwood, E. J., Rosenberg, P. D., Trembath, J., Brooke, J. K., Bart, M., Dean, A., Crosier, J., Dorsey, J., Brindley, H., Banks, J., Marsham, J. H., McQuaid, J. B., Sodemann, H. and Washington, R.: Optical properties of Saharan dust aerosol and contribution from the coarse mode as measured during the Fennec 2011 aircraft campaign, Atmos. Chem. Phys., 13(1), 303–325, doi:10.5194/acp-13-303-2013, 2013b.

Ryder, C. L., Marenco, F., Brooke, J. K., Estelles, V., Cotton, R., Formenti, P., McQuaid, J. B., Price, H. C., Liu, D., Ausset, P., Rosenberg, P. D., Taylor, J. W., Choularton, T., Bower, K., Coe, H., Gallagher, M., Crosier, J., Lloyd, G., Highwood, E. J. and Murray, B. J.: Coarse-mode mineral dust size distributions, composition and optical properties from AER-D aircraft

measurements over the tropical eastern Atlantic, Atmos. Chem. Phys., 18(23), 17225–17257, doi:10.5194/acp-18-17225-2018, 2018.

Ryder, C. L., Highwood, E. J., Walser, A., Seibert, P., Philipp, A. and Weinzierl, B.: Coarse and giant particles are ubiquitous in Saharan dust export regions and are radiatively significant over the Sahara, Atmos. Chem. Phys., 19(24), 15353–15376, doi:10.5194/acp-19-15353-2019, 2019.

Sanjeevi, S. K. P., Kuipers, J. A. M. and Padding, J. T.: Drag, lift and torque correlations for non-spherical particles from Stokes limit to high Reynolds numbers, Int. J. Multiph. Flow, 106, 325–337, doi:10.1016/j.ijmultiphaseflow.2018.05.011, 2018.

Shao, B., Liu, G. R., Lin, T., Xu, G. X. and Yan, X.: Rotation and orientation of irregular particles in viscous fluids using the gradient smoothed method (GSM), Eng. Appl. Comput. Fluid Mech., 11(1), 557–575, doi:10.1080/19942060.2017.1329169, 2017.

Sinyuk, A., Holben, B. N., Eck, T. F., Giles, D. M., Slutsker, I., Korkin, S., Schafer, J. S., Smirnov, A., Sorokin, M. and Lyapustin, A.: The AERONET Version 3 aerosol retrieval algorithm, associated uncertainties and comparisons to Version 2, Atmos. Meas. Tech., 13(6), 3375–3411, doi:10.5194/amt-13-3375-2020, 2020.

Solomos, S., Kallos, G., Kushta, J., Astitha, M., Tremback, C., Nenes, A. and Levin, Z.: An integrated modeling study on the effects of mineral dust and sea salt particles on clouds and precipitation, Atmos. Chem. Phys., 11(2), 873–892, doi:10.5194/acp-11-873-2011, 2011.

Solomos, S., Ansmann, A., Mamouri, R. E., Binietoglou, I., Patlakas, P., Marinou, E. and Amiridis, V.: Remote sensing and modelling analysis of the extreme dust storm hitting the Middle East and eastern Mediterranean in September 2015, Atmos. Chem. Phys., 17(6), 4063–4079, doi:10.5194/acp-17-4063-2017, 2017.

Solomos, S., Kalivitis, N., Mihalopoulos, N., Amiridis, V., Kouvarakis, G., Gkikas, A., Binietoglou, I., Tsekeri, A., Kazadzis, S., Kottas, M., Pradhan, Y., Proestakis, E., Nastos, P. T. and Marenco, F.: From tropospheric folding to Khamsin and Foehn winds: How atmospheric dynamics advanced a record-breaking dust episode in Crete, Atmosphere (Basel)., 9(7), doi:10.3390/atmos9070240, 2018.

Stockdale, A., Krom, M. D., Mortimer, R. J. G., Benning, L. G., Carslaw, K. S., Herbert, R. J., Shi, Z., Myriokefalitakis, S., Kanakidou, M. and Nenes, A.: Understanding the nature of atmospheric acid processing of mineral dusts in supplying bioavailable phosphorus to the oceans, Proc. Natl. Acad. Sci. U. S. A., 113(51), 14639–14644, doi:10.1073/pnas.1608136113, 2016.

Tagliabue, A., Bowie, A. R., Boyd, P. W., Buck, K. N., Johnson, K. S. and Saito, M. A.: The integral role of iron in ocean biogeochemistry, Nature, 543(7643), 51–59, doi:10.1038/nature21058, 2017.

Tesche, M., Ansmann, A., Müller, D., Althausen, D., Mattis, I., Heese, B., Freudenthaler, V., Wiegner, M., Esselborn, M., Pisani, G. and Knippertz, P.: Vertical profiling of Saharan dust with Raman lidars and airborne HSRL in southern Morocco during SAMUM, Tellus, Ser. B Chem. Phys. Meteorol., 61(1), 144–164, doi:10.1111/j.1600-0889.2008.00390.x, 2009.

Textor, C., Schulz, M., Guibert, S., Kinne, S., Balkanski, Y., Bauer, S., Berntsen, T., Berglen, T., Boucher, O., Chin, M., Dentener, F., Diehl, T., Easter, R., Feichter, H., Fillmore, D., Ghan, S., Ginoux, P., Gong, S., Grini, A., Hendricks, J., Horowitz, L., Huang, P., Isaksen, I., Iversen, T., Kloster, S., Koch, D., Kirkevåg, A., Kristjansson, J. E., Krol, M., Lauer, A., Lamarque, J. F., Liu, X., Montanaro, V., Myhre, G., Penner, J., Pitari, G., Reddy, S., Seland, Stier, P., Takemura, T. and Tie, X.: Analysis and quantification of the diversities of aerosol life cycles within AeroCom, Atmos. Chem. Phys., 6(7), 1777–1813, doi:10.5194/acp-6-1777-2006, 2006.

Toth III, J., Rajupet, S., Squire, H., Volbers, B., Zhou, J., Xie, L., Sankaran, R. M. and Lacks, D.: Electrostatic forces alter particle size distributions in atmospheric dust, Atmos. Chem. Phys. Discuss., 1–14, doi:10.5194/acp-2019-650, 2019.

Tsekeri, A., Amiridis, V., Tsichla, M., Fountoulakis, I., Nersesian, A., Proestakis, E., Gkikas, A., Papachristopoulou, K., Barlakas, V., and Kazadzis, S.:The effect of large dust size on solar radiation fluxes, International Radiation Symposium, Thessaloniki, Greece, 4-8 July 2022.

Tsikerdekis, A., Zanis, P., Steiner, A. L., Solmon, F., Amiridis, V., Marinou, E., Katragkou, E., Karacostas, T. and Foret, G.: Impact of dust size parameterizations on aerosol burden and radiative forcing in RegCM4, Atmos. Chem. Phys., 17(2), 769–791, doi:10.5194/acp-17-769-2017, 2017.

Twohy, C. H., Kreidenweis, S. M., Eidhammer, T., Browell, E. V., Heymsfield, A. J., Bansemer, A. R., Anderson, B. E., Chen, G., Ismail, S., DeMott, P. J. and Van Den Heever, S. C.: Saharan dust particles nucleate droplets in eastern Atlantic clouds, Geophys. Res. Lett., 36(1), 1–6, doi:10.1029/2008GL035846, 2009.

U.S. Standard Atmosphere, 1962, U.S. Government Printing Office, Washington, D.C., 1962,https://www.ngdc.noaa.gov/stp/space-weather/online-publications/miscellaneous/us-standard-atmosphere-1976/us-standard-atmosphere_st76-1562_noaa.pdf

Versteeg H. K. & Malalasekera W. (2007).An introduction to computational fluid dynamics : the finite volume method (2nd ed.). Pearson Education.

Weinzierl, B., Petzold, A., Esselborn, M., Wirth, M., Rasp, K., Kandler, K., SchüTZ, L., Koepke, P. and Fiebig, M.: Airborne measurements of dust layer properties, particle size distribution and mixing state of Saharan dust during SAMUM 2006, Tellus B Chem. Phys. Meteorol., 61(1), 96–117, doi:10.1111/j.1600-0889.2008.00392.x, 2009.

Weinzierl, B., Sauer, D., Esselborn, M., Petzold, A., Veira, A., Rose, M., Mund, S., Wirth, M., Ansmann, A., Tesche, M., Gross, S. and Freudenthaler, V.: Microphysical and optical properties of dust and tropical biomass burning aerosol layers in

the Cape Verde region-an overview of the airborne in situ and lidar measurements during SAMUM-2, Tellus, Ser. B Chem. Phys. Meteorol., 63(4), 589–618, doi:10.1111/j.1600-0889.2011.00566.x, 2011.

Weinzierl, B., Sauer, D., Minikin, A., Reitebuch, O., Dahlkötter, F., Mayer, B., Emde, C., Tegen, I., Gasteiger, J., Petzold, A., Veira, A., Kueppers, U. and Schumann, U.: On the visibility of airborne volcanic ash and mineral dust from the pilot's perspective in flight, Phys. Chem. Earth, 45–46, 87–102, doi:10.1016/j.pce.2012.04.003, 2012.

Weinzierl, B., Ansmann, A., Prospero, J. M., Althausen, D., Benker, N., Chouza, F., Dollner, M., Farrell, D., Fomba, W. K., Freudenthaler, V., Gasteiger, J., Groß, S., Haarig, M., Heinold, B., Kandler, K., Kristensen, T. B., Mayol-Bracero, O. L., Müller, T., Reitebuch, O., Sauer, D., Schäfler, A., Schepanski, K., Spanu, A., Tegen, I., Toledano, C. and Walser, A.: The Saharan aerosol long-range transport and aerosol-cloud-interaction experiment: Overview and selected highlights, Bull. Am. Meteorol. Soc., 98(7), 1427–1451, doi:10.1175/BAMS-D-15-00142.1, 2017.

Winker, D. M., Vaughan, M. A., Omar, A., Hu, Y., Powell, K. A., Liu, Z., Hunt, W. H. and Young, S. A.: Overview of the CALIPSO Mission and CALIOP Data Processing Algorithms, J. Atmos. Ocean. Technol., 26(11), 2310–2323, doi:10.1175/2009JTECHA1281.1, 2009.

Zastawny, M., Mallouppas, G., Zhao, F. and van Wachem, B.: Derivation of drag and lift force and torque coefficients for non-spherical particles in flows, Int. J. Multiph. Flow, 39, 227–239, doi:10.1016/j.ijmultiphaseflow.2011.09.004, 2012.

~~Amiridis, V., Wandinger, U., Marinou, E., Giannakaki, E., Tsekeri, A., Basart, S., Kazadzis, S., Gkikas, A., Taylor, M., Baldasano, J. and Ansmann, A.: Optimizing CALIPSO Saharan dust retrievals, Atmos. Chem. Phys., 13(23), 12089–12106, doi:10.5194/acp-13-12089-2013, 2013.~~

~~Amiridis, V., Marinou, E., Tsekeri, A., Wandinger, U., Schwarz, A., Giannakaki, E., Mamouri, R., Kokkalis, P., Binietoglou, I., Solomos, S., Herekakis, T., Kazadzis, S., Gerasopoulos, E., Proestakis, E., Kottas, M., Balis, D., Papayannis, A., Kontoes, C., Kourtidis, K., Papagiannopoulos, N., Mona, L., Pappalardo, G., Le Rille, O. and Ansmann, A.: LIVAS: a 3-D multi-wavelength aerosol/cloud database based on CALIPSO and EARLINET, Atmos. Chem. Phys., 15(13), 7127–7153, doi:10.5194/acp-15-7127-2015, 2015.~~

~~Bullard, J. E., Baddock, M., Bradwell, T., Crusius, J., Darlington, E., Gaiero, D., Gassó, S., Gisladottir, G., Hodgkins, R., McCulloch, R., McKenna-Neuman, C., Mockford, T., Stewart, H. and Thorsteinsson, T.: High-latitude dust in the Earth system, Rev. Geophys., 54(2), 447–485, doi:10.1002/2016RG000518, 2016.~~

~~Chen, F. and Dudhia, J.: Coupling an advanced land surface-hydrology model with the Penn State-NCAR MM5 modeling system. Part II: Preliminary model validation, Mon. Weather Rev., 129(4), 587–604, doi:10.1175/1520-0493(2001)129<0587:CAALSH>2.0.CO;2, 2001.~~

~~Clift, R. and Gauvin, W. H.: Motion of entrained particles in gas streams, Can. J. Chem. Eng., 49(4), 439–448, doi:10.1002/cjce.5450490403, 1971.~~

Μορφοποιήθηκε: Διάστημα Μετά: 6 στ., Έλεγχος "χήρας/ορφανής" γραμμής, Ρύθμιση διαστήματος μεταξύ κειμένου δυτικής γραφής και ασιατικού κειμένου, Ρύθμιση διαστήματος μεταξύ ασιατικού κειμένου και αριθμών

Danielson, J. J. and Gesch, D. B.: Global multi-resolution terrain elevation data 2010 (GMTED2010)., 2011.

Daskalopoulou, V., Mallios, S. A., Ulanowski, Z., Hloupis, G., Gialitaki, A., Tsikoudi, I., Tassis, K. and Amiridis, V.: The electrical activity of Saharan dust as perceived from surface electric field observations, Atmos. Chem. Phys., 21(2), 927–949, doi:10.5194/acp-21-927-2021, 2021.

Diehl, K., Debertshäuser, M., Eppers, O., Schmithüsen, H., Mitra, S. K. and Borrmann, S.: Particle surface area dependence of mineral dust in immersion freezing mode: Investigations with freely suspended drops in an acoustic levitator and a vertical wind tunnel, Atmos. Chem. Phys., 14(22), 12343–12355, doi:10.5194/acp-14-12343-2014, 2014.

van der Does, M., Knippertz, P., Zschenderlein, P., Giles Harrison, R. and Stuut, J. B. W.: The mysterious long-range transport of giant mineral dust particles, Sci. Adv., 4(12), eaau2768, doi:10.1126/sciadv.aau2768, 2018.

Du, Y., Xu, X., Chu, M., Guo, Y. and Wang, J.: Air particulate matter and cardiovascular disease: The epidemiological, biomedical and clinical evidence, J. Thorac. Dis., 8(1), E8–E19, doi:10.3978/j.issn.2072-1439.2015.11.37, 2016.

Gasteiger, J., Groß, S., Sauer, D., Haarig, M., Ansmann, A. and Weinzierl, B.: Particle settling and vertical mixing in the Saharan Air Layer as seen from an integrated model, lidar, and in situ perspective, Atmos. Chem. Phys., 17(1), 297–311, doi:10.5194/acp-17-297-2017, 2017.

Georgoulias, A. K., Tsikerdekis, A., Amiridis, V., Marinou, E., Benedetti, A., Zanis, P., Alexandri, G., Mona, L., Kourtidis, K. A. and Lelieveld, J.: A 3-D evaluation of the MACC reanalysis dust product over Europe, northern Africa and Middle East using CALIOP/CALIPSO dust satellite observations, Atmos. Chem. Phys., 18(12), 8601–8620, doi:10.5194/acp-18-8601-2018, 2018.

Giannadaki, D., Pozzer, A. and Lelieveld, J.: Modeled global effects of airborne desert dust on air quality and premature mortality, Atmos. Chem. Phys., 14(2), 957–968, doi:10.5194/acp-14-957-2014, 2014.

Gilliam, R. C. and Pleim, J. E.: Performance Assessment of New Land Surface and Planetary Boundary Layer Physics in the WRF-ARW, J. Appl. Meteorol. Climatol., 49(4), 760–774, doi:10.1175/2009JAMC2126.1, 2010.

Ginoux, P.: Effects of nonsphericity on mineral dust modeling, J. Geophys. Res. Atmos., 108(2), doi:10.1029/2002jd002516, 2003a.

Ginoux, P.: Effects of nonsphericity on mineral dust modeling, J. Geophys. Res., 108(D2), 4052, doi:10.1029/2002JD002516, 2003b.

Ginoux, P., Chin, M., Tegen, I., Goddard, T. and In , G.: Sources and distributions of dust aerosols simulated with the GOCART model, J. Geophys. Res., 106, 20255–20273, 2001.

Ginoux, P., Prospero, J. M., Gill, T. E., Hsu, N. C. and Zhao, M.: Global-scale attribution of anthropogenic and natural dust sources and their emission rates based on MODIS Deep Blue aerosol products, Rev. Geophys., 50(3), 1–36, doi:10.1029/2012RG000388, 2012.

Goudie, A. S.: Desert dust and human health disorders, Environ. Int., 63, 101–113, doi:10.1016/j.envint.2013.10.011, 2014.

Goudie, A. S. and Middleton, N. J.: Desert Dust in the Global System., 2006.

Grell, G. A. and Dévényi, D.: A generalized approach to parameterizing convection combining ensemble and data assimilation techniques, Geophys. Res. Lett., 29(14), 10–13, doi:10.1029/2002GL015311, 2002.

Grell, G. A., Peckham, S. E., Schmitz, R., McKeen, S. A., Frost, G., Skamarock, W. C. and Eder, B.: Fully coupled "online" chemistry within the WRF model, Atmos. Environ., 39(37), 6957–6975, doi:10.1016/j.atmosenv.2005.04.027, 2005.

Gu, Z., He, Y., Zhang, Y., Su, J., Zhang, R., Yu, C. W. and Zhang, D.: An overview of triggering mechanisms and characteristics of local strong sandstorms in china and haboobs, Atmosphere (Basel)., 12(6), 1–17, doi:10.3390/atmos12060752, 2021.

Harb, K., Butt, O., Abdul-jauwad, S. and Al-yami, A. M.: Systems Adaptation for Satellite Signal under Dust , Sand and Gaseous Attenuations, J. Wirel. Netw. Commun., 3(3), 39–49, doi:10.5923/j.jwnc.20130303.03, 2013.

Huang, Y., Kok, J. F., Kandler, K., Lindqvist, H., Nousiainen, T., Sakai, T., Adebiyi, A. and Jokinen, O.: Climate Models and Remote Sensing Retrievals Neglect Substantial Desert Dust Asphericity, Geophys. Res. Lett., 47(6), 1–11, doi:10.1029/2019GL086592, 2020.

Huneeus, N., Schulz, M., Balkanski, Y., Griesfeller, J., Prospero, J., Kinne, S., Bauer, S., Boucher, O., Chin, M., Dentener, F., Diehl, T., Easter, R., Fillmore, D., Ghan, S., Ginoux, P., Grini, A., Horowitz, L., Koch, D., Krol, M. C., Landing, W., Liu, X., Mahowald, N., Miller, R., Morcrette, J. J., Myhre, G., Penner, J., Perlwitz, J., Stier, P., Takemura, T. and Zender, C. S.: Global dust model intercomparison in AeroCom phase i, Atmos. Chem. Phys., 11(15), 7781–7816, doi:10.5194/acp-11-7781-2011, 2011.

Iacono, M. J., Delamere, J. S., Mlawer, E. J., Shephard, M. W., Clough, S. A. and Collins, W. D.: Radiative forcing by long-lived greenhouse gases: Calculations with the AER radiative transfer models, J. Geophys. Res. Atmos., 113(13), 2–9, doi:10.1029/2008JD009944, 2008.

Janić, Z. I.: Nonsingular implementation of the Mellor-Yamada level 2.5 scheme in the NCEP Meso model, edited by N. C. for E. P. (U.S.), [online] Available from: https://repository.library.noaa.gov/view/noaa/11409, 2001.

Jickells, T., Boyd, P. and Hunter, K. A.: Biogeochemical Impacts of Dust on the Global Carbon Cycle, in Mineral Dust: A Key Player in the Earth System, edited by P. Knippertz and J. B. W. Stuut, pp. 359–384, Springer Netherlands, Dordrecht., 2014.

Jickells, T. D., An, Z. S., Andersen, K. K., Baker, A. R., Bergametti, C., Brooks, N., Cao, J. J., Boyd, P. W., Duce, R. A., Hunter, K. A., Kawahata, H., Kubilay, N., LaRoche, J., Liss, P. S., Mahowald, N., Prospero, J. M., Ridgwell, A. J., Tegen, I. and Torres, R.: Global iron connections between desert dust, ocean biogeochemistry, and climate, Science (80-.)., 308(5718), 67–71, doi:10.1126/science.1105959, 2005.

Knippertz, P. and Stuut, J. B. W.: Mineral dust: A key player in the earth system, Miner. Dust A Key Play. Earth Syst., 1–509, doi:10.1007/978-94-017-8978-3, 2014.

Kok, J. F.: An improved parameterization of wind-blown sand flux on Mars that includes the effect of hysteresis, Geophys. Res. Lett., 37(12), doi:10.1029/2010GL043646, 2010.

Kok, J. F.: A scaling theory for the size distribution of emitted dust aerosols suggests climate models underestimate the size of the global dust cycle, Proc. Natl. Acad. Sci. U. S. A., 108(3), 1016–1021, doi:10.1073/pnas.1014798108, 2011.

Kok, J. F., Adebiyi, A. A., Albani, S., Balkanski, Y., Checa-Garcia, R., Chin, M., Colarco, P. R., Hamilton, D. S., Huang, Y., Ito, A., Klose, M., Li, L., Mahowald, N. M., Miller, R. L., Obiso, V., Pérez García-Pando, C., Rocha-Lima, A. and Wan, J. S.: Contribution of the world's main dust source regions to the global cycle of desert dust, Atmos. Chem. Phys., 21(10), 8169–8193, doi:10.5194/acp-21-8169-2021, 2021.

Konsta, D., Binietoglou, I., Gkikas, A., Solomos, S., Marinou, E., Proestakis, E., Basart, S., García-Pando, C. P., El-Askary, H. and Amiridis, V.: Evaluation of the BSC-DREAM8b regional dust model using the 3D-LIVAS-CALIPSO product, Atmos. Environ., 195, 46–62, doi:10.1016/j.atmosenv.2018.09.047, 2018.

Kosmopoulos, P. G., Kazadzis, S., El-Askary, H., Taylor, M., Gkikas, A., Proestakis, E., Kontoes, C. and El-Khayat, M. M.: Earth-observation-based estimation and forecasting of particulate matter impact on solar energy in Egypt, Remote Sens., 10(12), 1–23, doi:10.3390/rs10121870, 2018.

LeGrand, S. L., Polashenski, C., Letcher, T. W., Creighton, G. A., Peckham, S. E. and Cetola, J. D.: The AFWA dust emission scheme for the GOCART aerosol model in WRF-Chem v3.8.1, Geosci. Model Dev., 12(1), 131–166, doi:10.5194/gmd-12-131-2019, 2019.

Li, J. and Osada, K.: Preferential settling of elongated mineral dust particles in the atmosphere, Geophys. Res. Lett., 34(17), 2–5, doi:10.1029/2007GL030262, 2007.

Liu, D., Taylor, J. W., Crosier, J., Marsden, N., Bower, K. N., Lloyd, G., Ryder, C. L., Brooke, J. K., Cotton, R., Marenco, F., Blyth, A., Cui, Z., Estelles, V., Gallagher, M., Coe, H. and Choularton, T. W.: Aircraft and ground measurements of dust aerosols over the west African coast in summer 2015 during ICE-D and AER-D, Atmos. Chem. Phys., 18(5), 3817–3838, doi:10.5194/acp-18-3817-2018, 2018.

Mahowald, N., Albani, S., Kok, J. F., Engelstaeder, S., Scanza, R., Ward, D. S. and Flanner, M. G.: The size distribution of desert dust aerosols and its impact on the Earth system, Aeolian Res., 15, 53–71, doi:10.1016/j.aeolia.2013.09.002, 2014.

Mallios, S. A., Drakaki, E. and Amiridis, V.: Effects of dust particle sphericity and orientation on their gravitational settling in the earth's atmosphere, J. Aerosol Sci., 150(April), 105634, doi:10.1016/j.jaerosci.2020.105634, 2020.

Mallios, S. A., Papangelis, G., Hloupis, G., Papaioannou, A., Daskalopoulou, V. and Amiridis, V.: Modeling of Spherical Dust Particle Charging due to Ion Attachment, Front. Earth Sci., 9(August), 1–22, doi:10.3389/feart.2021.709890, 2021.

Maring, H., Savoie, D. L., Izaguirre, M. A., Custals, L. and Reid, J. S.: Mineral dust aerosol size distribution change during atmospheric transport, J. Geophys. Res. Atmos., 108(19), 1–6, doi:10.1029/2002jd002536, 2003.

Marinou, E., Amiridis, V., Binietoglou, I., Tsikerdekis, A., Solomos, S., Proestakis, E., Konsta, Di., Papagiannopoulos, N., Tsekeri, A., Vlastou, G., Zanis, P., Balis, Di., Wandinger, U. and Ansmann, A.: Three-dimensional evolution of Saharan dust transport towards Europe based on a 9-year EARLINET-optimized CALIPSO dataset, Atmos. Chem. Phys., 17(9), 5893–5919, doi:10.5194/acp-17-5893-2017, 2017.

Marinou, E., Tesche, M., Nenes, A., Ansmann, A., Schrod, J., Mamali, D., Tsekeri, A., Pikridas, M., Baars, H., Engelmann, R., Voudouri, K. A., Solomos, S., Sciare, J., Groß, S., Ewald, F. and Amiridis, V.: Retrieval of ice-nucleating particle concentrations from lidar observations and comparison with UAV in situ measurements, Atmos. Chem. Phys., 19(17), 11315–11342, doi:10.5194/acp-19-11315-2019, 2019.

Morrison, H., Curry, J. A. and Khvorostyanov, V. I.: A new double-moment microphysics parameterization for application in cloud and climate models. Part I: Description, J. Atmos. Sci., 62(6), 1665–1677, doi:10.1175/JAS3446.1, 2005.

Nakanishi, M. and Niino, H.: An improved Mellor-Yamada Level-3 model: Its numerical stability and application to a regional prediction of advection fog, Boundary-Layer Meteorol., 119(2), 397–407, doi:10.1007/s10546-005-9030-8, 2006.

Nicoll, K. A., Harrison, R. G. and Ulanowski, Z.: Observations of Saharan dust layer electrification, Environ. Res. Lett., 6(1), 1–8, doi:10.1088/1748-9326/6/1/014001, 2011.

O'Sullivan, D., Marenco, F., Ryder, C., Pradhan, Y., Kipling, Z., Johnson, B., Benedetti, A., Brooks, M., McGill, M., Yorks, J. and Selmer, P.: Models transport Saharan dust too low in the atmosphere compared to observations, Atmos. Chem. Phys. Discuss., 1–47, doi:10.5194/acp-2020-57, 2020.

Okin, G. S., Mahowald, N., Chadwick, O. A. and Artaxo, P.: Impact of desert dust on the biogeochemistry of phosphorus in terrestrial ecosystems, Global Biogeochem. Cycles, 18(2), doi:10.1029/2003GB002145, 2004.

Petters, M. D. and Kreidenweis, S. M.: A single parameter representation of hygroscopic growth and cloud condensation nucleus activity–Part 3: Including surfactant partitioning, Atmos. Chem. Phys., 13(2), 1081–1091, doi:10.5194/acp-13-1081-2013, 2013.

Proestakis, E., Amiridis, V., Marinou, E., Georgoulias, A. K., Solomos, S., Kazadzis, S., Chimot, J., Che, H., Alexandri, G., Binietoglou, I., Daskalopoulou, V., Kourtidis, K. A., De Leeuw, G. and Van Der A, R. J.: Nine-year spatial and temporal evolution of desert dust aerosols over South and East Asia as revealed by CALIOP, Atmos. Chem. Phys., 18(2), 1337–1362, doi:10.5194/acp-18-1337-2018, 2018.

Prospero, J. M., Bonatti, E., Schubert, C. and Carlson, T. N.: Dust in the Caribbean atmosphere traced to an African dust storm, Earth Planet. Sci. Lett., 9(3), 287–293, doi:10.1016/0012-821X(70)90039-7, 1970.

Prospero, J. M., Ginoux, P., Torres, O., Nicholson, S. E. and Gill, T. E.: Environmental characterization of global sources of atmospheric soil dust identified with the Nimbus 7 Total Ozone Mapping Spectrometer (TOMS) absorbing aerosol product, Rev. Geophys., 40(1), 2-1–2–31, doi:10.1029/2000RG000095, 2002.

Renard, J. B., Dulac, F., Durand, P., Bourgeois, Q., Denjean, C., Vignelles, D., Couté, B., Jeannot, M., Verdier, N. and Mallet, M.: In situ measurements of desert dust particles above the western Mediterranean Sea with the balloon-borne Light Optical Aerosol Counter/sizer (LOAC) during the ChArMEx campaign of summer 2013, Atmos. Chem. Phys., 18(5), 3677–3699, doi:10.5194/acp-18-3677-2018, 2018.

Ryder, C. L., Highwood, E. J., Rosenberg, P. D., Trembath, J., Brooke, J. K., Bart, M., Dean, A., Crosier, J., Dorsey, J., Brindley, H., Banks, J., Marsham, J. H., McQuaid, J. B., Sodemann, H. and Washington, R.: Optical properties of Saharan dust aerosol and contribution from the coarse mode as measured during the Fennec 2011 aircraft campaign, Atmos. Chem. Phys., 13(1), 303–325, doi:10.5194/acp-13-303-2013, 2013.

Ryder, C. L., Marenco, F., Brooke, J. K., Estelles, V., Cotton, R., Formenti, P., McQuaid, J. B., Price, H. C., Liu, D., Ausset, P., Rosenberg, P. D., Taylor, J. W., Choularton, T., Bower, K., Coe, H., Gallagher, M., Crosier, J., Lloyd, G., Highwood, E. J. and Murray, B. J.: Coarse-mode mineral dust size distributions, composition and optical properties from AER-D aircraft measurements over the tropical eastern Atlantic, Atmos. Chem. Phys., 18(23), 17225–17257, doi:10.5194/acp-18-17225-2018, 2018.

Ryder, C. L., Highwood, E. J., Walser, A., Seibert, P., Philipp, A. and Weinzierl, B.: Coarse and giant particles are ubiquitous in Saharan dust export regions and are radiatively significant over the Sahara, Atmos. Chem. Phys., 19(24), 15353–15376, doi:10.5194/acp-19-15353-2019, 2019a.

Ryder, C. L., Highwood, E. J., Walser, A., Seibert, P., Philipp, A. and Weinzierl, B.: Coarse and Giant Particles are Ubiquitous in Saharan Dust Export Regions and are Radiatively Significant over the Sahara, Atmos. Chem. Phys. Discuss., 1–36, doi:10.5194/acp-2019-421, 2019b.

Solomos, S., Kallos, G., Kushta, J., Astitha, M., Tremback, C., Nenes, A. and Levin, Z.: An integrated modeling study on the effects of mineral dust and sea salt particles on clouds and precipitation, Atmos. Chem. Phys., 11(2), 873–892, doi:10.5194/acp-11-873-2011, 2011.

Stockdale, A., Krom, M. D., Mortimer, R. J. G., Benning, L. G., Carslaw, K. S., Herbert, R. J., Shi, Z., Myriokefalitakis, S., Kanakidou, M. and Nenes, A.: Understanding the nature of atmospheric acid processing of mineral dusts in supplying bioavailable phosphorus to the oceans, Proc. Natl. Acad. Sci. U. S. A., 113(51), 14639–14644, doi:10.1073/pnas.1608136113, 2016.

Tagliabue, A., Bowie, A. R., Boyd, P. W., Buck, K. N., Johnson, K. S. and Saito, M. A.: The integral role of iron in ocean biogeochemistry, Nature, 543(7643), 51–59, doi:10.1038/nature21058, 2017.

Tesche, M., Ansmann, A., Müller, D., Althausen, D., Mattis, I., Heese, B., Freudenthaler, V., Wiegner, M., Esselborn, M., Pisani, G. and Knippertz, P.: Vertical profiling of Saharan dust with Raman lidars and airborne HSRL in southern Morocco during SAMUM, Tellus, Ser. B Chem. Phys. Meteorol., 61(1), 144–164, doi:10.1111/j.1600-0889.2008.00390.x, 2009.

Toth III, J., Rajupet, S., Squire, H., Volbers, B., Zhou, J., Xie, L., Sankaran, R. M. and Lacks, D.: Electrostatic forces alter particle size distributions in atmospheric dust, Atmos. Chem. Phys. Discuss., 1–14, doi:10.5194/acp-2019-650, 2019.

Twohy, C. H., Kreidenweis, S. M., Eidhammer, T., Browell, E. V., Heymsfield, A. J., Bansemer, A. R., Anderson, B. E., Chen, G., Ismail, S., DeMott, P. J. and Van Den Heever, S. C.: Saharan dust particles nucleate droplets in eastern Atlantic clouds, Geophys. Res. Lett., 36(1), 1–6, doi:10.1029/2008GL035846, 2009.

Weinzierl, B., Petzold, A., Esselborn, M., Wirth, M., Rasp, K., Kandler, K., Schütz, L., Koepke, P. and Fiebig, M.: Airborne measurements of dust layer properties, particle size distribution and mixing state of Saharan dust during SAMUM 2006, Tellus, Ser. B Chem. Phys. Meteorol., 61(1), 96–117, doi:10.1111/j.1600-0889.2008.00392.x, 2009.

Weinzierl, B., Sauer, D., Esselborn, M., Petzold, A., Veira, A., Rose, M., Mund, S., Wirth, M., Ansmann, A., Tesche, M., Gross, S. and Freudenthaler, V.: Microphysical and optical properties of dust and tropical biomass burning aerosol layers in the Cape Verde region-an overview of the airborne in situ and lidar measurements during SAMUM-2, Tellus, Ser. B Chem. Phys. Meteorol., 63(4), 589–618, doi:10.1111/j.1600-0889.2011.00566.x, 2011.

Weinzierl, B., Sauer, D., Minikin, A., Reitebuch, O., Dahlkötter, F., Mayer, B., Emde, C., Tegen, I., Gasteiger, J., Petzold, A., Veira, A., Kueppers, U. and Schumann, U.: On the visibility of airborne volcanic ash and mineral dust from the pilot's perspective in flight, Phys. Chem. Earth, 45–46, 87–102, doi:10.1016/j.pce.2012.04.003, 2012.

Weinzierl, B., Ansmann, A., Prospero, J. M., Althausen, D., Benker, N., Chouza, F., Dollner, M., Farrell, D., Fomba, W. K., Freudenthaler, V., Gasteiger, J., Groß, S., Haarig, M., Heinold, B., Kandler, K., Kristensen, T. B., Mayol-Bracero, O. L., Müller, T., Reitebuch, O., Sauer, D., Schäfler, A., Schepanski, K., Spanu, A., Tegen, I., Toledano, C. and Walser, A.: The Saharan aerosol long-range transport and aerosol-cloud-interaction experiment: Overview and selected highlights, Bull. Am. Meteorol. Soc., 98(7), 1427–1451, doi:10.1175/BAMS-D-15-00142.1, 2017a.

Weinzierl, B., Ansmann, A., Prospero, J. M., Althausen, D., Benker, N., Chouza, F., Dollner, M., Farrell, D., Fomba, W. K., Freudenthaler, V., Gasteiger, J., Groß, S., Haarig, M., Heinold, B., Kandler, K., Kristensen, T. B., Mayol-Bracero, O. L.,

Müller, T., Reitebuch, O., Sauer, D., Schäfler, A., Schepanski, K., Spanu, A., Tegen, I., Toledano, C. and Walser, A.: The Saharan aerosol long-range transport and aerosol-cloud-interaction experiment: Overview and selected highlights, Bull. Am. Meteorol. Soc., 98(7), 1427–1451, doi:10.1175/BAMS-D-15-00142.1, 2017b.

Winker, D. M., Vaughan, M. A., Omar, A., Hu, Y., Powell, K. A., Liu, Z., Hunt, W. H. and Young, S. A.: Overview of the CALIPSO Mission and CALIOP Data Processing Algorithms, J. Atmos. Ocean. Technol., 26(11), 2310–2323, doi:10.1175/2009JTECHA1281.1, 2009.

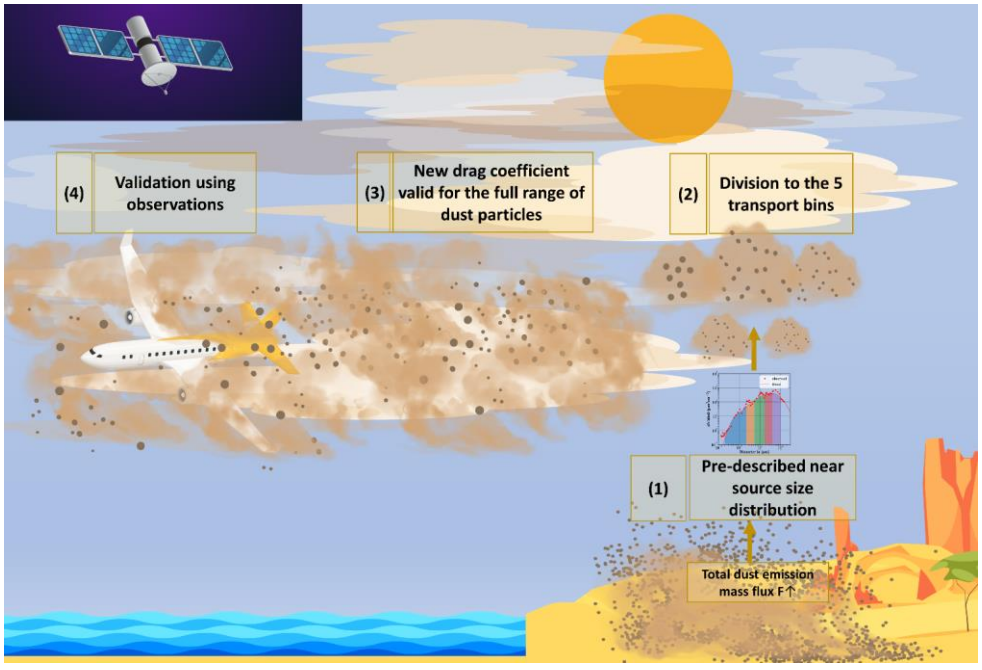

Figure 1: The structure of the presented work. Steps (1), (2) and (3) correspond to the appropriate modifications implemented in the WRF-Chem GOCART-AFWA dust scheme, for the inclusion of the giant dust particles and the development of WRF-L. Step (4) refers to model validation activities.

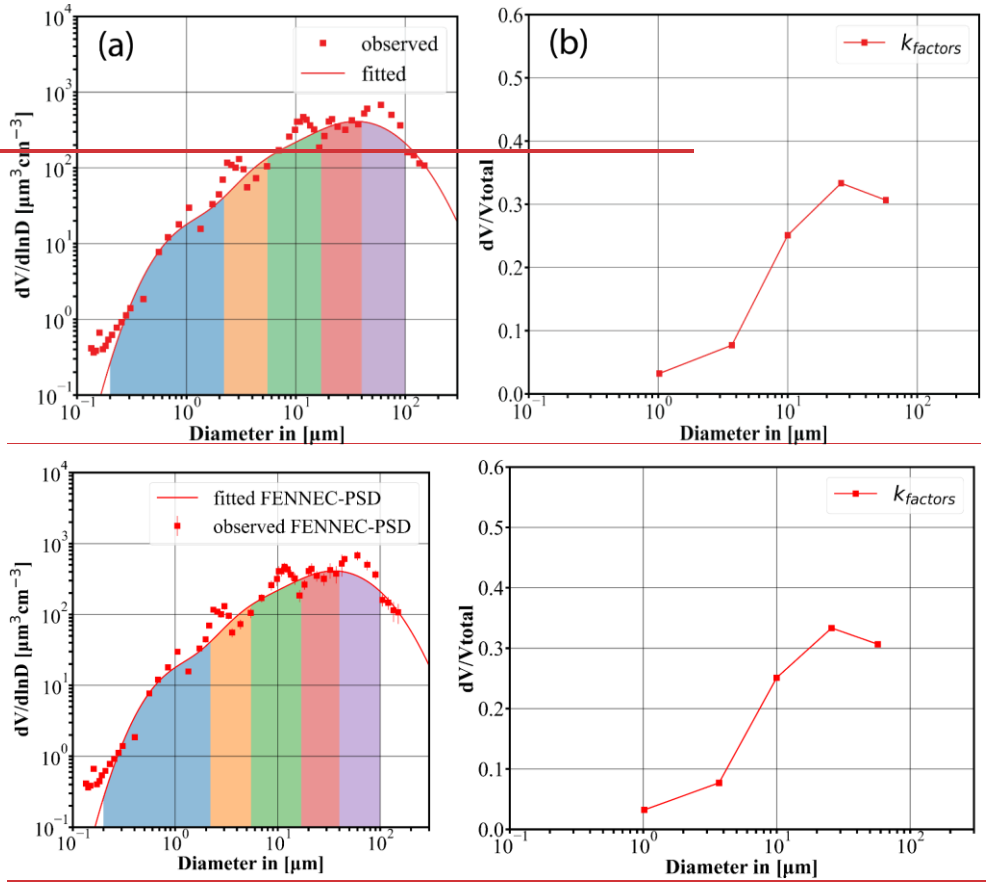

Figure 2: Prescribed dust size distribution used in the WRF-L for the distribution of total dust mass to the transport model size bins: (a) "observed FENNEC-PSD" ($\mu m^3 cm^{-3}$) (red squares), and the respective fitted volume PSD (black solid line). The observed FENNEC-PSD correspond to PSD measurements at 1km, obtained by averaging profile measured data of freshly uplifted dust cases, over 500m. The shaded areas indicate the model transport size bins in WRF-L. Error bars indicate the standard deviation (b) The $k_{factors}$ of the transport size bins calculated based on "fitted FENNEC-PSD", provide the mass fraction of the emitted dust for each bin.

Μορφοποίησε: Αγγλικά (Ηνωμένων Πολιτειών)

~~**Prescribed dust size distribution used in the WRF-L for the distribution of total dust mass to the transport model size bins: (a) observed FENNEC-PSD ($\mu m^3 cm^{-3}$) (red squares), and the respective fitted volume PSD (black solid line. The shaded areas indicate the model transport size bins in WRF-L. (b) The $k_{factors}$ of the transport size bins, providing the mass fraction of the emitted dust for each bin.**~~

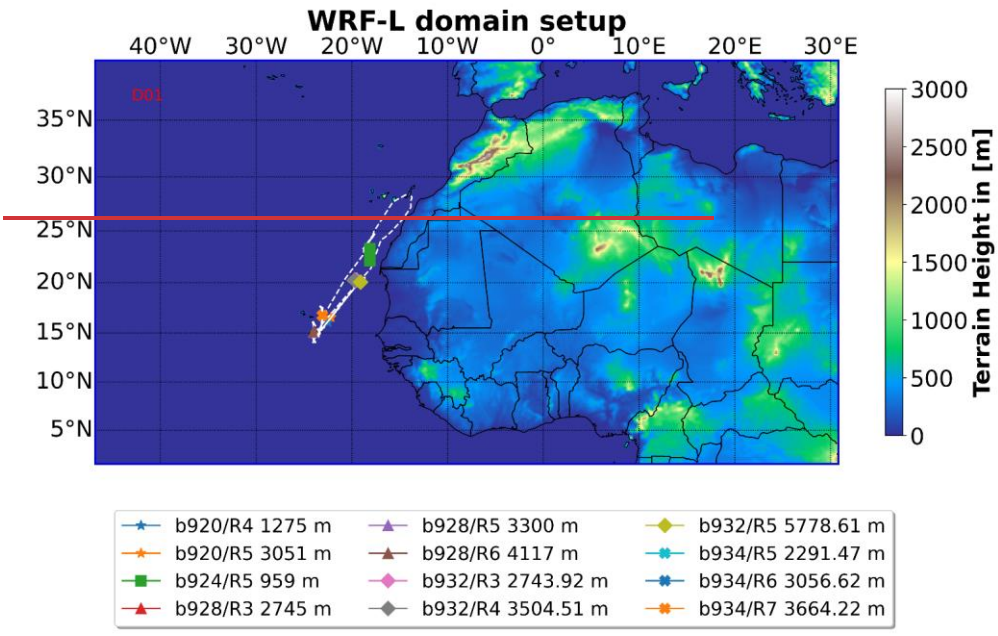
WRF-L domain setup
40°W
30°W
20°W
10°W
0°
10°E
20°E
30°E
D01
35°N
30°N
25°N
20°N
15°N
10°N
5°N
3000
2500
2000
1500
1000
500
0
Terrain Height in [m]
b920/R4 1275 m
b920/R5 3051 m
b924/R5 959 m
b928/R3 2745 m
b928/R5 3300 m
b928/R6 4117 m
b932/R3 2743.92 m
b932/R4 3504.51 m
b932/R5 5778.61 m
b934/R5 2291.47 m
b934/R6 3056.62 m
b934/R7 3664.22 m

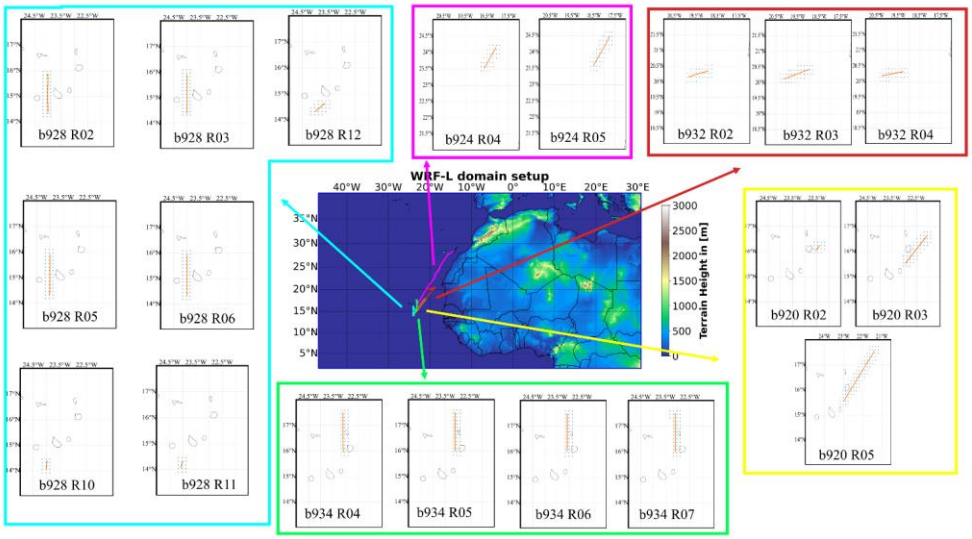

Figure 3: Domain and topography map of the WRF-L model simulations, with a horizontal grid spacing of 15km, and 70 vertical levels. The tracks of the AER-D flights, used in this study (b920, b924, b928, b932 and b934), are depicted in the central plot with different colours. The aircraft tracks of each flight RUN are also depicted with the orange dots in the surrounding maps. The blue dots correspond to the collocated model grid points.

~~**Figure 3: Domain map of the WRF-L model simulations, with horizontal grid spacing of 15km, and 70 vertical levels. The locations of the different runs for the AER-D flights b920, b924, b928, b932 and b932 are also depicted, along with the heights above the sea level (colored markers).**~~

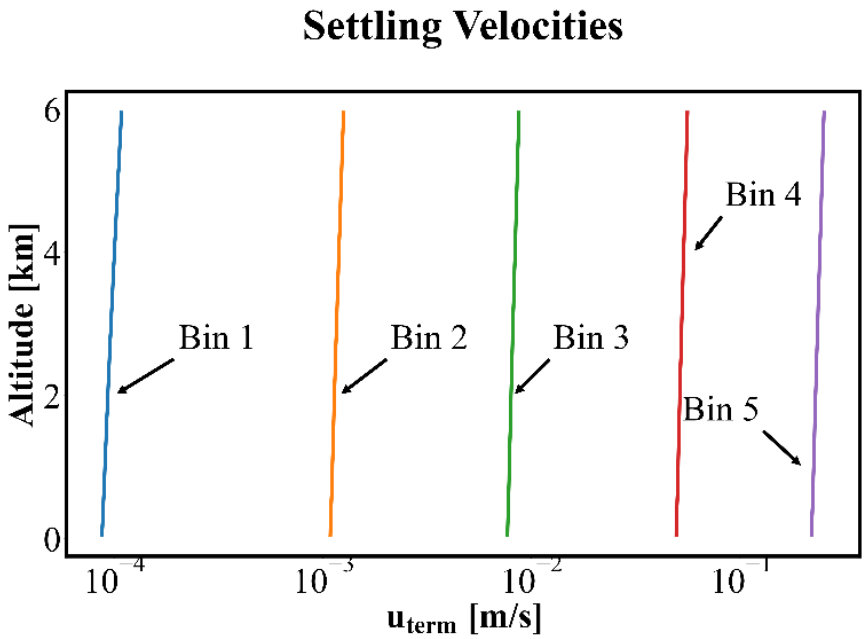

Figure 4: Terminal velocities of the CONTROL experiment, averaged for the simulation time and the domain. Each colored line corresponds to one of the new model size bins, with blue: Bin 1, orange: Bin 2, green: Bin 3, red: Bin 4 and purple: Bin 5.

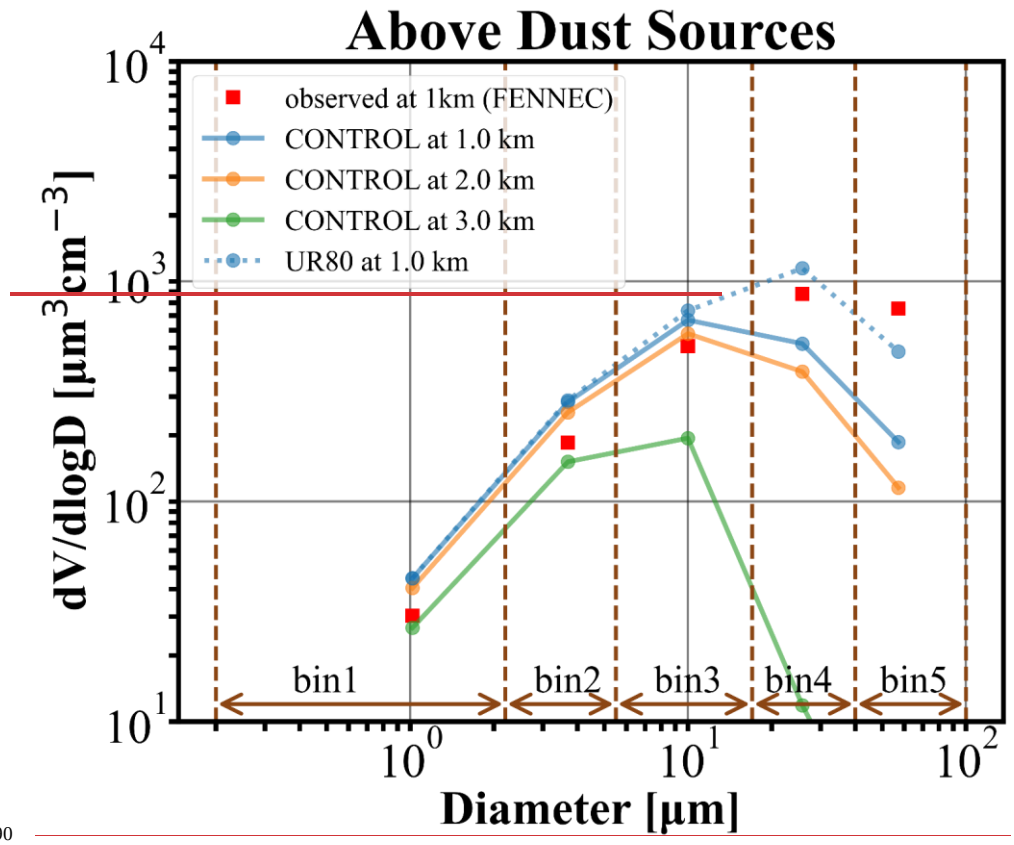
Above Dust Sources
observed at 1km (FENNEC)
CONTROL at 1.0 km
CONTROL at 2.0 km
CONTROL at 3.0 km
UR80 at 1.0 km
dV/dlogD [µm3cm−3]
Diameter [µm]
bin1
bin2
bin3
bin4
bin5

1490

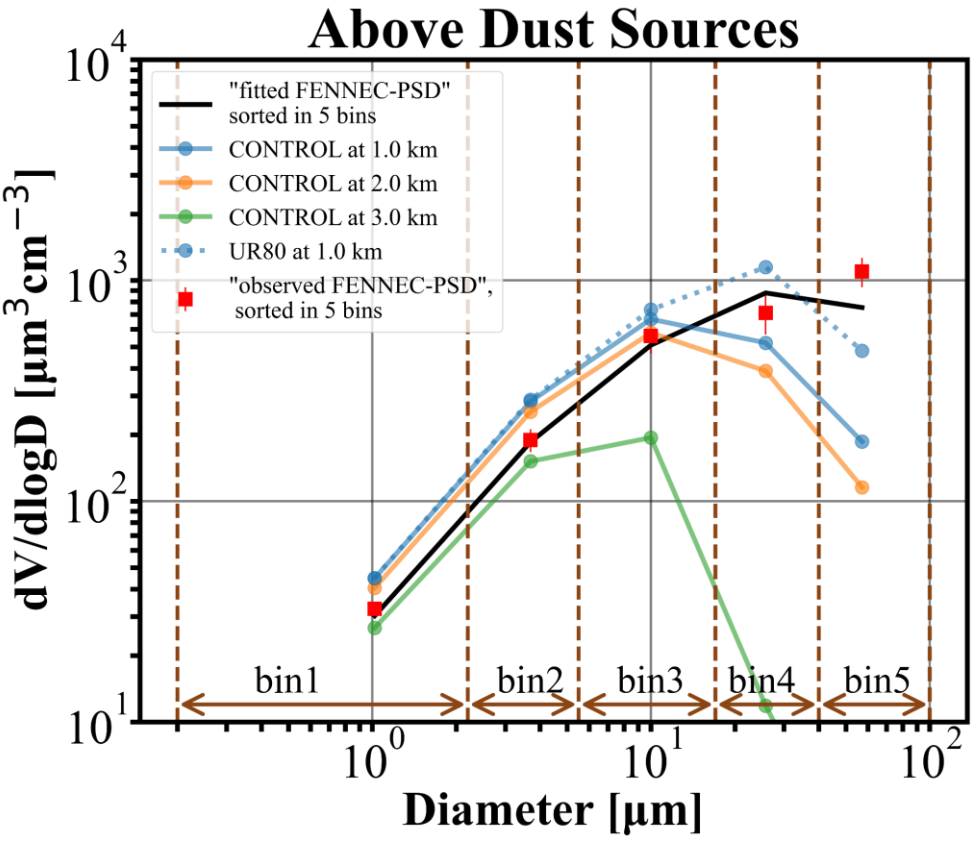

Figure 5: Dust size distribution above an emission model grid point (latitude=24.9º and longitude=9.2º) in Mali, on 11/08/2015 at 14UTC. Blue solid line: the dust PSD of the CONTROL run interpolated at 1 km altitude above the dust source, orange solid line: the dust PSD of the CONTROL run interpolated at 2 km altitude above dust source, green solid line: the dust PSD of the CONTROL run interpolated at 3 km altitude above dust source, blue dotted line: the dust PSD of the UR80 run interpolated at 1 km altitude above the dust source and red squares: the mean observed FENNEC-PSD at 1 km altitude, black squares the fitted FENNEC-PSD at 1km which has been used for the distribution of the model emission to the five size bins.

Μορφοποίησε: Γραμματοσειρά: Έντονα, Χρώμα γραμματοσειράς: Αυτόματο, Αγγλικά (Ηνωμένων Πολιτειών)

Μορφοποίησε: Γραμματοσειρά: Έντονα, Χρώμα γραμματοσειράς: Αυτόματο, Αγγλικά (Ηνωμένων Πολιτειών), Εκθέτης

Μορφοποίησε: Γραμματοσειρά: Έντονα, Χρώμα γραμματοσειράς: Αυτόματο, Αγγλικά (Ηνωμένων Πολιτειών)

Μορφοποίησε: Γραμματοσειρά: Έντονα, Χρώμα γραμματοσειράς: Αυτόματο, Αγγλικά (Ηνωμένων Πολιτειών), Εκθέτης

Μορφοποίησε: Γραμματοσειρά: Έντονα, Χρώμα γραμματοσειράς: Αυτόματο, Αγγλικά (Ηνωμένων Πολιτειών)

~~**Figure 5: Dust size distribution above an emission point. Blue line: the dust PSD of the CONTROL run at 1 km altitude above the dust source, orange line: the dust PSD of the CONTROL run at 2 km altitude above dust source, green line: the dust PSD of the CONTROL run at 3 km altitude above dust source, blue dotted line: the dust PSD of the UR80 run at 1 km altitude above the dust source and red squares: the mean observed FENNEC PSD at 1 km altitude.**~~

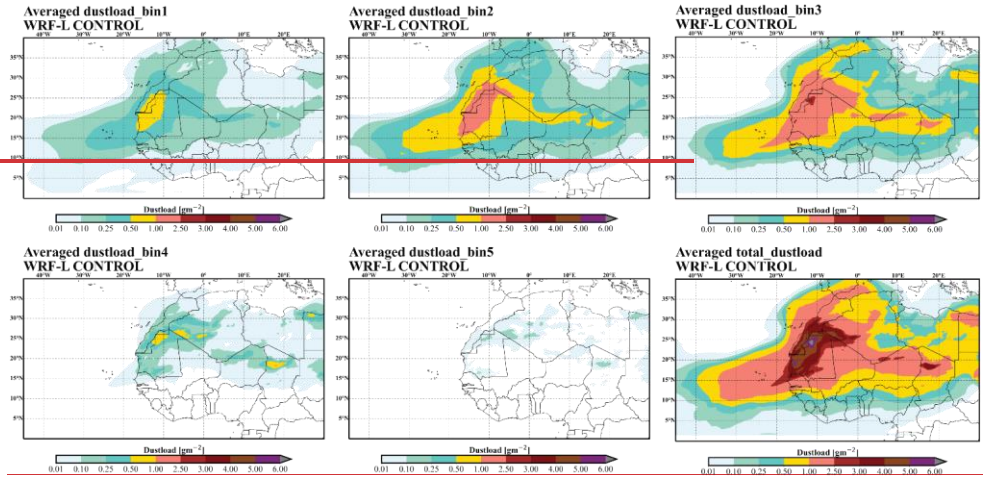
Averaged dustload_bin1
WRF-L CONTROL
Averaged dustload_bin2
WRF-L CONTROL
Averaged dustload_bin3
WRF-L CONTROL
Averaged dustload_bin4
WRF-L CONTROL
Averaged dustload_bin5
WRF-L CONTROL
Averaged total_dustload
WRF-L CONTROL
Dustload [gm^{-2}]
0.01 0.10 0.25 0.50 1.00 2.50 3.00 4.00 5.00 6.00

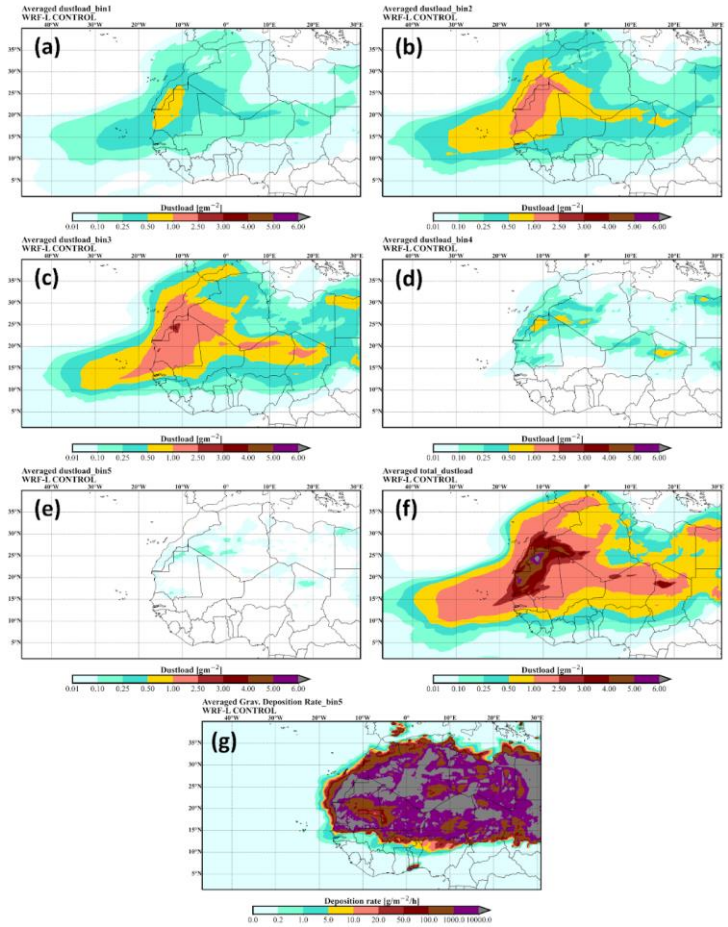

Figure 6: The dust load provided by the model, averaged for the whole simulation period, for (a) bin 1, (b) bin 2, (c) bin 3, (d) bin 4, (e) bin 5, and (f) the whole range of the PSD. The dust load is in g/m2. (g) The gravitational deposition rate for bin 5 in g/m2/h.

Μορφοποίησε: Όχι Εκθέτης/ Δείκτης

Μορφοποίησε: Χρώμα γραμματοσειράς: Αυτόματο, Αγγλικά (Ηνωμένων Πολιτειών)

Μορφοποίησε: Γραμματοσειρά: 12 στ., Χρώμα γραμματοσειράς: Αυτόματο, Αγγλικά (Ηνωμένων Πολιτειών)

Μορφοποίησε: Γραμματοσειρά: 12 στ., Χρώμα γραμματοσειράς: Αυτόματο, Αγγλικά (Ηνωμένων Πολιτειών), Όχι Εκθέτης/ Δείκτης

Μορφοποίησε: Γραμματοσειρά: 12 στ., Χρώμα γραμματοσειράς: Αυτόματο, Αγγλικά (Ηνωμένων Πολιτειών)

Μορφοποίησε: Αγγλικά (Ηνωμένων Πολιτειών)

1515

~~(a)~~

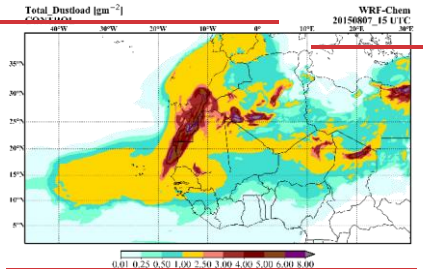
Total_Dustload [gm^{-2}]
WRF-Chem
2015080?_15 UTC
40°W
30°W
20°W
10°W
0°
10°E
20°E
30°E
35°
30°
25°
20°
15°
10°
5°
0.01 0.25 0.50 1.00 2.50 3.00 4.00 5.00 6.00 8.00

~~(b)~~

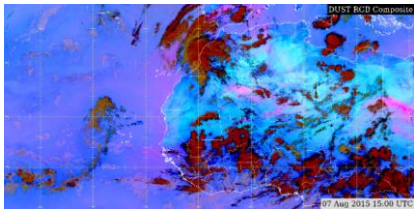
DUST RGB Composite
07 Aug 2015 15:00 UTC

~~(c)~~

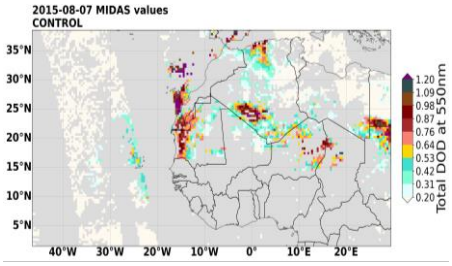
2015-08-07 MIDAS values
CONTROL
35°N
30°N
25°N
20°N
15°N
10°N
5°N
40°W
30°W
20°W
10°W
0°
10°E
20°E
1.20
1.09
0.98
0.87
0.76
0.64
0.53
0.42
0.31
0.20
Total DOD at 550nm

~~(d)~~

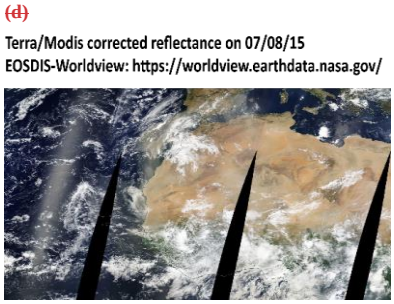
Terra/Modis corrected reflectance on 07/08/15
EOSDIS-Worldview: https://worldview.earthdata.nasa.gov/

(e)

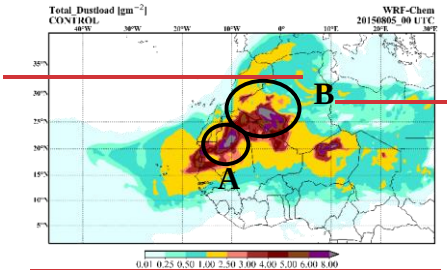

(f)

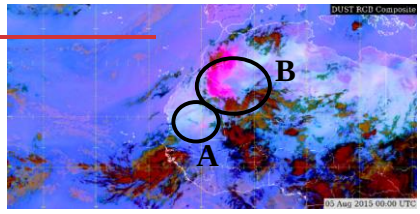

Figure 7: (a) Modelled dust load and (b) Dust RGB-Colors image from the MSG-SEVIRI. The fuchsia/pink colors indicate dust particles, with darker hue corresponding to higher concentrations or/and dust at higher altitudes. Both (a) and (b) show simulations and measurements, respectively, on 07/08/2015, at 15 UTC, near the time of b920 AER-D flight, at 15:24 -17:00 UTC. (c) MIDAS DOD at 550 μm, on 07/08/2015, and (d) corrected reflectance of Terra/MODIS on 07/08/2015. (e) Modelled dust load on 05/08/2015, at 00 UTC, and (f) Dust RGB image from the MSG-SEVIRI, on 05/08/2015, at 00 UTC.

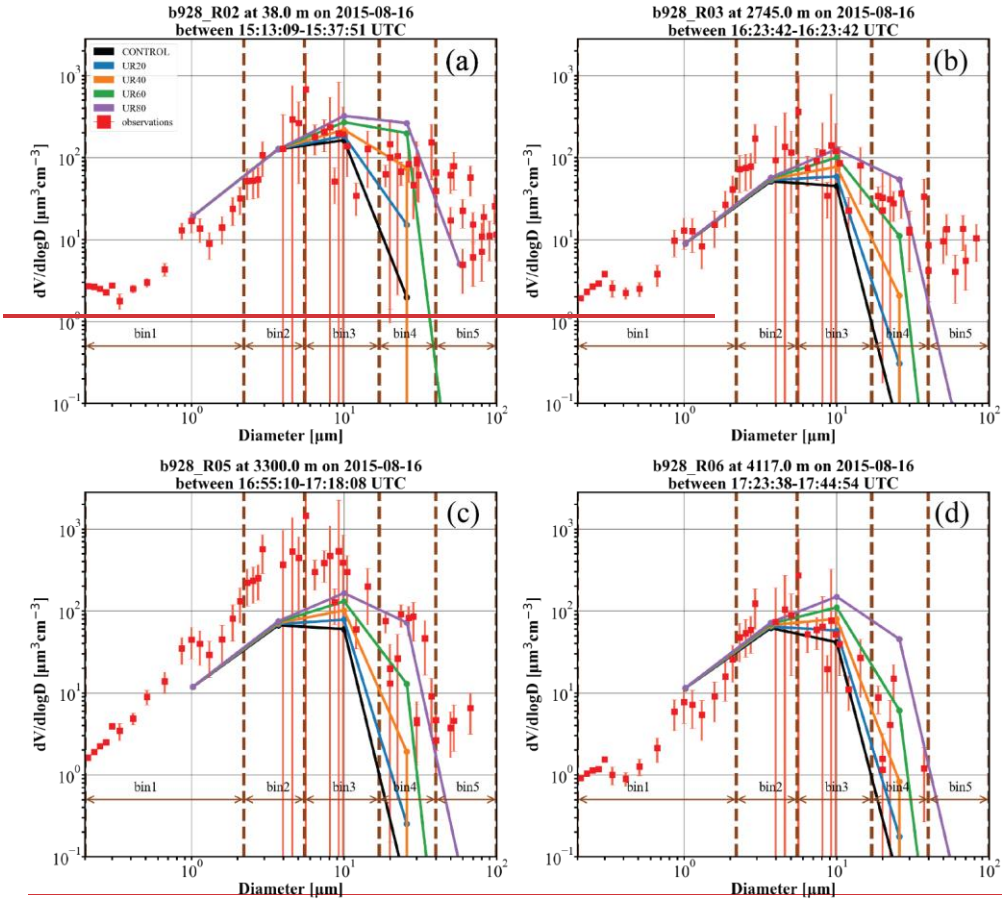
b928_R02 at 38.0 m on 2015-08-16
between 15:13:09-15:37:51 UTC
(a)
CONTROL
UR20
UR40
UR60
UR80
observations
bin1
bin2
bin3
bin4
bin5
dV/dlogD [µm³cm⁻³]
Diameter [µm]
b928_R03 at 2745.0 m on 2015-08-16
between 16:23:42-16:23:42 UTC
(b)
b928_R05 at 3300.0 m on 2015-08-16
between 16:55:10-17:18:08 UTC
(c)
b928_R06 at 4117.0 m on 2015-08-16
between 17:23:38-17:44:54 UTC
(d)

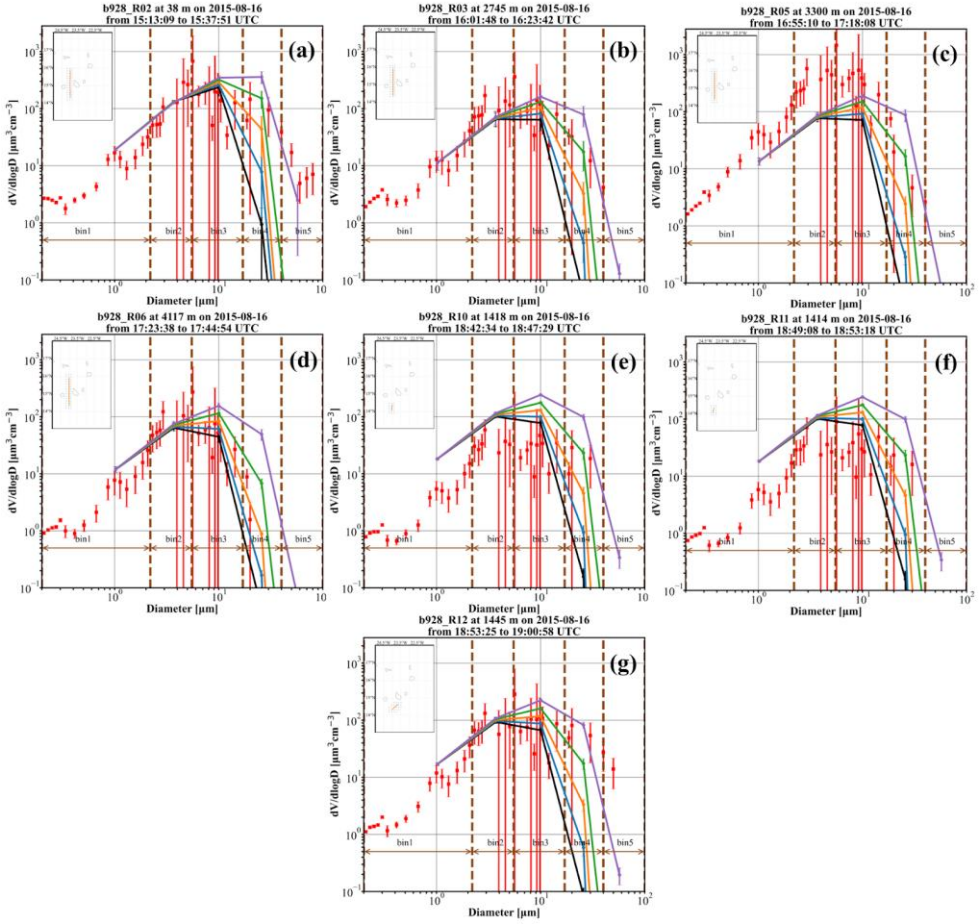

1530 **Figure 8: Modelled and observed dust PSD of flight b928, for straight-level runs (a) R02, (b) R03, (c) R05, and (d) R06. The in situ observations are shown with red squares (along with uncertainties), and the modelled PSDs with lines, for the CONTROL run (black), UR20 (blue), UR40 (orange), UR60 (green), and UR80 (purple). The brown vertical lines indicate the limits of the model size bins. The modelled PSD are collocated in space and time with the corresponding**

~~observations.~~ Figure 7: Modeled and observed dust PSD of flight b928, for straight-level-runs (a) R02, (b) R03, (c) R05, (d) R06, (e) R10, (f) R11 and (g) R12. The in situ observations are shown with red squares (along with the total instrumentation error). The collocated modeled PSDs are shown with lines, for the CONTROL run (black), UR20 (blue), UR40 (orange), UR60 (green), and UR80 (purple) and the corresponding standard deviation with the associated error bars. The brown vertical lines indicate the limits of the model size bins. The inlet maps show the flight segment track and the collocated model grid points.

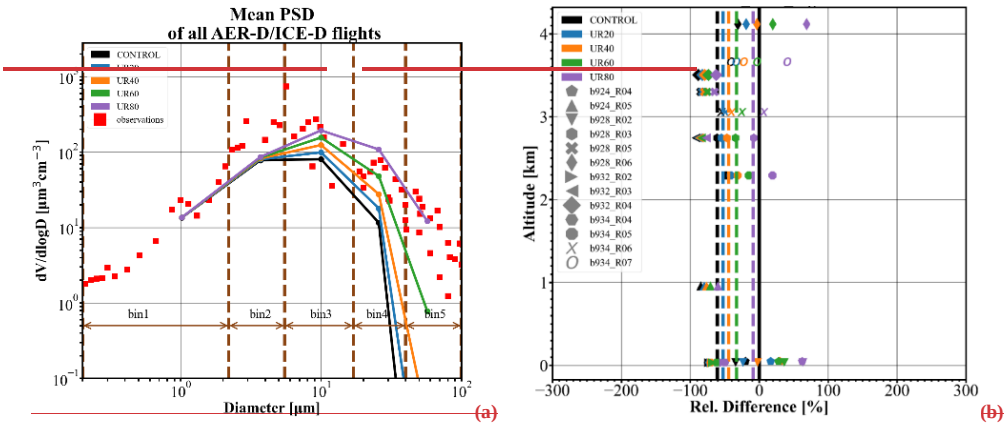

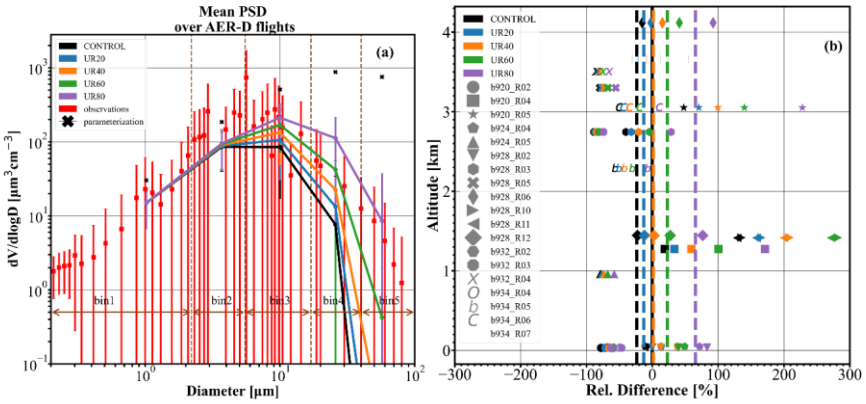

Figure 8: (a) Mean PSD of AER-D/ICE-D campaign. The observations are shown with red squares, whereas the simulations are shown with solid lines for the CONTROL run (black), UR20 (blue), UR40 (orange), UR60 (green), and UR80 (purple). (b) The relative difference between the observations and the model simulations of the total volume of dust particles, at different altitudes. The observations from different flight segments (i.e., b920 R02, b920 R04, b920 R05, b924 R04, b924 R05, b928 R03, b928 R05, b928 R06, b932 R02, b932 R03, b932 R04, b934 R04, b934 R05, b934 R06, and b934 R07) are denoted with different markers. The average relative difference of the observations and the simulations are denoted with dashed lines, for the CONTROL run (black), UR20 (blue), UR40 (orange), UR60 (green), and UR80 (purple).

~~Figure 9: (a) Mean PSD of AER-D/ICE-D campaign. The observations are shown with red squares, whereas the simulations are shown with solid lines for the CONTROL run (black), UR20 (blue), UR40 (orange), UR60 (green), and UR80 (purple). (b) The relative difference between the observations and the model simulations of the total volume of dust particles, at different altitudes. The observations from different flight segments (i.e., b924_R04, b924_R05, b928_R03, b928_R05, b928_R06, b932_R02, b932_R03, b932_R04, b934_R04, b934_R05, b934_R06, and b934_R07) are denoted with different markers. The average relative difference of the observations and the simulations are denoted with dashed lines, for the CONTROL run (black), UR20 (blue), UR40 (orange), UR60 (green), and UR80 (purple).~~

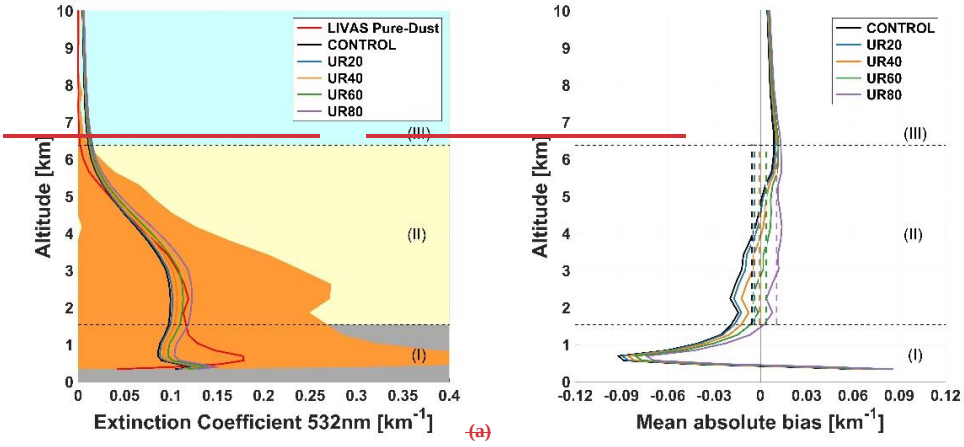

Μορφοποίησε: Αγγλικά (Ηνωμένων Πολιτειών)

Μορφοποίησε: Αγγλικά (Ηνωμένων Πολιτειών)

Μορφοποίησε: Αγγλικά (Ηνωμένων Πολιτειών)

Μορφοποίησε: Αγγλικά (Ηνωμένων Πολιτειών)

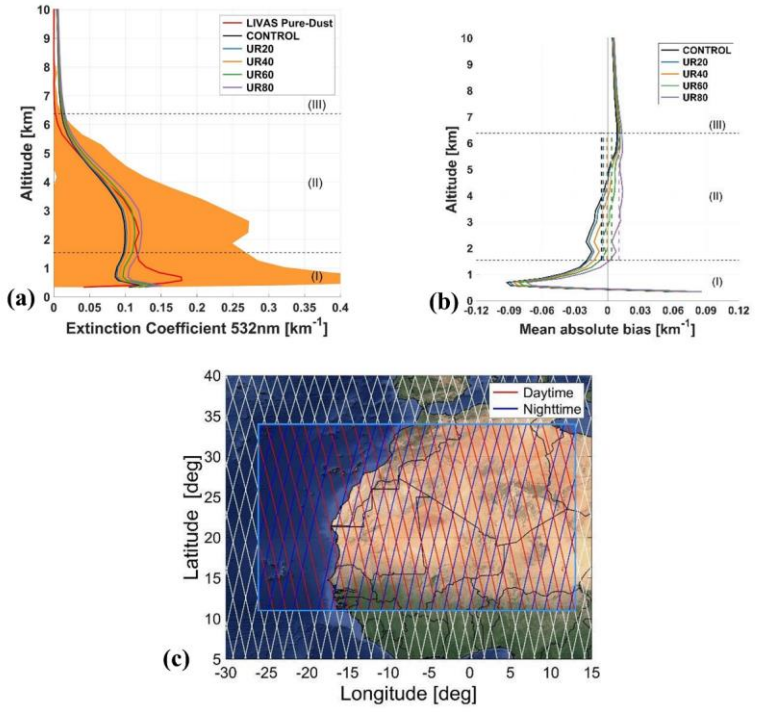

Figure 9: (a) Profile of the mean extinction coefficient at 532 nm, by LIVAS pure-dust product (black red line), and profiles of the mean extinction coefficient at 532 nm simulated from the different experiments of Table 3 (CONTROL, UR20/40/60/80). The orange shading indicates the standard deviation of the LIVAS profile averaging. (b) The mean absolute biases between the LIVAS profile and the simulated profiles from the different experiments, in the domain of interest, between 05/08/2015 and 25/08/2015. The vertical dashed lines are the mean absolute bias between the LIVAS profile and the simulated profiles from the different experiments averaged over the altitudes of region II. (c) The domain of interest and the daytime (red) and nighttime (blue) CALIPSO overpasses. The vertical dashed lines are the mean absolute bias between the LIVAS profile and the simulated profiles from the different experiments averaged over the altitudes of region II.

~~**Figure 10: (a) Profile of the mean extinction coefficient at 532 nm, by LIVAS pure-dust product (black line), and profiles of the mean extinction coefficient at 532 nm simulated from the different experiments of Table 3 (CONTROL,**~~

Μορφοποιήθηκε: Στοιχισμένο στο κέντρο

~~UR20/40/60/80). The orange shading indicates the standard deviation of the LIVAS pure-dust product (b) The mean absolute biases between the LIVAS profile and the simulated profiles from the different experiments, in the domain of interest, between 05/08/2015 and 25/08/2015.~~

Table 1 Size ranges and properties of model size bins in the default WRF-GOCART-AFWA scheme

WRF-GOCART-AFWA					
Bins	**1**	**2**	**3**	**4**	**5**
$D_{lo} - D_u$**(µm)**	0.2-2.0	2.0-3.6	3.6-6.0	6.0-12.0	12.0-20.0
D_{eff} **(µm)**	1.46	2.8	4.8	9.0	16.0
ρ_p **(g cm^{-3})**	2.5	2.65	2.65	2.65	2.65
WRF-L					
Bins	**1**	**2**	**3**	**4**	**5**
$D_{lo} - D_u$**(µm)**	0.2-2.2	2.2-5.5	5.5-17.0	17.0-40.0	40.0-100.0
D_{eff} **(µm)**	1.02	3.7	10.0	25.8	57.2
ρ_p **(g cm^{-3})**	2.5	2.65	2.65	2.65	2.65

Table 2 Configuration parameters of the WRF-L runs

Parameterization	**Scheme**	**Parameterization**	**Scheme**
Surface Model	Noah (Chen and Dudhia, 2001)	sf_surface_physics	2
Surface Layer~~Surface Layer~~	Monin-Obukov-Janjic (Janić, 2001) ~~MM5 (Jiménez and Dudhia, 2012)~~	sf_sfclay_physics~~sf_sfclay_physics~~	22
Radiation (SW and LW)	RRTMG (Iacono et al., 2008)	ra_sw(lw)_physics	4
Microphysics	Morrison 2-moment (Morrison et al., 2005)	mp_physics	10
Cumulus	Grell-3 (Grell and Dévényi, 2002)	cu_physics	5
Boundary Layer	MYNN 2.5 (Nakanishi and Niino, 2006)	bl_pbl_physics	5
Chemistry	GOCART simple (Ginoux et al., 2001; LeGrand et al., 2019)	chem_opt	300
Dust Scheme	AFWA (LeGrand et al., 2019)	dust_opt	3

Table 3 Experimental runs that performed in this study

Experiment	Code
CONTROL	WRF-L
UR20	WRF-L with reduced settling velocities by 20% of their settling velocity
UR40	WRF-L with reduced settling velocities by 40% of their settling velocity
UR60	WRF-L with reduced settling velocities by 60% of their settling velocity
UR80	WRF-L with reduced settling velocities by 80% of their settling velocity

Table 4: Lognormal ($\frac{dV}{dlnD} = \frac{V_{tot}}{\sqrt{2\pi}lns_g} exp\left(-\frac{(lnD_v - lnD)^2}{2(lns_g)^2}\right)$) mode parameters of the fitted FENNEC-PSD. Diameters are given in $[\mu m]$ and volume concentrations in $[\frac{\mu m^3}{cm^3}]$:

Modes	1	2	3	4	5
V_{tot}	15.16	27.07	169.32	310.5	563.3
D_v	1.0	2.5	7.0	22.0	50.0
s_g	1.8	2.0	1.9	2.0	2.15